DEPARTMENT OF MECHANICAL ENGINEERING
INDIAN INSTITUTE OF TECHNOLOGY
MADRAS
CHENNAI – 600 036

Development of a two-phase detection probe for high temperature lead-lithium liquid metal applications

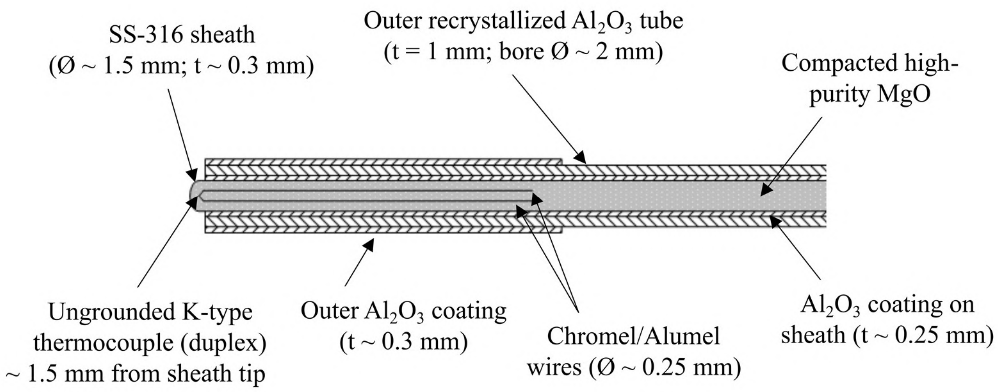

A Thesis

Submitted by

ABHISHEK SARASWAT

For the award of the degree

Of

MASTER OF SCIENCE by Research

April 2022

DEPARTMENT OF MECHANICAL ENGINEERING
INDIAN INSTITUTE OF TECHNOLOGY
MADRAS
CHENNAI – 600 036

Development of a two-phase detection probe for high temperature lead-lithium liquid metal applications

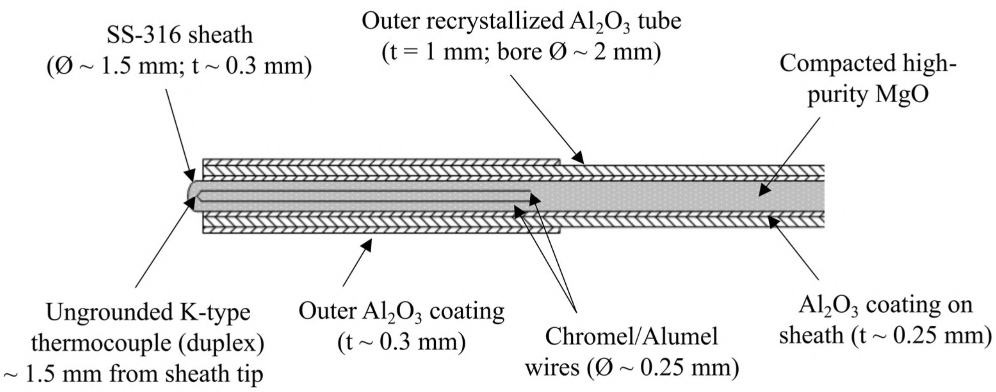

A Thesis

Submitted by

ABHISHEK SARASWAT

For the award of the degree

Of

MASTER OF SCIENCE by Research

April 2022

In no way can we get such an overwhelming idea of the grandeur of Nature, as when we consider, that in accordance with the law of the conservation of energy, throughout the infinite, the forces are in a perfect balance, and hence the energy of a single thought may determine the motion of a Universe.

- ***Nikola Tesla***

Dedicated

to

Akanksha *and* ***Saransh***

THESIS CERTIFICATE

This is to undertake that the Thesis titled, **DEVELOPMENT OF A TWO-PHASE DETECTION PROBE FOR HIGH TEMPERATURE LEAD-LITHIUM LIQUID METAL APPLICATIONS** submitted by me to the Indian Institute of Technology Madras, for the award of M.S. is a bonafide record of the research work done by me under the supervision of **Dr. Sateesh Gedupudi** (Guide) and **Dr. Paritosh Chaudhuri** (Co-guide). The contents of this Thesis, in full or in parts, have not been submitted to any other Institute or University for the award of any degree or diploma.

The research work has been carried out at IIT Madras and Institute for Plasma Research. In order to effectively convey the idea presented in this Thesis, the following work of other authors was reprinted in the Thesis with their permission:

- Figure 1.1, page 2: Reprinted from Matsuura and Nishikawa (2017) with the permission of Springer (publisher).
- Figure 1.2, page 2: Reprinted from Rajendrakumar *et al.* (2012) with the permission of Elsevier (publisher).
- Figure 2.1, page 30: Reprinted from Valls *et al.* (2020) with the permission of Elsevier (publisher).

Chennai 600 036
Date : Monday, 07 February 2022

Abhishek Saraswat
Research Scholar

Dr. Sateesh Gedupudi
Research Guide
Indian Institute of Technology Madras

Dr. Paritosh Chaudhuri
Research Co-guide
Institute for Plasma Research,Gandhinagar

LIST OF PUBLICATIONS

The publications arising out of the work mentioned in this thesis are given as follows:

I. REFEREED JOURNALS BASED ON THE THESIS

1. **A. Saraswat, C. Sasmal, A. Prajapati, R. Bhattacharyay, P. Chaudhuri and S. Gedupudi** (2022) Experimental investigations on electrical-insulation performance of Al_2O_3 coatings for high temperature PbLi liquid metal applications. *Annals of Nuclear Energy*, **167**, 108856.
   DOI: https://doi.org/10.1016/j.anucene.2021.108856.
2. **A. Saraswat, A. Prajapati, R. Bhattacharyay, P. Chaudhuri and S. Gedupudi** (2022) Development of a compact multivariable sensor probe for two-phase detection in high temperature PbLi-argon vertical columns. *Instruments and Experimental Techniques*, **65(1)**, 179-189.
   DOI: https://doi.org/10.1134/S0020441222010109.

II. PUBLICATIONS IN CONFERENCE PROCEEDINGS

1. **A. Saraswat, A. Prajapati, R. Bhattacharyay, P. Chaudhuri and S. Gedupudi**. Experimental investigations on bubble detection in water-air two-phase vertical columns. *2nd International Conference on Recent Advances in Mechanical Engineering (RAME-2020)*, New Delhi, India, September, 2020.
   The paper has been published as a chapter in Lecture Notes in Mechanical Engineering book series, 2021. pp 555-566.
   DOI: https://doi.org/10.1007/978-981-15-9678-0_48.

III. PRESENTATIONS IN CONFERENCES

1. **A. Saraswat, A. Prajapati, R. Bhattacharyay, P. Chaudhuri and S. Gedupudi**. Development of a compact multivariable sensor probe for two-phase detection in high-temperature PbLi-Ar columns. *International Conference on Diagnostics for Fusion Reactors (ICFRD2020)*, Varenna, Italy (remote), September, 2021.

2. **A. Saraswat, A. Prajapati, R. Bhattacharyay, P. Chaudhuri and S. Gedupudi**. Development of compact multivariable sensor probe for two-phase detection in high-temperature lead-lithium/argon vertical columns. *18th Multiphase Flow Conference (MPF2021)*, Dresden, Germany (remote), November, 2021.
3. **A. Saraswat, C. Sasmal, A. Prajapati, R. Bhattacharyay, P. Chaudhuri and S. Gedupudi**. Experimental investigations on electrical-insulation performance of Al_2O_3 coatings for high-temperature lead-lithium liquid-metal applications. *The 30th International Toki Conference on Plasma and Fusion Research (ITC30)*, Toki, Japan (remote), November, 2021.

IV. AWARDS

1. 2nd prize under best paper category for the following conference paper:

   A. Saraswat, A. Prajapati, R. Bhattacharyay, P. Chaudhuri and S. Gedupudi (2020). Experimental investigations on bubble detection in water-air two-phase vertical columns. *2nd International Conference on Recent Advances in Mechanical Engineering (RAME-2020)*, New Delhi, India (remote), September, 2020.

ACKNOWLEDGEMENTS

After being in a research-oriented environment for over nine years, I was very keen to restart my formal educational journey at IIT Madras. Although only a semester long, my residence period at the beautiful campus of IIT Madras was very pleasant and memorable.

I take this opportunity to express my sincere gratitude to my research supervisor **Dr. Sateesh Gedupudi** and co-supervisor **Dr. Paritosh Chaudhuri** for guiding me throughout the research work and providing me the clarity through detailed technical discussions and invaluable suggestions at every stage of my research. I am highly indebted to them for their constant encouragement and constructive criticism, helping me tackle the unforeseen challenges and making my journey more enjoyable.

I am sincerely grateful to my GTC Committee members **Dr. Srinivasa Rao Bakshi** and **Dr. Mayank Mittal** for their invaluable comments and suggestions towards improvement of this work.

I would like to thank **Dr. Rajendraprasad Bhattacharyay** and **Dr. Nirav I. Jamnapara** for their constant feedback and review of the experimental findings. I also express my gratitude to **Mr. Satya Prasad Akkireddy** and **Dr. Arunsinh B. Zala** for providing the necessary facilities towards completion of this research work.

I have immensely benefitted from the technical discussions held with my colleagues **Mr. Mahesh Vuppugalla**, **Mr. Vaibhav Ranjan**, **Mr. Chandrasekhar Sasmal**, **Mr. Ashok Prajapati** and **Mr. Hardik Tailor**, who actively helped me expand my interdisciplinary knowledge base.

I am also thankful to the staff at **IPR Workshop** for their support in timely fabrication of components required for this research.

Finally, I express my heartfelt gratitude to my loving wife **Akanksha** and my son **Saransh** for their continuous love and endless support. This journey would not have seen light of the day without their encouragement and dedicated efforts towards my academic success.

ABSTRACT

KEYWORDS: Liquid metal; two-phase; bubble; lead-lithium; insulation; coating.

Liquid-gas two-phase flow is a common occurrence in various industrial applications such as thermal power plants, steelmaking and refining processes etc. However, for nuclear fusion applications, where a lithium based liquid metal breeder/coolant is utilized, the existence of a two-phase flow may lead to certain critical issues including fuel inefficiency resulting from the reduced tritium breeding ratio, probability of mechanical failures due to generation of hot spots and safety considerations related to improper nuclear shielding. Out of the candidate liquid breeders, lead-lithium eutectic (Pb-16Li; hereafter referred to as PbLi) has gained immense focus for its various advantages and is utilized in several tritium breeding blanket concepts. Therefore, the development of a two-phase detection tool for PbLi liquid metal environment is imperative. Numerous two-phase measurement studies have been performed on room temperature/low melting liquid metals like GaInSn, Hg, Na etc. However, corrosive nature of PbLi coupled with constraints owing to high temperature operations severely restricts the application of commercially available diagnostic tools. This has indeed resulted in a lack of two-phase detection experiments in PbLi environment.

This work primarily aims to bridge the existing gap with the development and preliminary validation of a compact sensor probe as a measurement tool to experimentally study two-phase regimes in PbLi liquid metal environment. In this study, an electrical conductivity and temperature measurement based multivariable two-phase detection probe is developed using electrical insulation coating of high purity alumina (Al_2O_3). The probe is calibrated in a specifically designed liquid metal-gas two-phase test facility. Functional validation of the fabricated probe is achieved in high temperature PbLi-Ar (liquid-gas) two-phase vertical column with bulk PbLi temperature upto 400°C and time-averaged void fractions upto 0.95, covering two-phase flow regimes from well dispersed bubbly flow upto localized annular flows with void fractions similar to an in-box Loss of Coolant Accident characterized by a very large high pressure gas ingress inside bulk PbLi. Estimations of time-averaged void fraction, bubble frequency and average bubble residence time are performed. The experimental data corroborates high reliability and excellent temporal resolution towards individual bubble detection using electrical conductivity based principle, while the observed bulk temperature trends coherent with estimated void fractions provide qualitative insights into the presence of two-phase flows. A decrease in the experimentally measured bubble frequency with an increase in the time-averaged void fractions above 0.6 indicates coalescence of bubbles in the PbLi environment.

TABLE OF CONTENTS

LIST OF TABLES

LIST OF FIGURES

ABBREVIATIONS

BB	Breeding Blanket
CCD	Charged Coupled Device
CJC	Cold Junction Compensation
CTE	Coefficient of Thermal Expansion
DAQ	Data Acquisition
DC	Direct Current
DCLL	Dual-Coolant Lithium-Lead
DMFC	Digital Mass Flow Controller
ECFM	Eddy Current Flow Meter
EDX	Energy Dispersive X-ray
EMP	Electro Magnetic Pump
ETC	Effective Thermal Conductivity
FCI	Flow Channel Insert
FPS	Frames Per Second
FW	First Wall
HCLL	Helium Cooled Lithium-Lead
ICDD	International Centre for Diffraction Data
IITM	Indian Institute of Technology Madras
IPR	Institute for Plasma Research
IR	Insulation Resistance
LabVIEW	Laboratory Virtual Instrument Engineering Workbench
LBE	Lead-Bismuth Eutectic
LLCB	Lead-Lithium Ceramic Breeder
LM	Liquid Metal
LMFBR	Liquid Metal cooled Fast Breeder Reactor
LOCA	Loss of Coolant Accident
LOHS	Loss of Heat Sink

MHD	Magneto-Hydrodynamics
NR	Neutron Radiography
PID	Proportional-Integral-Derivative
PIV	Particle Image Velocimetry
PXI	PCI eXtensions for Instrumentation
PXIe	PXI Express
RAFM	Reduced Activation Ferritic-Martensitic
RT	Room Temperature
SEM	Scanning Electron Microscopy
SEN	Submerged Entry Nozzle
SS	Stainless Steel
TBM	Test Blanket Module
TBR	Tritium Breeding Ratio
TPB	Tritium Permeation Barrier
UHP	Ultra High Purity
USB	Universal Serial Bus
WCLL	Water-Cooled Lithium-Lead
XRD	X-Ray Diffraction

NOTATION

English Symbols

d	Bubble thickness additional to sensor conducting tip length
f_b	Bubble frequency
l	Length of conducting tip of the sensor
L	Length of insulation over cable
n	Neutron
N	Number of bubbles
r	Outer radius of cable conductor
R	Outer radius of insulated cable
R_i	Insulation resistance of a cable
T_b	Bubble residence time
V_g	Gas superficial velocity

Greek Symbols

α	Time-averaged void fraction
ρ	Volumetric electrical resistivity

CHAPTER 1

INTRODUCTION

1.1 THE BACKGROUND

The most promising of the nuclear fusion reactions, aimed at the generation of clean energy on earth, is the deuterium-tritium (D-T) reaction involving two isotopes of hydrogen. However, unlike the naturally abundant stable isotope deuterium, the rare radioactive isotope tritium, having a half-life of ~ 12.5 year, needs to be "bred" to complete the nuclear fusion fuel cycle. To achieve this aim, nuclear fusion Breeding Blanket (BB) concepts employ attractive solid and liquid breeder materials in the form of lithium/lithium-containing compounds like Li, Pb-16Li, Li_2O, $LiAlO_2$, Li_4SiO_4, Li_2SiO_3, Li_2TiO_3 and Li_2ZrO_3. Out of these candidate materials, eutectic lead-lithium (PbLi) Liquid Metal (LM) has gained immense focus owing to its various advantages including a high Tritium Breeding Ratio (TBR) without an additional neutron multiplier, circulation ability facilitating tritium extraction outside fusion blanket, inherent immunity towards radiation damage, high thermal conductivity and reduced chemical activity compared to pure Li.

A typical radial built-up of a fusion machine/tokamak is depicted in Figure 1.1 and a representative image for one of the candidate breeder concepts, namely Lead-Lithium Ceramic Breeder (LLCB), is shown in Figure 1.2. The D-T fusion reaction occurring in the magnetically confined, high temperature plasma produces energetic 14 MeV neutrons, which are bombarded against lithium (present in the blanket) to breed tritium in accordance to the following nuclear reactions.

$$\mathbf{D + T \longrightarrow He\ (3.517\ MeV) + n\ (14.069\ MeV)}$$

$$\mathbf{Li + n \longrightarrow He + T + 4.78\ MeV}$$

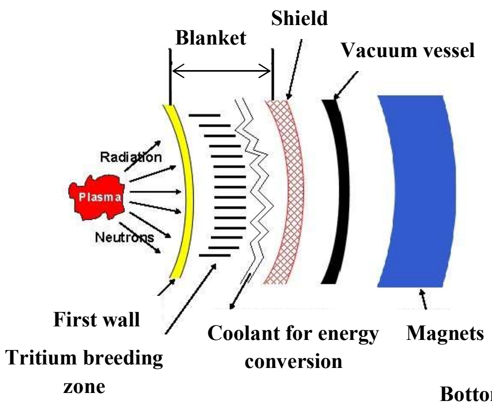

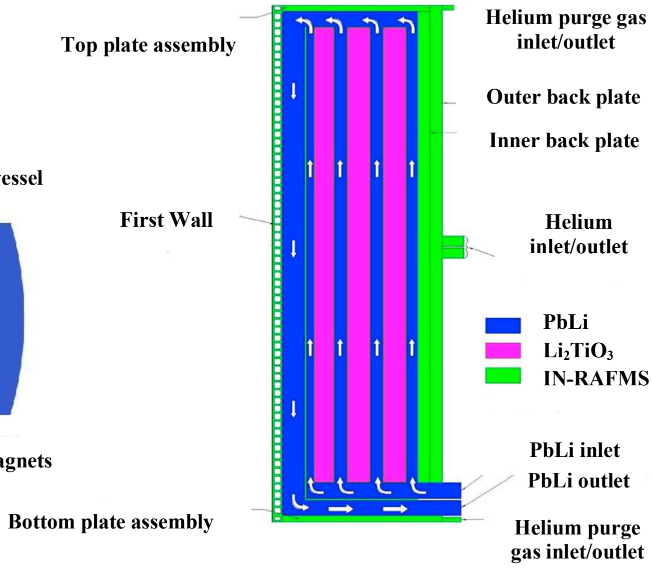

Fig. 1.1 Typical radial built-up of a fusion machine (Matsuura and Nishikawa, 2017).

Fig. 1.2 Simplified representation of a PbLi breeder blanket (Rajendrakumar *et al.*, 2012).

To enhance the tritium breeding, neutron multipliers like lead (Pb) and beryllium (Be) are utilized within the blanket. For instance, in LLCB concept, PbLi plays the role of neutron multiplier, tritium breeder as well as a coolant. Success of a breeder concept is primarily governed by TBR and heat extraction performance, which can be well achieved using PbLi in a self-cooled concept. However, as highlighted in above mentioned nuclear reaction, interaction of lithium with fusion neutrons, to breed tritium, leads to generation of helium gas as a by-product, having relatively low solubility in PbLi (Conrad, 1991). The generated gaseous helium could precipitate in the form of bubbles affecting system design and safety (Kordač and Košek, 2017).

Further, postulated accidental events like an in-box Test Blanket Module (TBM) Loss of Coolant Accident (LOCA) or a Loss of Heat Sink (LOHS) can occur due to rupture of well-defined boundaries between helium/water and PbLi, resulting in an ingress of a high pressure gas phase (helium/steam) inside PbLi circuit generating a LM-gas two-phase flow with unconventionally high density ratio between the two phases. Such two-phase regimes and trapped gas pockets are also expected in lab scale PbLi R&D facilities considering the installation constraints (like inclined nozzles for melt pressure sensors) and standard practices of charging LM in presence of an inert cover gas to provide cushion against volumetric expansion of LM and to avoid oxidation of LM due to ambient ingress.

Gas phase generation and entrapment within a PbLi breeder/coolant circuit may lead to reduced tritium breeding, improper nuclear shielding and compromised structural integrity (Kordač and Košek, 2017). Therefore, various BB concepts involving PbLi would invariably be prone to such a phenomenon. To model such occurrences of relevance towards design and operational safety of ancillary breeder/coolant circuits in future fusion reactors, an extensive experimental database needs to be generated, mandating development of proper diagnostic tools compatible with high temperature and corrosive PbLi environment.

Although non-contact techniques immensely benefit from non-intrusive nature of detection, a practical implementation of such techniques is rendered difficult in PbLi circuits due to opaque nature of fluid coupled with extreme operating environments, obstructions and installation constraints like surface heaters and thermal insulation, requirements for localized gas pocket detection, licensing requirements and high attenuation characteristics exhibited by LMs towards radiation based techniques. As a preliminary attempt to study two-phase flow regimes, electrical impedance based techniques offer a better route considering ease of installation, feasibility of adaptation and better response owing to large difference in electrical conductivities of LM and gas. However, adaptation of such a technique towards PbLi scenario puts severe demands on electrical insulation in terms of required compatibility towards corrosive media and operational temperature. In view of the above mentioned challenges restricting experimental studies on two-phase detection in PbLi environment, recently studies have been initiated using numerical/software tools for prediction of flow regimes in PbLi-He flows. It is further emphasized that results of numerical simulations for such advanced fluids must be validated by independent experimental campaigns.

1.2 THESIS ORGANIZATION

The thesis contains six chapters including the present chapter. A brief description of the contents of the chapters is presented below.

Chapter 1 presents a general introduction to the problem chosen and a brief introduction to the issues encountered in two-phase studies for PbLi applications. Organization of the overall thesis is also presented in this chapter.

Chapter 2 presents a detailed review of most relevant literature followed by the objective, scope and methodology of the present study.

Chapter 3 provides details on preliminary experimental investigations on water-air two-phase vertical columns. This chapter provides details regarding fabrication and calibration of a prototype probe, experimental set up and measurement tools. Results are presented for quantitative estimations of bubble impaction chord length and time-averaged void fractions.

Chapter 4 briefly discusses the criticality and potential applications of an electrical insulation coating for LM breeder/coolant ancillary circuits in nuclear fusion power plants. This chapter provides details on experimental runs towards optimization of heat curing parameters for depositing electrically insulating alumina coating on Stainless Steel (SS) substrates. This chapter elaborates the experimental methodology followed for quantitative assessment of in-situ insulation integrity in PbLi LM environment with estimations of volumetric electrical resistivity and temperature dependent insulation resistance derating factors. The chapter also presents results from detailed metallurgical analyses performed towards coating characterization like thickness estimations, LM ingress depth and surface morphology.

Chapter 5 presents details on basic sensor design and fabrication of the multivariable probe through utilization of validated alumina coating. This chapter depicts design details of two-phase test facility and utilized experimental tools. Results on probe calibration and probe performance in high temperature PbLi-Ar column with estimations of time-averaged void fraction, bubble frequency, bubble residence time and critical observations are presented.

Chapter 6 highlights the major conclusions and observations derived from the present study. The chapter ends with discussion and outline on future scope of work.

1.3 CLOSURE

In this chapter, a brief background on the identified problem alongwith an outline of the thesis is presented. The next chapter presents a detailed literature review relevant to the present study.

CHAPTER 2

REVIEW OF LITERATURE

2.1 INTRODUCTION

Numerous two-phase detection experimental studies are available for common fluid pairs like water-air or oil-gas systems. However, the detection of two-phase in LMs presents challenges in terms of opacity, temperature, surface obstructions like heat-tracer lines and thermal insulations, attenuation in radiation based measurements etc. Therefore, in view of the objective of present study being detection of two-phase flow in PbLi LM applications, this chapter presents a detailed review of relevant literature specific to LMs. The following subsection presents experimental studies performed towards LM two-phase flow detection with main emphasis on the utilized measurement techniques and major observations. A few numerical studies are also discussed in relevance to the research work under this thesis.

Chen *et al.* (1968) developed a resistivity probe for void detection in LMs. To circumvent the problem of requirements of an electrical insulation compatible with LMs, the authors studied a probe fabricated with an all metal sheath. The estimations suggest a signal of 25 mV from the probe using an excitation current of 1.1 Ampere. Authors validated the functionality and estimated response time for the probe with manual dip/ retrieval cycles in a liquid mercury pool at Room Temperature (RT). Actual two-phase detection studies were conducted with air bubbling in liquid mercury pool at RT. The radial profiles of local void fraction showed a core peak pattern. Although no results have been presented for high temperature applications for the probe, authors claimed that the developed configuration can be adapted for use upto 900°C.

Schwerdtfeger (1968) utilized ultrasound pulse echo technique to measure rise velocity of argon bubbles in liquid mercury column (at RT) in a plexiglass cylindrical container. The authors specifically highlighted the non-applicability of available correlations for LMs in consideration to their higher surface tension. Top surface of mercury was covered with distilled water (10 cm layer) to enable visual observations of emerging bubbles while the transducer was immersed 10 mm below mercury surface. Bubbles were ejected using a glass tube. Velocities were also measured in distilled water to check the reliability of the technique. It was observed that the experimental data for rise velocity of bubbles in distilled water agreed with correlations for similar experiments. While for mercury, a deviation was observed using same correlation. The study further suggests that for larger bubbles the velocity of rise becomes independent of the liquid properties and could be correlated within uncertainty limits to an existing correlation considering the fact that surface tension to density ratio did not differ larger than a factor of two in the correlation and the experiment.

Sano and Mori (1974) studied bubble formation in mercury-air (at RT) and liquid silver-air/oxygen (1000°C) using single nozzles of varying bore diameters. The study was aimed towards bubbling phenomena in steelmaking and other industrial processes. Authors suggested that bubble size is dependent on the gas flow rate, gas chamber volume, nozzle diameter and liquid properties like density and surface tension. Authors discussed in detail the effects of variations in the above parameters on the bubble size formed. Ejection of gas at constant low flow rate was achieved using an assembly of a falling weight, synchronous motor and frequency converter on top of the gas injection syringe. Bubble size was estimated using injected gas volume and bubble frequency assuming a spherical shape. The bubble frequency was arrived at through visual observations at the surface of the melt for low bubble frequency (< 200 bubble/minute), while for higher frequency, pressure pulse technique was utilized in conjunction with an earphone and sound recorder assembly. The study concluded the size of bubbles is mainly dominated by the outer diameter of nozzle in LMs which do not wet the nozzle.

Andreini *et al.* (1977) adopted a novel acoustic technique to measure velocity and volume of gas bubbles injected in different melts (tin, lead and copper). The underlying principle to estimate bubble frequency was the detection of distinct noises (using a unidirectional microphone in conjunction with a band-pass filter) generated by the bubbles breaking from a submerged nozzle and bursting the LM surface. The measurements were done for different melt-gas combinations like argon-tin (262°C), argon-lead (357°C) and argon-copper (1113°C). Experimental observations suggest increase in bubble frequency with an increase in the gas flow rate. Authors concluded that the mode of bubble formation is same for all the studied LMs and is independent of the liquid density and viscosity. It was suggested that the generated bubble sizes are proportional to the gas flow rate, orifice diameter, liquid surface tension and the gas density with defined exponents. The study further suggested that most of the bubbles generated have oblate spheroid shapes while spherical cap type bubbles were generated using a 0.1 cm orifice in argon-lead system. Experimental observations deviated significantly from static water-air systems with increased discrepancy as the bubble size and formation frequency increased.

Sano and Mori (1980) studied size of nitrogen bubbles in mercury column (at RT) within a glass tank using electro-resistivity probes. Bubble frequency measured using the electro-resistivity probe alongwith gas injection flow rate was utilized to estimate average bubble size. An important observation of gas fraction inside the injection nozzle less than unity highlights that mercury flows back into the nozzle after detachment of bubble. Experimental observations suggest that the position of maximum bubble frequency from the nozzle seems to be dependent on the gas injection rate. Authors highlight that the experimental data do not agree well with the correlations derived for water systems for estimation of bubble diameters, although at higher gas velocities, a few correlations were able to predict the bubble diameters in mercury. Authors suggest that the bubble size at such high gas flow rates is independent of fluid properties. Observations were made regarding presence of various small sized bubbles dispersed in the mercury column. Results also showed an altogether opposite tendency in contrast to water-air systems where volume-surface mean diameter tends to decrease for water-air systems. Study suggests that at lower gas flow rates, single bubbles are formed uniformly which then move towards a pair formation of large and small bubbles as flow rate is increased. Further increase of flow rate leads to physical interactions between the two bubbles towards coalescence. This study suggests that the nozzle diameter has no influence on the frequency distribution and volume-surface mean diameter of bubbles in swarms while the phenomena of bubble break-up and coalescence occur simultaneously.

Tsuchiya *et al.* (1993) employed pressure fluctuation detection technique to evaluate the bubble diameters towards applications in sweep gas bubbling utilized for tritium extraction in LM breeders. The utilized liquids were water (RT), methanol (RT), mercury (RT) and lead-lithium alloy (400°C) with injection of helium gas within a pyrex chamber. Varying shapes and diameter were explored for injection nozzles. It is highlighted that the bubble diameter is affected by shape, material and diameter of the nozzle in addition to the density, surface tension and viscosity of the liquid. The study includes study of low and intermediate gas flow rates, but excludes injection of gas at high flow rates which gives rise to jetting where bubbles are not formed. An indirect technique was utilized to measure pressure change through a condenser microphone, in the gas feed line when bubbles are generated at nozzle tip. Bubble size was estimated using gas flow rate and bubble generation frequency assuming a spherical shape. The correlation provided by Sano and Mori was modified and applied to study estimated bubble diameters against experimental measurements and was found to agree well for J-type and L-type nozzle shapes. It was concluded that the bubble size tends to vary with nozzle shape due to difference in wetting by the liquid medium.

Iguchi *et al.* (1995) utilized a two-needle electro-resistivity probe to experimentally estimate argon bubble characteristic in a molten iron bath at 1600°C towards gas injection techniques in steelmaking processes. Probe electrode was fabricated from a 0.5 mm platinum wire coated with ZrO_2 cement (< 0.5 mm thickness) and outer coat of alumina as an insulator. Life span of the probe was limited to ~20 min at 1600°C. Previous investigations by Iguchi *et al.* (1994) using a probe needle made of $LaCrO_3/ZrO_2$ sustained the probe at 1250°C iron bath for over 2 h. However, the life span of $LaCrO_3$ in iron bath at 1600°C was less than 3 minute and use of ZrO_2 restricted useful measurements due to almost overlapping electrical resistances of ZrO_2 and Al_2O_3 outer insulation. Argon gas was preheated before injection and the molten iron was placed in a carbon crucible within a furnace. Heat shock to the probe was avoided by preheating the probe for 20 minutes above the melt. A steady decrease in the gas holdup was observed between the nozzle exit and the bath surface. Observations suggest mean bubble diameter approximately 25 mm for both flow rates of 50 cm^3/s and 100 cm^3/s, which was in discrepancy with existing empirical correlations. Uniformity of bubble diameter along radial direction suggests rise of bubble in a zig zag path. A core peak trend was observed for both the gas holdup and bubble frequency along the axial direction.

Thiyagarajan *et al.* (1995) developed a non-intrusive gamma ray attenuation based technique using cobalt-60 source towards detection of two-phase flow in a density difference driven mercury-nitrogen loop (at RT) towards application in Magneto-Hydrodynamics (MHD) power generation systems. The radioactive source was contained in a lead shielding while a focused gamma ray beam was obtained using collimator shield window. Overall accuracy of the system was ascertained by creating zones of well-defined void fractions by insertion of plastic tubes within a mercury column. It was observed that at a given location, void fraction tends to increase with increase in the gas flow rate. It was concluded that the predicted void fractions using empirical relations for vertical two-phase flow match reasonably well with experimental observations.

Eckert *et al.* (2000) studied dispersion of gas bubbles within sodium-argon (at 200°C) and mercury-nitrogen (RT) flow loops subjected to external transverse and longitudinal magnetic fields (maximum of 0.45 T) with local void fraction detection using array of resistivity probes. Challenges in applying commercial techniques are highlighted by the authors due to opacity, abrasiveness and high temperature of LM systems. The Hg-N_2 two-phase flow was studied with limited void fractions (<5%) to reduce the bubble-induced turbulence. Experimental observations suggest uniform distribution of local void fraction profile over the cross-section in absence of an external magnetic field. However, application of an external magnetic field (~ 50 mT) modified the local void fraction profile to a core peak, which gets further concentrated with an increase in the magnitude of magnetic field with suppression of bubble dispersion in a direction parallel to the magnetic field. It was observed that with an externally applied longitudinal magnetic field, the radial distribution of the void fraction remains isotropic over varying Reynolds number.

Cha *et al.* (2003) employed electromagnetic flowmeter to assess the suitability for measuring two-phase flow in vertical upwards concurrent Na-N_2 mixture with a maximum temperature upto 190°C and superficial velocity 0.09 m/s to 0.4 m/s. Authors emphasize difficulties in two-phase detection for LMs considering the temperature and opacity. Void fraction estimation was not done directly but was estimated using two flowmeters in the loop. The study suggests the liquid flow rate in a two-phase mixture could be measured directly only if void fraction estimations have been conducted both in water-air and Na-N_2 flow mixtures. The instantaneous location of a slug bubble could be detected by the change of phase in the generated voltage. For bubbly flow regimes, a discrepancy was observed between experimental results and estimations from correlation. Although, the overall shape of the output signal retains its form, the magnitude is larger in case of two-phase flow due to reduction in flow area available for liquid phase.

Suzuki *et al.* (2003) conducted experimental studies on PbBi-N_2 two-phase systems using Neutron Radiography (NR) technique with LM column thickness of 20 mm for a maximum temperature upto 200°C. Observations suggested deformed ellipsoidal bubbles with diameters upto 10 mm at lower gas fluxes and spherical/deformed cap bubbles upto 30 mm in diameter for higher gas fluxes within bubble flow regime. The study suggested modification of two-phase flow regime map with bubbly flow regime upto 0.3, transition regime (containing both bubbly and droplet flow) for 0.3-0.7 and droplet flow regime above 0.7.

Saito *et al.* (2004) employed NR and Particle Image Velocimetry (PIV) for visualization and measurement of two-phase flow for PbBi-N_2 at a maximum temperature of 150°C and N_2 velocity range of 0-15 cm/s. The study emphasizes the differences in density ratio and surface tension for LM-gas flows as compared to water-air flow. For visualization of flow using PIV, tracer particles of gold-cadmium were employed (size 1-1.5 mm) considering densities and wetting behavior. NR technique suggested presence of spherical and ellipsoidal shaped bubbles at low gas velocities and deformed cap bubbles at velocities greater than 2 cm/s. A recirculation flow was observed to be induced by rising bubbles in LM column. Experimental measurements further suggest uniformity of void fraction profiles at low gas flow rates (1.4 cm/s) changing to a core peak at higher gas flow rates. This effect is attributed to temporary entrapment and coalescence of bubbles before breaking up and dispersion towards the wall. For ellipsoidal bubbly flow, void fraction profile was observed to fluctuate from side to side.

Zhang *et al.* (2005) applied non-intrusive ultrasound doppler velocimetry to study the motion of single argon bubbles rising in GaInSn column (at RT) in presence of a Direct Current (DC) longitudinal magnetic field with field strength upto 0.3T. The study was aimed towards contactless control of bubble motion in the melts like during steel processing. Authors highlight lack of measurement techniques and studies on gas-LM flows. An open perspex cylinder was utilized as LM vessel while very low gas flow rates were maintained to study isolated bubble phenomena. Equivalent bubble diameters estimated using gas flow rate and bubble frequency were in the range 4.5 mm – 8.5 mm. Authors highlight the deviations observed between previous correlation and experimental data. This effect is attributed to presence of oxides, which alter the surface tension of the GaInSn melt. A slight rise in the mean terminal velocity was observed in presence of magnetic field while the shape and amplitude of velocity oscillations appeared more regular. A decrease in the normal velocity component of LM was observed with a longitudinally applied DC magnetic field and bubble assumed a rectilinear motion.

Cha *et al.* (2005) employed dynamic NR as a technique to visualize and measure multiphase flow in LM flowing within metallic ducts as a safety analysis towards Liquid Metal cooled Fast Breeder Reactor (LMFBR) design. Utilized fluids were lead-bismuth and nitrogen in a natural circulation loop made of SS-316 with flow channel diameter of ~ 22 mm (temperature details not available). The injected gas was preheated to avoid abrupt temperature dependent volumetric expansion. The imaging system was protected from radiation damage by enclosing the system in lead blocks and boron sheets. Superficial gas velocity was varied in the range 0-11 cm/s. Experiments suggest clear images obtained using the NR in spite of the presence of metallic walls and opacity of the liquids. Observations suggest detection of bubbly flow and slug flow. Authors suggest the dominant presence of cap bubbles or elongated slug bubbles due to high surface tension of LM.

Saito *et al.* (2005) employed NR and four-sensor electrical conductivity based probe for visualization and measurements in PbBi-N_2 two-phase flows concerning to the safety of LMFBR. Experiments were conducted at a temperature of 150°C and gas superficial velocity of 1-38 cm/s. Utilized conductivity probe contains silicon-resin varnish as an electrical insulation. Experimental observations strongly suggest good agreement between radial profiles of void fractions and bubble frequency measured using these two techniques. The study emphasizes experimental validation of available models to LM two-phase flows and also mentions limited spatial resolution available through NR technique. Authors propose utilization of conductivity probes to study local phenomena. However, the intrusive nature of conductivity probe is also highlighted in terms of bubble deformations. Visual observations suggest breaking of bubbles under high shearing stress of LM flow induced by preceding bubble resulting in absence of stable slug bubbles. Non-symmetrical profiles of radial void fraction were observed with both the measurement techniques and increase in the void fraction was reported with an increase in gas superficial velocity attributed to an increase in bubble size with higher superficial velocity.

Andruszkiewicz *et al.* (2013) implemented ultrasound transit time technique to study argon bubble detection in GaInSn (at RT). Arrays of ultrasonic transducers were arranged across the vessel. Measurement of bubble velocity was conducted using transit time measurements between the consecutive sensors of a single array. Study suggests limitation of the technique at very high void fractions due to permanent reflection of ultrasound signal. Signals could be extracted to understand the horizontal velocity component (or the tilt) in addition to vertical rise velocity. Diameter/lateral extension of bubbles could be determined using two opposite transducers. Experimental data suggests an increase in the bubble diameter from ~6.4 mm to ~7.8 mm and an increase in the deviation of the experimentally measured diameter from the theoretically derived diameter using the gas flow rate and bubble frequency. This effect is attributed to decreasing spherical shape of the bubble with increasing gas flow rate. Bubble generation frequency was also observed to increase with an increase in the gas flow rate. Study reported good agreement between the ultrasound doppler velocimetry and ultrasound transit time technique towards measurement of vertical rise velocity of bubble.

Klaasen *et al.* (2014) studied nitrogen bubbles in mercury (at RT) towards further development of pyrometallurgical gas injection reactors. Authors highlight the criticality of detailed experimental data over numerical studies and mention challenges like opacity and high temperature inherent to such an experimental study. Authors studied a quasi 2D bubble flow in a thin layer of LM between two flat parallel plates in a Hele-Shaw cell with the acknowledgement that a 2D study could not replace actual phenomena in the bulk melt. Adopted measurement technique was visual observations and high speed imaging with mercury filled in a soda-lime glass cell in view of poor wettability with mercury. Experimental data suggests that for bubble size smaller than 3 mm, no detachment occurred leading to gas hold-up near nozzle. Only for bubble size over 4 mm, spontaneous detachment from the nozzle could be achieved due to dominant buoyancy effect. Injection of more bubbles resulted in formation of bubble trains coalescing on their way up leading to larger bubbles being formed upto 20 mm in diameter. The small bubbles with a diameter below 5.3 mm, exhibited a linear regime with a constant circular or elliptical shape and a straight path, while bubbles larger than 6.4 mm showed a periodic regime with an oscillating, deformed shape along a swirling trajectory. In between these regimes, bubbles exhibit a mixed behavior. This effect is attributed to the expansion of the bubble under decreasing hydrostatic pressure along the ascending path. Authors conclude that the heavy LMs may not be correctly demonstrated using aqueous systems due to significant expansion of bubbles with decreased hydrostatic pressure.

Ariyoshi *et al*. (2015) performed experimental studies in a PbBi-N_2 two-phase upward flow loop as an accidental scenario in lead-bismuth cooled accelerator-driven system. The authors employed four-sensor based electrical conductivity probe to detect two-phase flow and estimate radial variations of void fraction, at various points along the flow, upto a maximum temperature of 200°C with application of silicon epoxy-resin varnish as an electrical insulation for conductivity probe. N_2 injection was achieved into the flowing PbBi using an injector consisting of 101 needles. Experimental observations suggested that the void fraction changes from wall peak (near the injection plane) to a core peak (after fully developed flow) i.e. void fraction increased along the flow direction due to movement of larger bubbles towards the central region. The study also suggested that the bubble shape in a LM two-phase flow might be strongly distorted by the momentum exchange at the gas–liquid interface and, therefore, emphasized development of correlations based on experimental data specific to LM scenarios.

Gundrum *et al.* (2015) carried out experimental studies towards detection of individual argon gas bubbles in RT LM alloy Galinstan (GaInSn). The utilized non-contact measurement technique is based on electromagnetic induction principle with receiver coils arranged in series opposition. The technique is robust being sensitive only to asymmetric magnetic fields. Theoretically estimated bubble diameter in an atmospheric pressure column varied between 5 mm and 8.7 mm. Experiments suggested movement of bubbles in a straight line path from injection to surface as well as a variation in the bubble size, the latter effect attributed to effect of wetting and surface tension of LM. The sensor response indicated single bubble detection upto 1 bubble/s. The technique was further validated in sodium melt at 150°C considering applicability for sodium/water heat exchangers. Although the detection of bubbles was successful in molten sodium at rest, the study suggests challenges in the detection of bubbles during flow of liquid sodium using an Electro Magnetic Pump (EMP), due to electromagnetic interference related issues. Such a technique requires very sensitive measurement system to detect small variations in the induced voltage.

Timmel *et al.* (2015) implemented X-ray radioscopy technique, with GaInSn at RT as the surrogate liquid, towards understanding of two-phase flow in the mold and Submerged Entry Nozzle (SEN) during continuous casting process of steel. Authors highlight that complex turbulent two-phase regime are difficult to predict using numerical models. Authors suggest lack of detailed two-phase studies in the LM scenario. The melt is discharged from an acrylic glass tube of 12 mm X 12 mm cross-section into the mold of 100 mm X 15 mm cross section while the test section materials are chosen so as to be non-wettable with the melt. Acrylic glass avoids significant attenuation of the X-ray intensity while the limit on LM depth was in consideration to high attenuation exhibited by LMs towards X-ray. Lead shielding was necessary to reduce exposure to sensitive equipment and to enhance contrast of X-ray imaging. Experimental observations suggest partial filling of SEN with prominent presence of gas pocket zones. In the lower nozzle zone, only a few large gas bubbles were observed and the flow regime strongly depended on the ratio of gas to LM flow rate. An increased gas flow rate resulted in turbulent flow regime while tendency towards bubbly flow regime could be established at high LM flow rates. The observed bubble shape was non spherical and sizes were estimated to be between 2-5 mm, with a quantitative estimation rendered difficult due to low signal to noise ratio. Coalescence of bubbles were observed in recirculation zones below the SEN due to increased residence time (5 s – 15 s) in the melt. It was concluded that the deviations of the results from previous reported studies is due to preferential wetting of the nozzle with water in contrast to limited wetting by LMs.

Vogt *et al.* (2015) performed experiments for detection of entrained argon gas in RT LM GaInSn in view of relevance towards safety of LMFBRs. The study emphasized lack of measuring techniques for LM two-phase flows. First utilized technique was based on transit time technique using an array of ultrasonic sensors attached to the surface of a perspex vessel for bubble detection in vortex configuration funnel shaped surface depression. The second technique utilized was X-ray radiography for detection of upward rising argon bubbles in a LM column within a rectangular cross-section perspex box. Detection using this technique requires a sophisticated set up consisting of scintillating screen, mirror arrangement, lens system and Charged Coupled Device (CCD) camera. The study presents stark differences between two-phase systems based on water and LMs. These differences include formation of larger gas bubbles due to higher surface tension of LMs, higher rate of bubble collisions leading to coalescence in LMs and breaking of large bubbles due to high shear stresses in LM environment. Further, the experimental observations suggest increased bubble residence time near the free surface of LM. Increase in the gas injection flow rate resulted in higher frequency of bubble entrainment further increasing the probability of bubble coalescence. Considering substantial differences between water and LM systems, the study emphasized specific LM based model experiments to understand LM-gas two-phase flows.

Wang *et al.* (2017) conducted experimental investigations on argon bubbles rising in a GaInSn column (at RT), arranged within a perspex container, in presence of a transverse magnetic field (B_{max} = 1.97 T) by utilizing ultrasonic doppler velocimetry. Authors highlighted the complexities involved considering the opacity and lack of suitable measurement techniques for gas-LM flows. Single bubble injection was done to avoid bubble interactions and wake effect on the following bubble. Experimental observations depict sinusoidal variations between the instantaneous velocity and height of the vertically rising bubbles of ~ 4.57 mm equivalent diameter in absence of magnetic field. Data analysis suggests that the previous correlation adjusted for GaInSn tend to overpredict the bubble rise velocity in GaInSn by almost 15%, which is attributed to the oxidation of melt in case of GaInSn, effectively reducing the surface tension. It was further observed that for smaller bubbles of size 3.1 mm and 3.4 mm, presence of a magnetic field decreases the ascension velocity. For larger bubble size (4.57 mm, 5.15 mm and 5.6 mm), velocity increases in presence of a weak magnetic field but reduces with an increase in magnetic field strength attributed to a combined influence of electrical conductivity of melt and generated Lorentz force due to magnetic field. Magnetic field was also found to suppress the bubble velocity component normal to the direction of magnetic field.

Keplinger *et al.* (2017) validated X-ray radiography technique against optical methods for detection of argon bubbles in water medium providing insights about bubble size, bubble velocity and bubble shape. Further the technique was extended for application in RT LM alloy GaInSn. This study emphasizes LM specific experimental investigations in view of strong differences in density, viscosity and surface tension. The authors mention limitations of various techniques applicable to LM two-phase flows suggesting limited LM thickness for which X-ray absorption technique may be applied. Container of acrylic was utilized to avoid significant attenuation of X-rays with LM column thickness restricted to 12 mm. Experimental observations suggest good agreement between the two techniques for water applications with visual observations on the significant deformations in bubble shape after detachment from nozzle leading to flattening in vertical plane followed by zig zag motion upwards. This study suggests a stark decrease in the bubble injection frequency in water and LM medium for the same gas injection rate with an average bubble size in LM almost twice as large as that in water. These effects are attributed to the high surface tension of LM and wetting of injection nozzle. The study further suggests less deformation in bubble shape due to large surface tension of GaInSn preventing surface wobbling resulting in change of bubble shape from a ellipsoid to almost spherical for heights above 30 mm. Experimental observations indicate similar rising velocities in water and GaInSn considering the buoyancy effect compensation with increased drag force due to large bubble size.

Kordac and Kosek (2017) performed numerical assessments of helium gas generation due to neutron bombardment of lithium for European DEMO relevant PbLi blanket. Authors highlighted the issues like fuel inefficiency, insufficient heat extraction and improper nuclear shielding due to the two-phase flow in PbLi breeder. Calculations were performed for a mean blanket temperature of 400°C and tritium production rate of 385 g/day with the assumption of no returning of produced helium into the blanket. This study suggested that helium generation is quite sensitive to the pressure and flow rate of PbLi in the blanket. Estimations highlight significant generation of helium gas for PbLi flow rate below 1000 kg/s, independent of pressure, while for a typical pressure of 10 bar, all helium leaves the blanket only at a flow rate of 10,000 kg/s with no bubble formation. For a given flow rate of 10,000 kg/s, estimations provide helium generation of 13.1 l/h at 5 m depth and 214.7 l/h at the surface due to reduction in hydrostatic pressure of alloy leading to more generation of helium. Authors highlight that such a phenomenon may lead to a decrease of upto 12% of the breeder volume after one year operation and suggest that the blanket configurations built on higher PbLi flow rates seem more resistant to this phenomenon.

Krull *et al.* (2017) conducted experimental investigations on bubbly flows in RT atmospheric pressure GaInSn LM using X-ray radiography. Authors highlight the complexity involved in detection of bubbly columns in LM environment and the criticality of experimental data towards validation of numerical models. Considering high X-ray attenuation by LMs, a narrow rectangular container made of acrylic was chosen for the study with LM column thickness of 12 mm. Authors highlight requirements of lead shields towards reduction of background noise from scattered radiation from the regions outside of LM volume and to avoid damage to video sensors. The equivalent bubble diameter was observed ~ 6 mm. In the study, the experimentally determined void fraction was slightly higher than numerical estimations. It is further observed that the rising bubbles induce a LM recirculation flow upstream in the centre and downstream remote from the chain near the side walls and the recirculation velocities differ between experiments and simulation.

Guichou *et al.* (2017) studied two-phase detection in RT GaInSn column, aimed towards achieving safety and reliability of sodium coolant loops in LMFBR. Utilized technique for the purpose involved Eddy Current Flow Meter (ECFM) with millimeter sized insulating beads (2 mm - 5 mm) controlled by 50 micron thick positioning thread within a non-conducting non-ferromagnetic ceramic tube and the secondary coils in series opposition. The ECFM copper coils were mounted on a polymer ring, where the ECFM has been provided with a controlled translational motion. Presence of the bead is detected by oscillations in the amplitudes of measured voltage difference at the position of bead. Response of the output signal is observed to be dependent on the bead size and the excitation frequency.

Usov *et al.* (2017) studied gas phase transport in a vertical stagnant column of Rose's alloy-argon towards understanding of a steam generator tube rupture accident in LMFBR. Study highlights lack of information on LM two-phase flow and stresses on numerical and experimental investigations specific to such scenarios. Temperature of the melt was maintained at 150°C. A conductivity sensor was utilized for measurement of gas volume fraction. The study suggested good agreement (within 12%) between experimental data and numerical estimations for two-phase flow in tubes. It is further suggested that the gas volume fraction is dependent on the volume flow rate of gas and velocity of gas bubbles.

Karcher (2018) experimentally explored the application of Lorentz force velocimetry for detection of non-conducting particles in LM towards applications in process and quality control in metallurgy. The utilized melt is RT GaInSn column with non-conducting (plastic) spherical particles of known dimensions (~ 6 mm) traversing the melt at controlled rate in a vessel made of plexiglass. The arrangement leads to force magnitudes in the range of micronewtons requiring special sensors. A simultaneously applied ultrasound doppler velocimetry provides the reference when the particle crosses the magnet system. A good agreement was obtained between experimental and simulation results to detect the presence of traversing object while measuring the lift force. However, drag forces were not in complete concurrence with the simulations.

Andruszkiewicz and Eckert (2018) experimentally studied two-phase flow in a column of GaInSn-argon (at RT) using ultrasonic echo pulse method towards effectiveness of metallurgical processes of refining and degassing related to argon gas blow-in. Experiments were performed with and without magnetic field. Two arrays of ultrasonic sensors were deployed consisting of 10 sensors in each array with 15 MHz frequency. Utilizing the echo run time, signals from both arrays were alternatively recorded providing the bubble velocity and trajectory. Observations suggest for argon gas flow rate greater than 1.8 lph, bubble velocity decreased in presence of a magnetic field and this difference kept on increasing with increase in the injection flow rate. It was also observed that the bubble generation frequency does not vary much with and without magnetic field leading to almost same average equivalent diameter of bubbles. The study suggested that in presence of a magnetic field, argon bubbles tend to rise almost straight and the width of rise zone is half of the width without magnetic field. Due to this effect, the number of bubbles in the detection zone is higher compared to the counterpart in absence of magnetic field. It was concluded that the reduction in the rise velocity of bubbles in presence of magnetic field enhances the contact time between LM and bubbles and could be better utilized for blow-in gas. Further the straight path movement in presence of magnetic field could be utilized for better gas distribution towards refinement and degassing of LMs.

Xu *et al.* (2019) performed experimental study to detect presence of argon bubbles in sodium flow loop as an accidental leakage in sodium cooled fast reactors leading to an intense chemical reaction and safety hazard. The measurements were performed using a modified version of electromagnetic vortex flowmeter and employing a peak-to-peak standard deviation algorithm by analyzing signal to noise ratio at different gas injection volumes. LM temperature was limited to a maximum of ~250°C. This study suggested minimum detectable water leakage amount as 0.1 g/s.

Keplinger *et al.* (2019) experimentally studied argon bubble chain ascending in a RT LM GaInSn column in presence of a horizontal magnetic field. Bubble ejection was done at the bottom centre of a plexiglass vessel with a limited LM column thickness of 12 mm considering high attenuation exhibited by LMs towards X-rays. X-ray radiography was employed to study bubble size distribution, deformation and velocities. The study suggests that presence of magnetic field suppresses the zig-zag movement of bubbles leading to a straight path. Increase in the magnetic field is also observed to decrease the rising velocity. The study emphasizes scarcity of experimental data on two-phase flow in LMs due to limitations of measurement techniques in opaque fluids. In absence of magnetic field, the mean bubble diameter was observed between 5 – 7 mm and change of bubble shape from ellipsoidal to spherical with increasing gas flow rate. The effect of bubble chains in the rising phenomena is highlighted due to bubble wake interactions, as compared to single bubble case. Bubble chains was observed oscillating leading to symmetrical distributions of time-averaged void fractions with maxima along the centre line of vessel.

Keplinger *et al.* (2019) studied the process of bubble breakup, aimed towards enhancement of floatation efficiency in metallurgical treatment processes, in a GaInSn column at RT within an acrylic container, using X-ray radiography technique. Considering the difference in density and surface tension between LMs and water, authors suggest direct investigations on LMs. Authors also emphasize difficulties rendered in two-phase detection in LMs owing to the opacity. LM column thickness was kept 12 mm considering high attenuation of X-rays. Experimental observations suggest generation of bubble chains upto gas injection flowrates of 800 cm^3/min, while clusters of bubbles at higher flow rates. The bubble size seems to increase with an increase in injection flow rate. Experimental observations suggest bubble break-up onset at 400 cm^3/min with increasing break-up events till 700 cm^3/s, attributed to increased surface deformations with increase in bubble size. The break-up frequency seems to decrease/difficult to observe for gas injection flow rate 800 cm^3/min and higher. This study suggests that the trailing bubble is accelerated in the wake of leading bubble, which results in the bubble collisions with flattening of the leading bubble and rise of a cluster pair with a thin LM film in between finally leading to breaking of the leading bubble. Also, for individual bubbles, the bubble break-up is induced by stretching due to the influence of liquid turbulence. Here, the gas-liquid interface is subjected to high shearing stress. In contrast, coalescence of bubbles occurs at higher flow rates as suggested in the study.

Lyu (2019) applied Lorentz Force Velocimetry in RT LM GaInSn for two-phase flow detection towards quality controls in industrial metallurgical processes. Argon bubble injection was done in a cylindrical glass tube as well as a bigger plastic chamber with sufficient time gap (> 30s) in between individual bubbles to eliminate mutual interactions, leading to the recorded signal being representative of LM flow induced by individual bubbles. Author highlights that the bubble size is dependent on the nozzle diameter, gas pressure, density difference between two fluids, wetting properties of LM and surface tension of the LM. The distance between rising bubble and sensor part varied due to zig-zag path of the bubble in the column. Average vertical velocity and diameter of bubble were estimated as 22 cm/s and ~7.5 mm respectively. The resulting force due to bubble rise in the detection region was within micronewtons range but was measurable. Experimental observations suggest that for a bubble distant from the wall, the measured signal is not significantly affected by deformation and zig-zag motion. It was also observed that the signal reproducibility was poor in a bigger chamber. The detection technique was further employed for detection of argon bubbles in liquid tin at 300°C within a steel tube where the distance between sensor and tube was ~ 50 mm to decouple the sensor from high temperature. Although bubble generation could be visually confirmed on the top surface of the melt, issues like noises generated from the heater, distance of the sensor from melt and solidification of the melt prevented a good signal acquisition.

Corazza *et al.* (2020) studied the feasibility of optical fiber based local void fraction detection technique within lead-bismuth LM as a requirement towards next generation nuclear reactors. Authors stressed the challenges involved due to high temperature, corrosiveness and opacity of fluid. Different configurations of probe tips were fabricated for utilization in two-phase detection. Maximum temperature of the LM was limited to 200°C. It is shown that the probe can distinguish gas phase from LM. Authors conducted detailed study on the interaction effects like interface deformation, vicinity effects, overshoot, probe wetting etc. The vicinity effects encountered by cleaved shaped probes were suggested to produce an overestimation of estimated void fraction. Such irregularities were not observed for conical and wedge-shaped probes. The probe was further employed in PbBi-argon environment at temperature upto 350°C with measurements of local gas hold-up and local bubble counts. It is suggested that fine sensor tips are prone to physical movements induced by heavy LM multiphase flow.

Valls *et al.* (2020) performed detailed numerical studies aimed towards first reported development of flow regime maps for PbLi-He two-phase horizontal and vertical flows. Authors utilized volume of fluid method in OpenFOAM toolkit to characterize the lead-lithium/helium pair. The study stresses lack of experimental data towards validation of performed simulations. Authors investigated flow regimes in steady state case for different duct widths of 20 mm, 50 mm and 100 mm. For vertically upward flows, relevant to the work in this thesis, selected helium fractions varied in the range 0.1-0.9 and mixture velocities between 0.0001 m/s – 100 m/s. It is suggested that at very low velocities, simulation results are independent of the mixture velocity but are only dependent on helium fraction. Clear annular flow regime could be obtained at a void fraction of 0.7. The authors suggest some of the cases represent attributes of both bubbly and slug flows. It is suggested that the predicted PbLi-He flow regime needs adjustment in the currently available numerical model i.e. for water-air pair. Influence of duct width at a velocity of 0.001 m/s suggests at low void fraction, slug flow moves towards bubbly regime with an increase in the duct width, maintaining the bubble diameter. It is asserted that the validity of these flow regimes is expected under similar flow conditions and shall be validated by means of experimental investigations. Figure 2.1 below provides relevant cases for a duct width of 50 mm with a mixture velocity of 0.001 m/s and helium fractions of 0.1, 0.5 and 0.9.

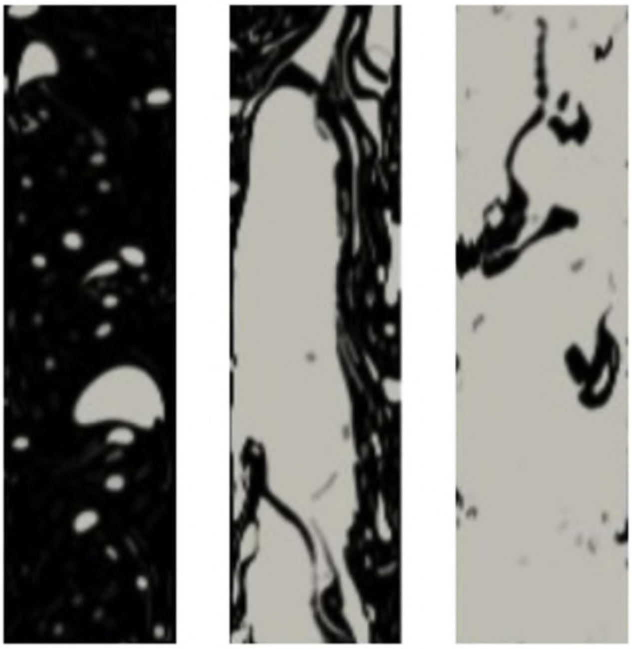

Fig. 2.1 Estimated flow regimes in PbLi-He flows for 0.1, 0.5 and 0.9 helium fractions (Source: Valls *et al.* (2020)).

2.2 CONCLUSIONS FROM THE LITERATURE SURVEY

Major observations derived from the literature review are presented below:

1. Most of the studies suggest experimental investigations to study the effects specific to LM scenarios in view of high density ratio between LM-gas and high surface tension inherent to LM environments. Some of the studies specifically highlight the deviations observed between aqueous systems and LM systems.

2. Most of the studies performed on LM two-phase flows are restricted to RT melting LMs (like GaInSn, Hg etc.) or low melting LMs (like Na, Rose's alloy, PbBi etc.).

3. Limited studies performed on high temperature LMs like Cu, Ag, Fe etc. preferentially utilized detection techniques like X-ray radiography, NR, pressure pulse method and resistivity probes.

4. Although non-contact radiation techniques like X-ray radiography, NR and gamma ray attenuation are applicable to high temperature opaque LM facilities, the required resources (including scintillator screens, lens arrangement, shielding blocks, radiation protection and licensing) alongwith limited penetration depth in the metallic pipes and within LM bulk for X-ray radiography renders the detection difficult. Additionally, surface obstructions like electrical heaters and thermal insulation for high temperature LM facilities make the technique less attractive.

5. Commercially available non-contact methods like ultrasonic transit time schemes and ECFM are restricted in terms of temperature as well as surface obstructions. Additionally, it has been demonstrated that ultrasound-based techniques are applicable only till low void fraction due to high amount of reflected echoes at higher void fractions. Methods like PIV require an optical window and seeding/tracer particles within the LM breeder, compromising its purity.

6. Simultaneous presence of magnetic field and nuclear radiation coupled with high temperature of LM systems in a nuclear fusion power plant may render the techniques like electromagnetic flowmeters, electromagnetic induction techniques and NR difficult in application.

7. Acoustic technique like pressure pulse technique, as studied for high temperature LMs including tin, lead, copper and in one case for PbLi, is restricted to the case where forced injection of gas is done from outside the LM circuit. However, such a technique cannot be utilized for bubbles generated within LM breeder, during accidental scenario (like a LOCA or LOHS) or to detect trapped gas pockets.

8. A localized detection of trapped gas pockets in complex manifolds typical in LM breeder circuits is rendered impossible considering the bulkiness of non-contact techniques.

9. Resistivity probes, although intrusive and localized, have been validated for their functionality against NR measurements in PbBi-N_2 flow loops and for very high temperature applications like in molten iron. The methodology can be adapted towards various LM scenario by proper selection of materials and is not much hindered by magnetic fields, irradiation, surface obstructions etc. Trapped gas zones within complex geometries and restricted zones can be well detected owing to miniaturization possibilities of the scheme.

2.3 OBJECTIVES AND SCOPE OF PRESENT STUDY

In view of the research gap identified from the detailed literature review presented above, the main objective of the present study is the development and validation of a two-phase detection probe for high temperature PbLi LM applications.

Scope of the experimental study is primarily divided into three parts. The details of these parts along with the different steps involved are depicted in Figure 2.2 below.

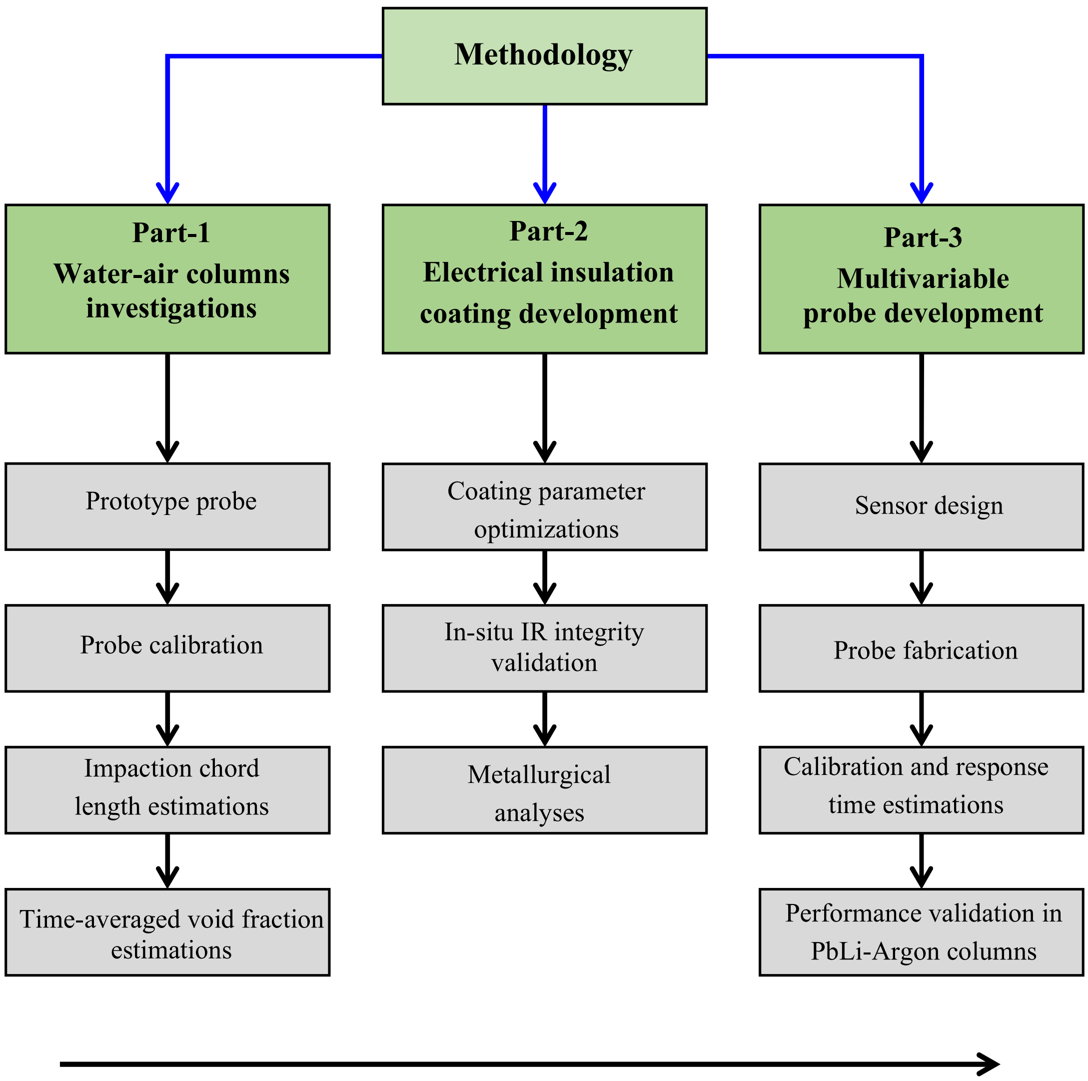

Fig. 2.2 Flowchart depicting thesis scope and workflow.

2.4 CLOSURE

In this chapter, a detailed and relevant literature survey has been performed on two phase detection studies conducted in LM environment. A greater emphasis has been placed on the utilized measurement techniques. In view of the above conducted survey, it is readily observed that two-phase detection studies for high temperature LM applications are severely limited. As such, no proper experimental study has been conducted to detect the presence of a two-phase regime in PbLi environment. The chapter also presents objectives and scope of the present thesis alongwith a framework of adopted methodology towards achieving the defined objective.

CHAPTER 3

EXPERIMENTAL INVESTIGATION: BUBBLE DETECTION IN WATER-AIR TWO-PHASE VERTICAL COLUMNS

3.1 INTRODUCTION

Two-phase flow is a commonly observed phenomenon in numerous industrial applications like thermal power plants, boilers and evaporators, hydrocarbon recovery systems, steel processing etc. In some processes, ingress of gas in liquid phase is intentional and desirable (Zheng and Zhu, 2018; Gajjar *et al.*, 2019). In specific to nuclear applications, a two-phase flow may occur due to specific configurational constraints within the facility or due to accidental scenarios. For instance, charging of a LM facility in presence of an inert cover gas may lead to trapped gas zones/dead pockets in inclined sections like nozzles for wetted configuration pressure transmitters (Saraswat *et al.*, 2016). Formation of re-circulation zones in complex structures and manifolds could also result in localized trapped gas regions. Even with proper gas venting arrangements, accidental scenarios like in-box TBM LOCA and LOHS (LM/water or LM/helium heat exchangers) could lead to ingress of gas phase within LM. An additional scenario (Kordac and Kosek, 2017) could lead to formation of helium bubbles within a lithium/lithium-based breeder/coolant like eutectic lead-lithium (PbLi) due to neutron interaction to produce tritium, which is the fuel for nuclear fusion reaction. Presence of this gas phase leads to hot spots within the reactor, reduced TBR as well as an improper shielding (Kordac and Kosek, 2017).

*This chapter is published in **Saraswat**, **A.**, **A. Prajapati**, **R. Bhattacharyay**, **P. Chaudhuri and S. Gedupudi** *Experimental investigations on bubble detection in water-air two-phase vertical columns*. pp. 555-566. *In* **A. Kumar, A. Pal, S.S. Kachhwaha,** and **P.K. Jain** (eds.) *Recent Advances in Mechanical Engineering. Lecture Notes in Mechanical Engineering*. Springer, Singapore, 2021.

It is, therefore, critical and imperative to detect occurrence of such a phenomenon to initiate proper remedial measures. Though the requirements for two-phase detection are well identified (Martsiniouk and Sorokin, 2000; IAEA technical meeting, 2006; Nuclear Energy Agency handbook, 2015; Lobanov and Pakhomov, 2017), a lack of proper diagnostics tools for high temperature applications (350°C-400°C) and compatible with corrosive liquid PbLi cannot be overlooked in specific to nuclear fusion applications.

As a first step to address some of the complexities involved in two-phase flow detection, experimental studies have been carried out in static water columns for detection and quantification of air pockets. Numerous tools, ranging from non-contact techniques like induction based measurements, gamma ray attenuation methods, ultrasound absorption technique etc. to contact techniques like electrical conductivity based and capacitance based detection probes, are readily available for low temperature two-phase flow detection and characterization studies (Anderson and Fincke, 1978; Saito *et al.*, 2005; Walker, 2010; Ariyoshi *et al.*, 2014; Gundrum *et al.*, 2016; Ratajczak *et al.*, 2017; Krull *et al.*, 2017; Stefański *et al.*, 2017; Stefani *et al.*, 2017; Huang *et al.*, 2018). However, present study takes into account the benefits and constraints in view of further adaptability towards liquid PbLi applications. In this study, an electrical conductivity principle based detection technique has been explored in detail owing to its better response, easier fabrication, relatively simpler operation, high temperature operational feasibilities and reduced installation requirements where non-contact techniques may prove challenging. For LM application, electrical conductivity principle is rather advantageous because of high electrical conductivity of the fluid itself. Secondly, only one probe is needed to be inserted; as the second conducting electrode can be configured using metal pipes of the facility itself. In this view, a prototype sensor probe is fabricated and simultaneous high speed imaging is performed to quantify relevant dimensions of air pockets colliding with the probe. Leverage of transparency from water medium in the present study provides visual corroboration before proceeding towards completely opaque LM applications.

3.2 EXPERIMENTAL METHOD AND APPARATUS

To fabricate the electrical conductivity sensing probe, two solid SS rods of 1.6 mm diameter are shaped in needle-point configuration and embedded in a slotted solid nylon rod. The slots are filled with an epoxy-resin based binder to provide electrical insulation and to hold the rods rigidly. Overall diameter of the sensor after fabrication is ~7.4 mm. The lengths of conducting bare SS electrodes are visually identified to be 1.5 mm and further confirmed by a handheld multimeter. Basic electrical circuit diagram with assembled components to gather output voltage signal, with and without interaction of an air bubble, alongwith principle of probe operation is demonstrated in Figure 3.1. The red section (AB) indicates electrically conducting exposed part of one SS rod in the medium, while the grey circles depict a vertically rising air bubble. Being a constant voltage excitation source, for bubble positions from (a) to (c), the voltage signal read by the Data Acquisition (DAQ) will remain the same due to availability of conducting path between exposed lengths of both the electrodes. Voltage signal dip across sensing resistor will begin as soon as the bubble completely encapsulates conducting portion of atleast one of the electrodes i.e. position (d) because of high electrical resistivity of surrounding air. At this point, conduction current through the encapsulated electrode is nil, but very low insulation leakage current flows, giving rise to a drop in circuit current. After point (f), when some portion of the conducting electrode is exposed to water again, the voltage will rise rapidly to achieve its normal value due to re-established electrical continuity.

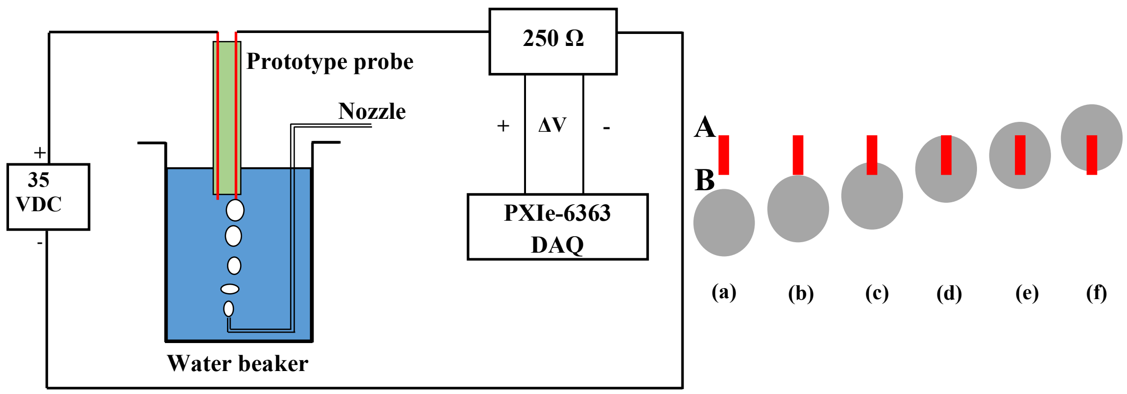

Fig. 3.1 Basic circuit diagram and the operational principle of electrical conductivity probe.

Hence, a detectable air pocket requires thickness greater or atleast equal to the exposed length of conducting electrode. To carry out preliminary studies towards detection of two-phase in static water column, an experimental facility is fabricated which consists of a glass beaker with dimensions 150mm (L) X 150mm (W) X 200mm (H). A square cross section reduces lens effects, ensuring correct dimensional measurements of injected air pockets using a camera and ruler arrangement. A primary SS nozzle with a 3-mm bore is installed in the beaker with a provision to vary bore diameter by installing a 24-gauge hypodermic needle (ID = 0.3 mm) on top of the primary nozzle. An air compressor with downstream pressure regulator and needle valve assembly is used to regulate injected air flow into the static water column. High speed imaging is performed at 60 Frames Per Second (FPS) to register the trajectory of traversing bubbles through optical chamber facility. For a fixed pressure downstream, nozzle generates an array of bubbles with approximately regular time interval in between. A Laboratory Virtual Instrument Engineering Workbench (LabVIEW) platform based application is developed to log and display real time data at 5 ms interval using PCI eXtensions for Instrumentation (PXIe-6363) module. To capture finer details of interactions between the bubbles and electrode, developed application also provides data logging at 1.5 MHz sampling rate.

3.3 DATA ANALYSIS, RESULTS AND DISCUSSIONS

3.3.1 Trajectory And Probe Interaction Analysis For Bubbles Generated Using Hypodermic Needle

The probe location is fixed in a manner that all the ejected bubbles hit one of the electrodes. The captured rise trajectory for an array of 07 bubbles is shown in Figure 3.2. The corresponding distinct 07 V-shaped voltage dips, as shown in Figure 3.3, confirm detection of all the bubbles. The encircled region (red) after second voltage dip depicts the residence time of the second bubble, stuck at the probe bottom, interacting intermittently with the electrode before getting hit by the third bubble. This phenomenon is clearly visible at 120 FPS. Such observation further corroborates sensitivity of fabricated probe towards two-phase detection.

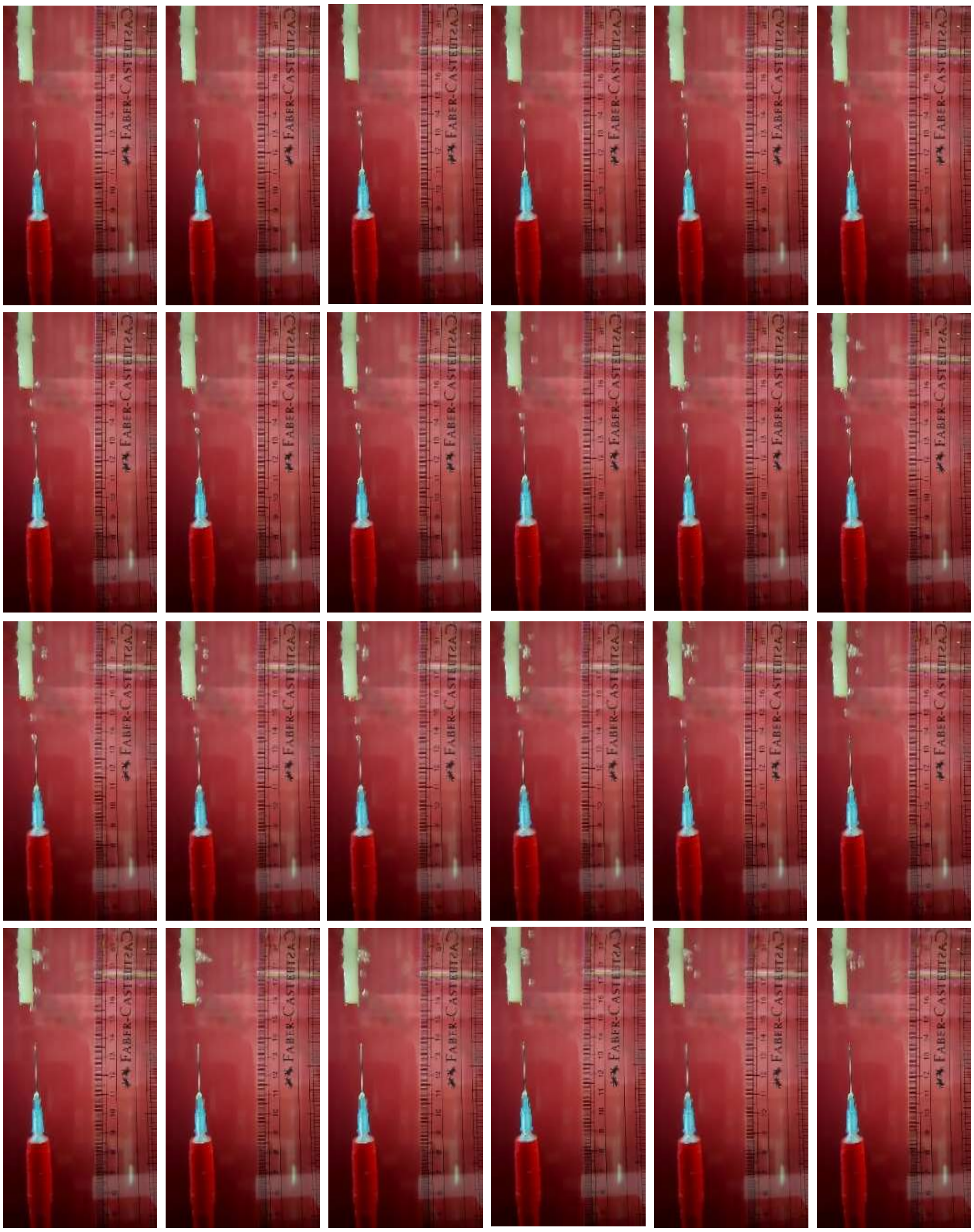

Fig. 3.2 Trajectory of bubbles generated from hypodermic needle towards probe.

An arbitrary threshold voltage sets a datum to calculate voltage dip time and therefore, bubble traversing time. Impact of the threshold selection is discussed later during air pocket thickness estimations. A ruler set within the plane of generated bubbles coupled with imaging field-view normal to this plane provides the necessary means to measure dimensions of air pocket just after ejection and thereafter, to analyze distortions during rise in the column.

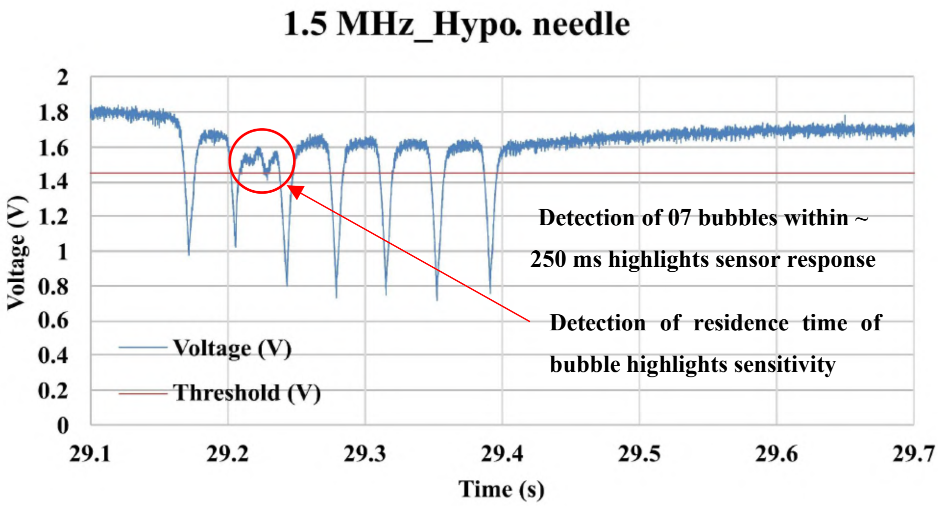

Fig. 3.3 High frequency sampling of probe voltage for bubbles generated through hypodermic needle.

Representative sets of extracted frames are further used to calculate average vertical velocity component of rising air pockets from projected vertical displacement against the ruler and number of image frames to estimate the time utilized for that displacement. For each bubble analyzed, vertical velocity is calculated using top reference, bottom reference and center reference with reference to the instantaneous bubble profile. Average vertical velocity is then calculated using an average of the velocities for all the analyzed bubbles of selected sets for a selected reference position.

An important observation from visualization study is that smaller diameter bubbles do not tend to distort much, but acquire a convex/dome shape with a dent at the bottom, which could be accounted for a vertical differential pressure. This observation is highlighted in Figure 3.4 for frames taken just after release of a bubble and just before its impact with the probe respectively. Estimated envelope dimension for the air pocket is approximately 4 mm using projections (yellow) against the ruler. However, as the top and bottom of the pocket have nearly similar convex curvatures, it can be seen that along the conducting electrode axis, the air pocket thickness is always less than 4 mm (~approximately 3 mm as traced using a freeform shape outline).

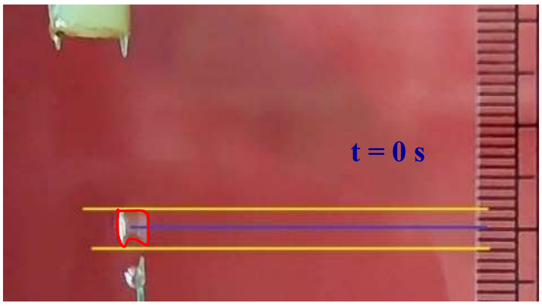

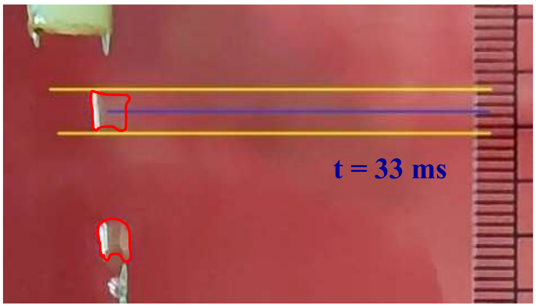

(a) (b)

Fig. 3.4 Close up views of an air bubble depict a convex shape: (a) just released from the hypodermic needle; (b) after ~33 ms from the first frame.

3.3.2 Trajectory And Probe Interaction Analysis For Bubbles Generated Using 3-mm Bore Nozzle

Similar methodology is applied to the bubbles generated from 3-mm bore nozzle. The captured bubble trajectory is shown in Figure 3.5 while the logged voltage data for a sample case is presented in Figure 3.6, respectively. Variation in the magnitude of voltage dips can be explained by the difference in sizes and difference in the ways of interactions. A smaller sized air pocket generates a lower magnitude voltage dip as it traverses across the electrode relatively faster compared to a bigger sized pocket. Figure 3.4 may be contrasted with Figure 3.7 to analyze distinctly visible distortions and flattening of air pockets of larger diameter within same time frame.

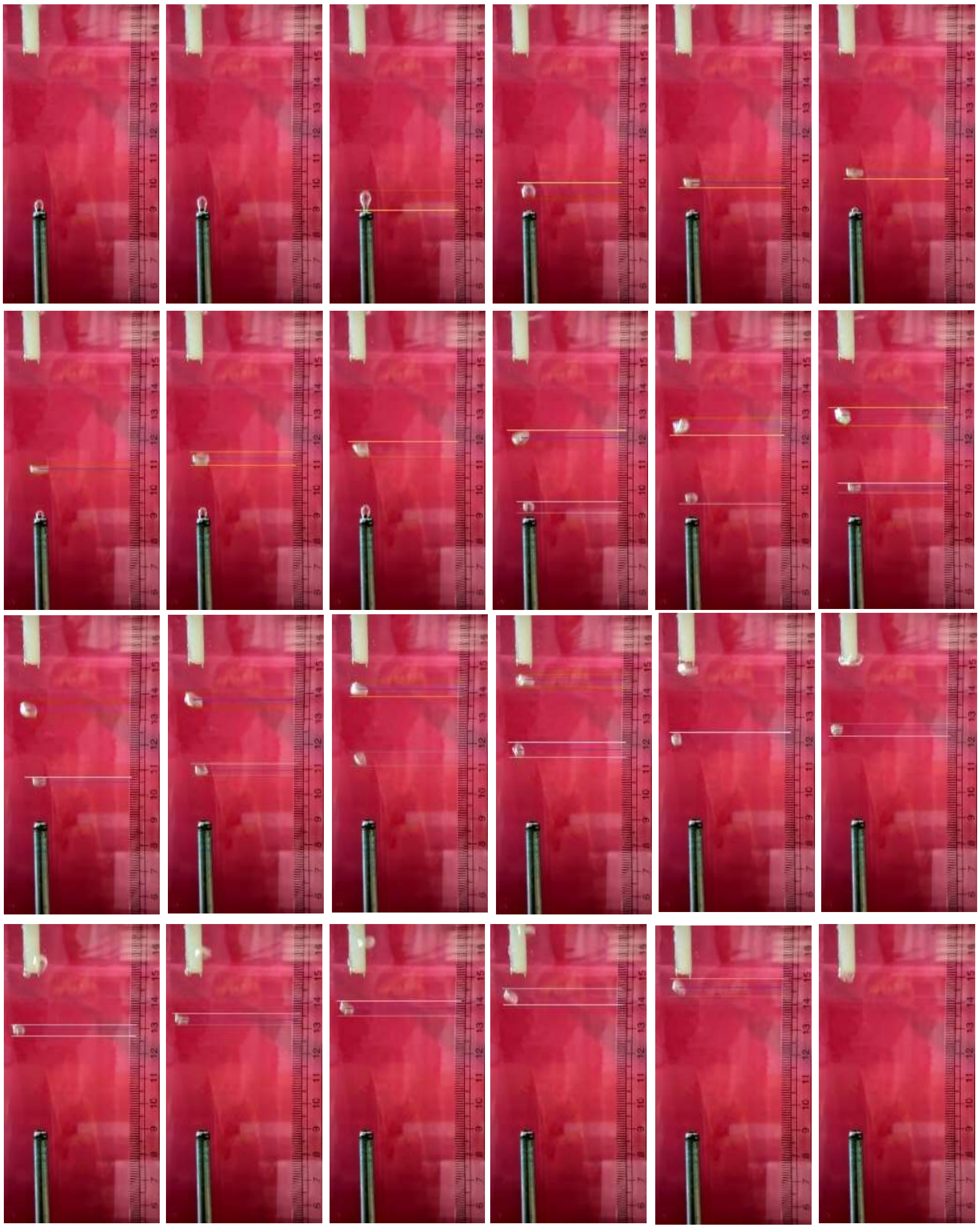

Fig. 3.5 Trajectory of bubbles generated from 3-mm bore nozzle towards probe.

Another critical observation is that the air pockets tend to have a non-zero horizontal velocity component, which may depend on the density of surrounding liquid phase. A higher liquid-gas density ratio (similar to heavy LM scenario) may force the air pockets to rise vertically upwards along the least resistance path.

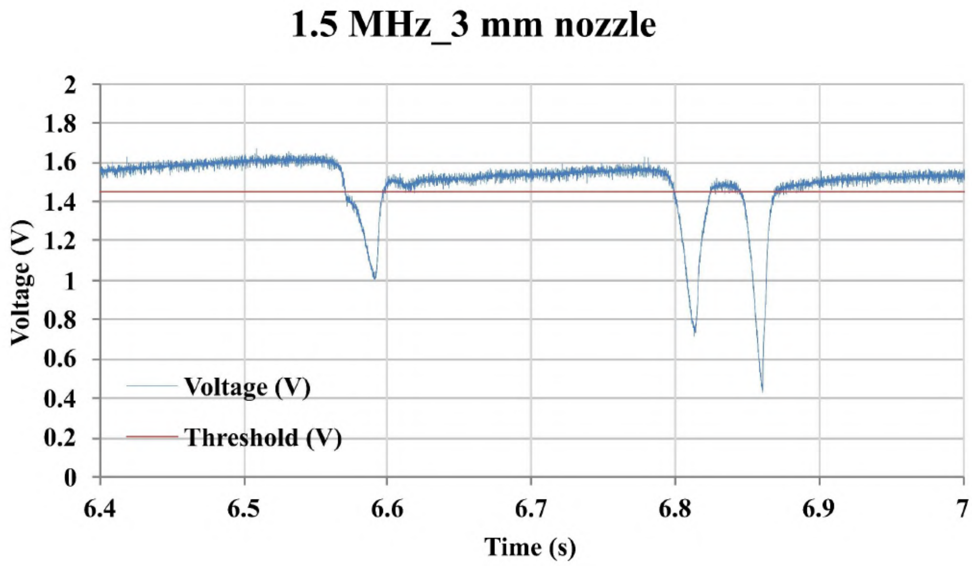

Fig. 3.6 High frequency sampling of probe voltage for bubbles generated through 3-mm bore nozzle.

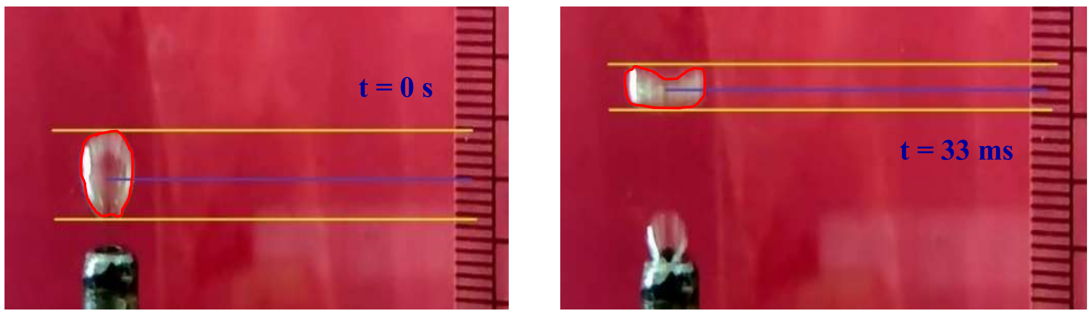

(a) (b)

Fig. 3.7 Close up views of visible dimensional distortions in an air pocket: (a) just released from 3-mm bore nozzle; (b) after ~33 ms from the first frame.

3.3.3 Calibration Of Probe Prototype

Although sub-microsecond logging is strikingly advantageous for offline data processing to gain detailed insights, it is highly desirable to monitor and detect presence of bubbles in real time during facility operations. To achieve this, a 0.2 kHz sampling rate is selected based on the analysis of characteristic V-shaped voltage dips from previous samples so as to acquire enough information for a conclusive detection of an air pocket. This calibration, performed with an input supply of 35 VDC (operating in a constant voltage mode) and output tapped across a 250 Ω resistor, holds true for a sampling interval of 5 ms. A precise calibration may be obtained with a higher sampling frequency. Table 3.1 reports the weighted averages for a number of sample sets to arrive at the calibration voltage output signals.

Table 3.1 Calibration details for prototype probe.

Condition	**No. of sample sets**	**No. of samples**	**Weighted average (V)**
Water medium (no bubble)	-	> 5,00,000	1.872 volts
Bubble from 3-mm bore nozzle	05	1098	1.053 volts
Bubble from hypo. needle	10	1107	1.397 volts

It should be noted that for a same sized air pocket, voltage dip depends on the way of interaction between the bubble and electrode(s) as well as on the sampling rate. A low frequency sampling may result in an over estimation of output voltage during bubble interaction (refer data from Table 3.1 at 0.2 kHz sampling and magnitude of dips from Figure 3.3 and Figure 3.6 at 1.5 MHz sampling). Dip in the voltage also depends on the distorted profile and vertical alignment of an air pocket along the sensing probe. However, average dips measured (~820 mV for 3-mm bore nozzle and ~475 mV for hypodermic needle) at 0.2 kHz sampling suffice to detect presence of an air pocket in the water column. Figure 3.8 presents voltage data against representative samples for a continuous ingress of high pressure gas phase into liquid phase, approximately simulating an in-box TBM LOCA/LOHS accident. As observed, the flow configuration appears to be jet-like/churn flow with extremely disordered bubble motions. Presence of a wide range of bubble diameters is corroborated by voltage dips of different magnitudes. A continuous 3 h duration performance test in such an agitated column corroborates no drift/degradation in the calibration signal for the fabricated probe.

(a)

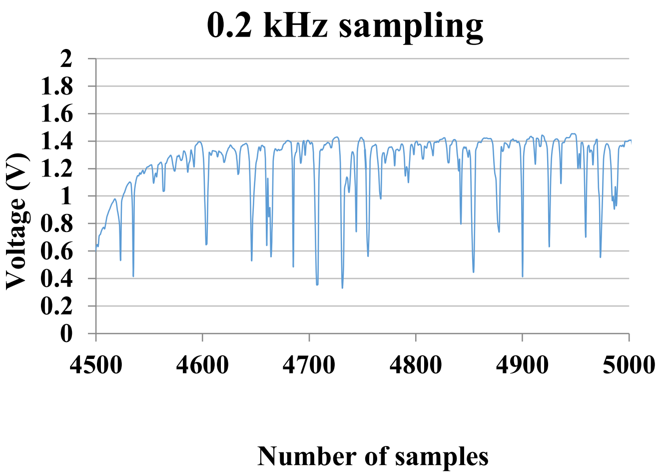

(b)

Fig. 3.8 Performance of prototype probe for extremely agitated flow (similar to a jet flow): (a) frame for the generated flow; (b) logged voltage data.

3.3.4 Estimations Of Air Pocket Thickness

Assuming symmetricity in the V-shape dips of voltage profiles, voltage dip time is estimated as half of the total time between the points where the voltage curve intersects preset threshold. Product of the calculated average vertical velocity with the estimated voltage dip time gives effective air void thickness (*d*) additional to the encapsulated conducting portion of electrode (*l*). Thus, the total effective air pocket thickness is estimated by summing the two components (*l*+*d*) as elaborated in Figure 3.9. Estimated average velocity for smaller bubbles varied between 0.32-0.35 m/s while that for larger bubbles varied between 0.25-0.26 m/s.

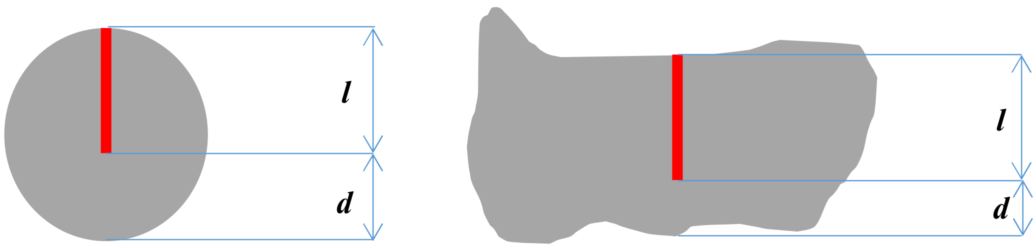

(a) (b)

Fig. 3.9 Estimations of air pocket thickness: (a) spherical pocket; (b) distorted pocket.

Estimated average air pocket thicknesses (Y-axis) against sample number (X-axis) for two sets each of bubbles generated from hypodermic needle and 3-mm bore nozzle with different thresholds are shown in Figure 3.10. For a given threshold, samples 1 to 3 represent average pocket thicknesses for the first set considering bottom, center and top references for velocity calculations. Similarly, samples 4 to 6 represent corresponding quantities for the second set. As observed, a change in threshold level significantly impacts estimated pocket thickness. In these calculations, for a given case, the pocket thickness is calculated by using a common threshold level for all the voltage dips.

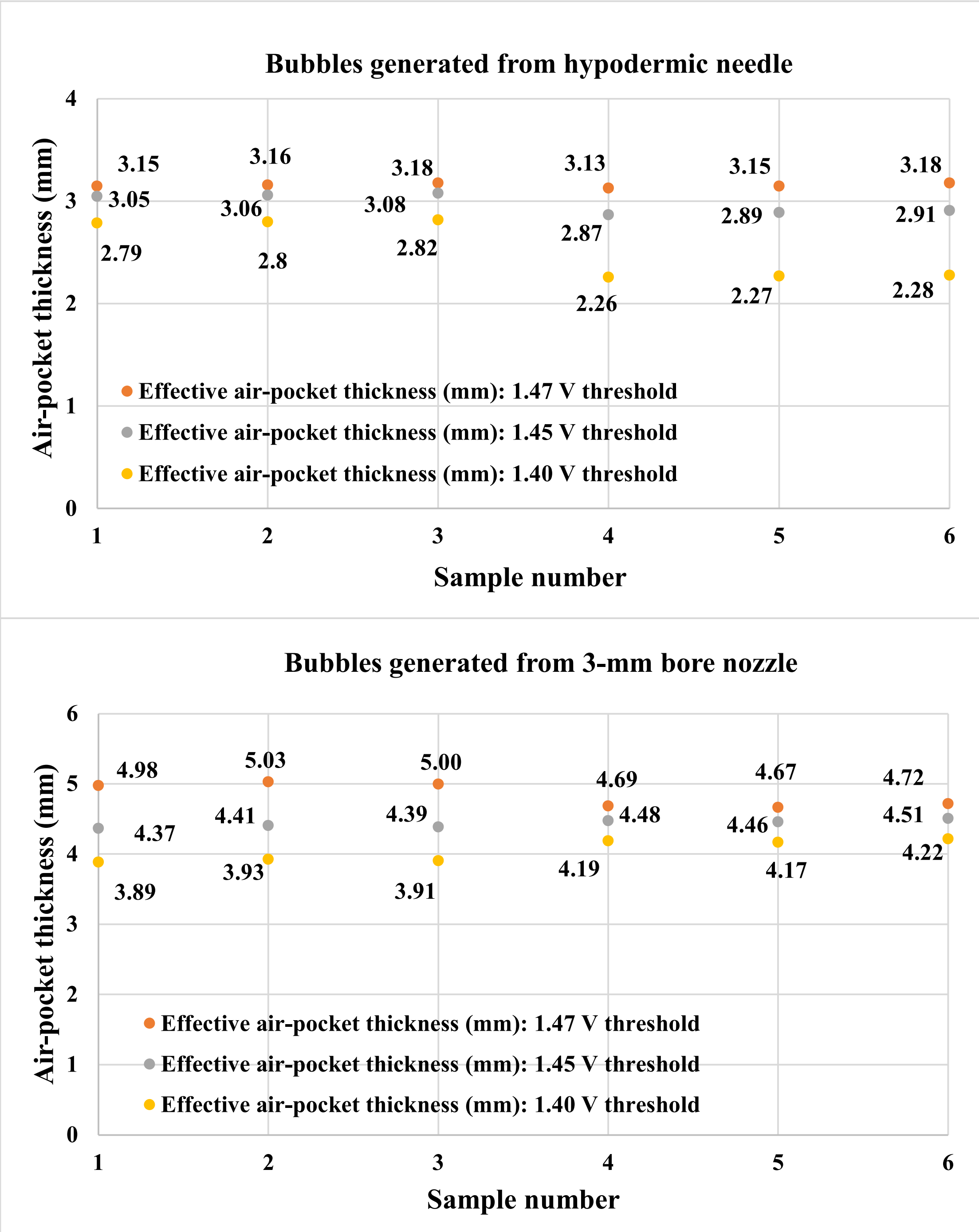

Fig. 3.10 Impact of threshold voltage selection on estimated air pocket thicknesses for bubbles generated: from hypodermic needle; from 3-mm bore nozzle.

However, for an exact thickness calculation, each air pocket must be analyzed individually because the dip for each pocket depends on its way of interaction with the probe. In the present case, threshold levels of 1.45 V and 1.47 V seem to predict air pocket thicknesses with relatively higher accuracy as could be confirmed from projected dimensions against the ruler for the case of smaller bubbles. However, an exact error analysis requires considerably higher frame rate imaging tools alongwith distance measurements at sub-mm level, which are limited in the present study. In the present study, an exact error quantification may not be possible but it can be concluded that the thickness of air pockets could be estimated within sub-mm accuracy.

3.3.5 Preliminary Attempts To Estimate Local Void Fractions

Threshold method is utilized to estimated time-averaged void fractions in the static water column using an excel logic, which assigns normalized values of 0 or 1 by comparing the probe circuit voltage with the preset threshold. Basic underlying assumption is that during the rise time, till the voltage intersects threshold limit, the air pocket encloses point A of the electrode ("A" defined in Figure 3.1). Ratio of time duration for which logic remains LOW (0) to the total time duration under consideration is defined as the local time-averaged void fraction at the point "A". For a particular representative case shown in Figure 3.11, utilizing a threshold level of 1.45 V, a time-averaged void fraction of ~ 16.15% is estimated for the selected time duration of 0.4 second.

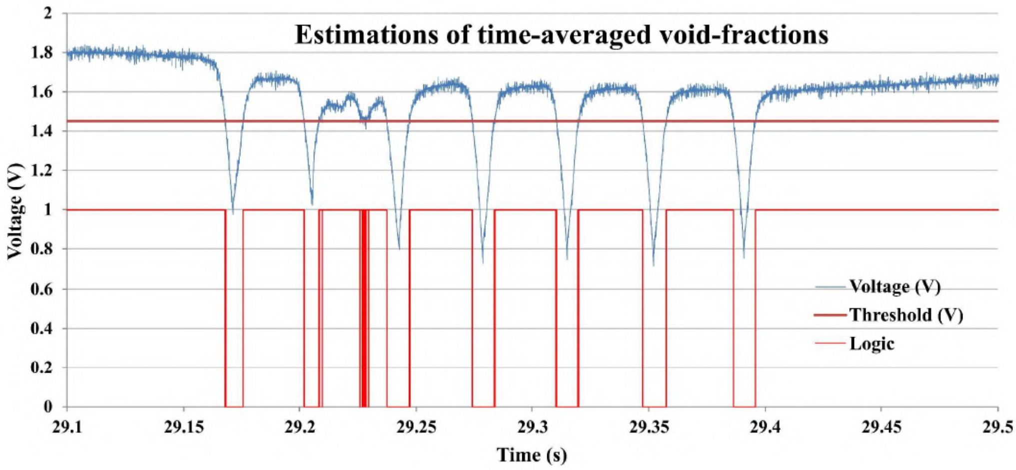

Fig. 3.11 Threshold method to estimate time-averaged void fraction in two-phase water-air column.

3.4 FUTURE PLANS

Future activities include gas pocket detection in flowing water facility with forcedly injected gas bubbles. Additionally, to cover a wider flow cross-sectional area, a sensor array assembly is being planned for testing and initial validations with gas sparger arrangements in a vertical water-air two-phase column. The design of the sensor array assembly and final assembled array are shown in Figure 3.12 and Figure 3.13, respectively.

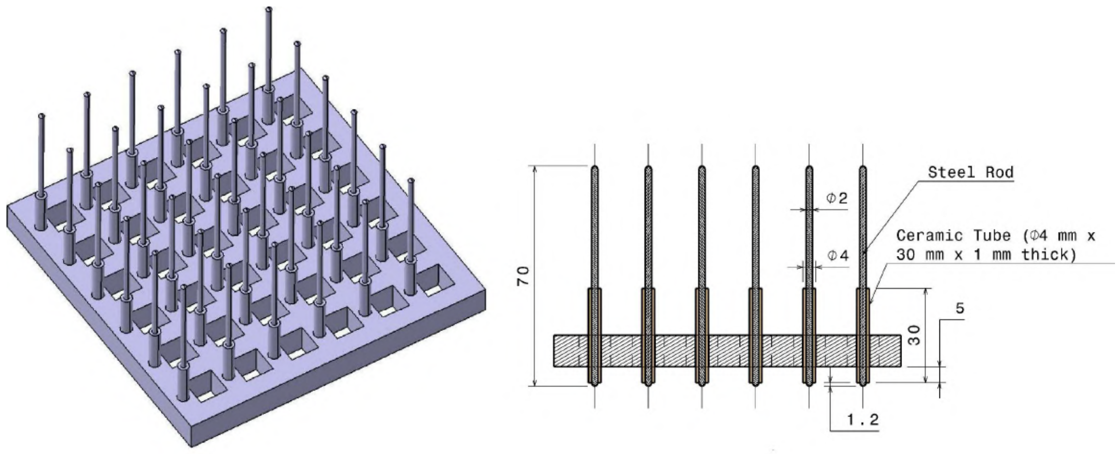

Fig. 3.12 3D view and dimensional schematic of the proposed sensor array assembly for detection of gas bubbles over a wider cross-section.

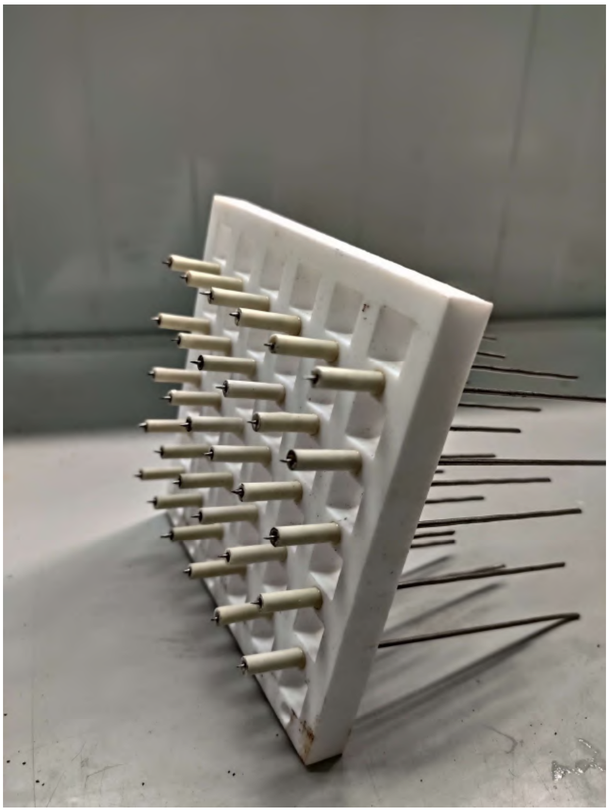

Fig. 3.13 Assembled sensor array configuration.

3.5 CONCLUSION

The major conclusions derived from the first experimental study are mentioned below:

- The necessary software tools along with measurement scheme for two-phase detection in a gas-liquid column have been identified.
- A sampling frequency of 0.2 kHz suffices for a real time detection of air pockets rising in water medium.
- An electrical conductivity based detection scheme could resolve all the bubbles colliding with the probe.
- A synchronous imaging technique could provide means for quantitative estimations i.e. to estimate the velocity and impaction chord length of rising air bubble.

3.6 CLOSURE

In this chapter, relevant details are discussed for an experimental study performed towards quantification of air pockets in water-air two-phase vertical columns. A test facility suitable to address experimental requirements is fabricated with provisions of generating different diameter bubbles at different injection frequencies. Present study sets a reference towards experimental activities in opaque liquid PbLi two-phase flow detection studies. The next chapter presents detailed experimental investigations on the validation and performance of an electrical insulation coating in PbLi LM environment intended to assess the adaptation feasibility of electrical conductivity based scheme towards two-phase detection in PbLi scenario.

CHAPTER 4

EXPERIMENTAL INVESTIGATION: ELECTRICAL INSULATION PERFORMANCE OF ALUMINA COATINGS FOR HIGH TEMPERATURE LEAD-LITHIUM LIQUID METAL APPLICATION

4.1 INTRODUCTION

LM based BB concepts like Helium Cooled Lithium-Lead (HCLL), Water-Cooled Lithium-Lead (WCLL), Dual-Coolant Lithium-Lead (DCLL) and LLCB provide several key advantages including low vapor pressure, high thermal conductivity, circulation ability enabling tritium extraction outside the blanket as well as stability under radiation environment typical for a fusion reactor. However, presence of a transverse magnetic field significantly modifies flow geometry of an electrically conductive fluid due to imposed Lorentz force, posing high demands on the required pumping power to compensate for resulting pressure drops. Successful materialization and utilization of such LM ancillary systems in a fusion power plant requires optimization of process parameters including MHD pressure drop reduction, which mandates an electrical isolation between the LM and structural material (Malang *et al.*, 1995; Mitsuyama *et al.*, 1998; Smolentsev *et al.*, 2005; Shikama *et al.*, 2008; Bühler and Abdou *et al.*, 2015; Mistrangelo, 2018; Fernández-Berceruelo *et al.*, 2018; Rowcliffe *et al.*, 2018; Rapisarda *et al.*, 2018; Giulio *et al.*, 2020; González and Kordac, 2020).

*This chapter is published in **Saraswat, A.**, **C. Sasmal**, **A. Prajapati**, **R. Bhattacharyay**, **P. Chaudhuri and S. Gedupudi** (2022) Experimental investigations on electrical-insulation performance of Al_2O_3 coatings for high temperature PbLi liquid metal applications. *Annals of Nuclear Energy*, **167**,108856.

Such an electrical insulation, by virtue of its non-porosity towards LM ingress, is also envisaged to act as a corrosion protection layer as well as Tritium Permeation Barrier (TPB) (Tanaka *et al.*, 2000; Shikama *et al.*, 2008; Chikada *et al.*, 2009; Zhang *et al.*, 2012; Wulf *et al.*, 2013; Singh *et al.*, 2014; Abdou *et al.*, 2015; Gazquez *et al.*, 2017; Rapisarda *et al.*, 2018; Utili *et al.*, 2019; Iadicicco *et al.*, 2019). Additionally, development of a few specific diagnostic tools for LM systems, like two-phase detection schemes based on electrical conductivity principle, necessitates provision of an electrical isolation over a substantial immersed length (Saito *et al.*, 2012; Nuclear Energy Agency Handbook, 2015; Muñoz-Cobo *et al.*, 2017). For such applications, a candidate insulation must be demonstrated for its compatibility with corrosive media, endurance towards high operational temperatures and integrity of electrical insulation over long operational durations without substantial degradation.

Numerous experimental and simulation studies are being carried out worldwide towards performance qualification of functional materials which can cater to above needs either in the form of a coating or as Flow Channel Insert (FCI), with Al_2O_3, Er_2O_3, SiC identified as potential candidates in particular (Malang *et al.*, 2009; Tosti *et al.*, 2013; Abdou *et al.*, 2015; Smolentsev *et al.*, 2015; Courtessole *et al.*, 2016). However, a scarcity of relevant experimental data could be observed towards quantitative performance assessment of electrical Insulation Resistance (IR) for coated substrates over long duration exposure to PbLi environment at relevant temperatures. IPR is working in the areas of MHD, corrosion studies of structural materials and development of a two-phase detection technique relevant to liquid PbLi applications (Atchutuni *et al.*, 2018; Kumar *et al.*, 2019; Saraswat *et al.*, 2021). In this view, to address the crucial requirements of an electrical insulation for further advancements in LM domain, a preliminary performance investigation was carried out for aluminium monophosphate bonded Al_2O_3 based electrical insulating coatings deposited over SS-316L substrate electrodes. Al_2O_3 was preferentially chosen as the coating material of interest for its thermodynamic and chemical stability over temperature range of interest, while the selection of substrate material was largely dominated by its commercial availability, inexpensiveness and proven usage as structural material and wetted parts of diagnostics in small scale PbLi R&D facilities. One of the major challenges in the application of ceramic coatings over SS-316L substrates is the wide difference between Coefficient of Thermal Expansion (CTEs) of the two materials over operational temperature range of interest. Through various experimental runs, optimization of heat treatment parameters was achieved successfully to develop Al_2O_3 coated SS-316L electrodes. Adopted coating application process allows for desired variations in the yielded coating thicknesses. Details of the application methods, performance tests in static liquid PbLi and metallurgical observations are presented in the following sections.

4.2 EXPERIMENTAL METHODS AND MATERIALS

Previous works have well demonstrated successful Al_2O_3 growth over substrates of SS-304L, SS-316L, P-91 and Reduced Activation Ferritic-Martensitic (RAFM) steels alongwith an excellent corrosion resistance observed against static and flowing PbLi (Jamnapara *et al.*, 2014; Gazquez *et al.*, 2017; Paul *et al.*, 2018; Vassallo *et al.*, 2018; Wulf *et al.*, 2018; Iadicicco *et al.*, 2019). A few efforts have also been made towards in-situ validation of solid high purity Al_2O_3 pieces as electrically insulating FCI in PbLi environment (González *et al.*, 2020). However, no reported study provides relevant long duration performance data on IR for Al_2O_3 coated substrates to address critical issues related to MHD pressure drops and development of diagnostics, as highlighted above. Additionally, during the present study, it was repeatedly observed that the plasma assisted tempering and thermal tempering (Jamnapara *et al.*, 2014; Sree *et al.*, 2014) of hot-dip aluminized SS-316L substrates resulted in an electrically conductive layer, which could be verified even at a macroscopic level, suggesting incomplete transformation to Al_2O_3. The study also resulted in substrate deformation due to high temperature exposure requirements. It may, therefore, be concluded that such coating application methods demand independent sophisticated optimization of parameters for different substrate materials. However, this further needs to be investigated in detail. In the present study, with an aim to homogenize the coating application method towards various substrate materials, a refractory coating suspension of aluminium monophosphate bonded calcined Al_2O_3 with 99.8% purity (containing ~ 75% solids by weight) has been investigated on 1.6 mm thick solid electrodes of SS-316L. Pre-coating preparation of the substrate includes surface roughness induction using grade-80 emery paper followed by acetone application for removal of dust, grease and foreign particles to allow for a better adhesion between the coating and the substrate. The coating was applied in two steps:

a) dip coating for 30 seconds and
b) manual brush coating on the surface of the electrode.

To ensure the experimental objective of in-situ IR measurements in electrically conducting PbLi, tip of the electrode was provided with an additional dip cycle in the same coating suspension, resulting in a blob-shaped coating deposition. Thereafter, coated samples were provided an air-set for ~ 24 h in a vertical orientation (coated probe tip at the top). Gradual retraction of the coating material under gravity allows the suspension to fill any remnant voids and undulations intentionally induced by surface roughening. This air-set period, acting as a necessary drying and pre-bonding stage, was followed by high temperature heat cure in a muffle furnace with the coated electrode(s) arranged in a horizontal orientation. High temperature heat cure involves following stages:

a) Ramp-up time of 2 h from RT to 93°C followed by a 2 h heat cure at 93°C. This step was intended towards gradual dehydration of the coating.

b) Ramp-up time of 2.5/10/12 h from 93°C to 427°C followed by a 2 h heat cure at 427°C. This step was intended towards achieving a good bond between Al_2O_3 and SS substrate.

c) A natural cool down from 427°C to RT.

Post heat treatments, absence of any voids/cracks was ensured through visual inspections using a magnifying glass, followed by high voltage IR measurements at RT for one of the fabricated probes. The in-situ IR measurement scheme for PbLi environment is depicted in Figure 4.1. To the best of our knowledge, this is the first time in-situ high voltage IR measurements are employed for Al_2O_3 coated substrates in PbLi environment over long duration experimental studies.

Test set up consists of a PbLi tank provided with surface mount electric resistive heater in a temperature feedback based Proportional-Integral-Derivative (PID) control loop and ports for vacuuming, gas feeding/purging and venting. Three coated probes, namely P1, P2 and P3, were fabricated as per the procedure described above. However, for P2 & P3, the fully heat cured layers were further deposited with an additional brush coated layer to allow for gradual heat curing through system operations over long duration. P2 was installed as such in the PbLi tank while P3 was first dehydrated at 93ºC for 2 h (step (a)) prior to installation in the tank. A bare SS-316L electrode (A), inserted through the third port, acts as a reference conducting electrode for IR measurements. PbLi in the tank was melted and heated upto a temperature of 300°C for a duration of ~15 h in Ultra High Purity (UHP) grade argon gas environment with repeated argon purging to maintain an inert environment.

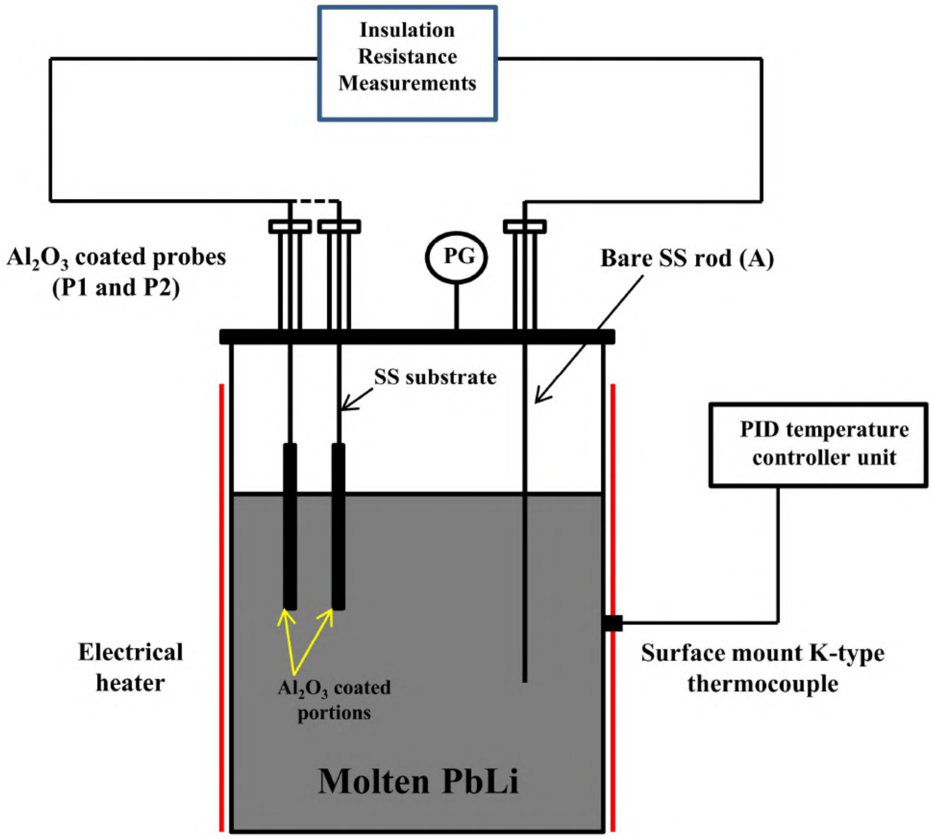

Fig. 4.1 Insulation resistance measurement scheme for Al_2O_3 coated probes in PbLi liquid metal.

A positive cover gas pressure was maintained over complete test duration. After liquefaction of PbLi (melting point observed at ~235°C-236°C), coated probes and the bare SS-316L electrode (A) were immersed in PbLi. The electrical resistance between A and the test facility structure was < 1 Ω, ensuring a good electrical contact.

Leverage of high electrical conductivity of PbLi (Schulz, 1991; Martelli *et al.*, 2019) was taken to measure IR of immersed probes being equal to the measured resistance between accessible conducting parts of the coated probes (Px, x = 1,2,3) and the electrode A. P1 and P2 were tested during test campaign-1 while P3 was tested during campaign-2. High voltage insulation tests were performed at regular intervals over complete duration of test campaigns including thermal cycles at the end.

Temperature derating factors, signifying the ratio of IR at any given temperature to the IR value at base temperature, were estimated during last thermal cycle for every 10°C rise in temperature from the base temperature. Test campaigns were concluded with final IR measurements to observe cumulative degradation effect on the IR due to thermal aging, corrosion and thermal cycling. Post completion of test campaigns, samples of ~ 8 mm length were cut across the cross-sections using a diamond wire cutter (Make: Gatan, wire diameter: 200 µm) followed by gold sputter coating of the samples for Scanning Electron Microscopy (SEM) and SEM-Energy Dispersive X-ray (EDX) analysis. Metallurgical analyses on the prepared samples were carried out for coating thickness estimations, microstructure evaluations and LM ingress detection. Particle size measurements were performed using SEM-image analysis software and open source imageJ software tool.

4.3 RESULTS AND DISCUSSIONS

4.3.1 Coating Observations

The adopted dip coating method resulted in a relatively thinner (~150-200 µm) wet film layer over the substrate. As depicted in Figure 4.2, a short ramp-up time (2.5 h/ 4 h) for heat treatment (step (b)) resulted in visible cracks along the coated length with formation of surface blisters, which can be attributed to a larger differential thermal expansion and sudden dehydration of the coated suspension, respectively.

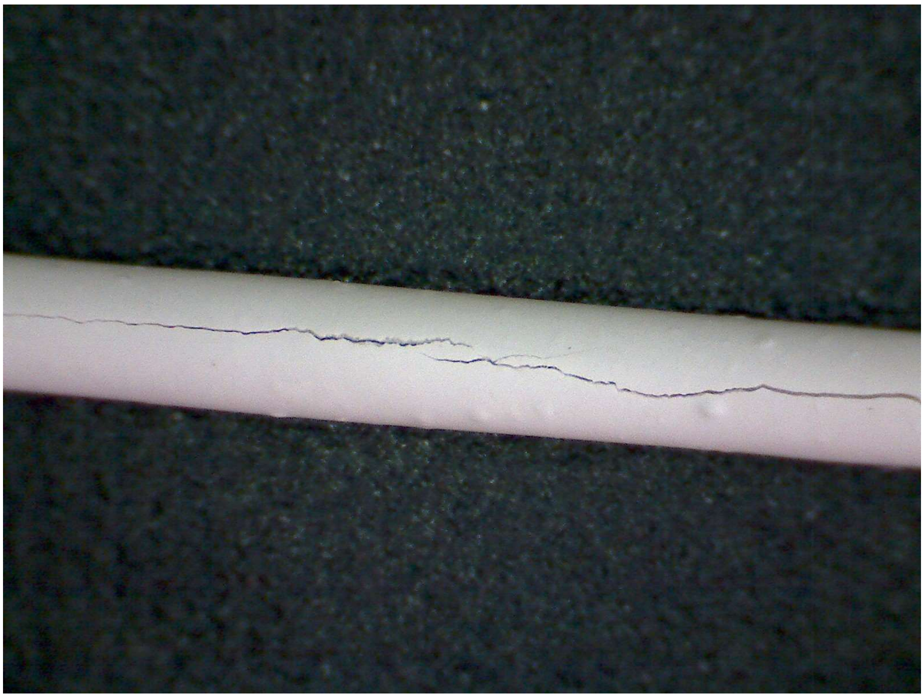

Fig. 4.2 A full length crack with blisters on deposited Al_2O_3 coating due to short temperature ramp-up time.

Although a longer ramp-up time (~ 10 h to 12 h) greatly minimized the cracks and blisters during first heat cure, complete elimination of very fine cracks could not be achieved. Hence, additional coating layers deemed necessary repeating the application steps until no visible cracks were identified. The IR at RT for one of the successfully fabricated probes, prepared with a single dip coat cycle followed by full heat curing, was found to be exceptionally high providing an insulation leakage current of < 1 nA. In view of highly brittle nature of Al_2O_3, preliminary non-destructive investigations were carried out using a calibrated portable Universal Serial Bus (USB) microscope for estimation of coating thicknesses using average diametrical measurements as shown in Figure 4.3(a) and Figure 4.3(b). Detailed average coating thickness estimations across the cross-section (destructive examinations) using SEM for the tested probes are presented under dedicated section on metallographic investigations.

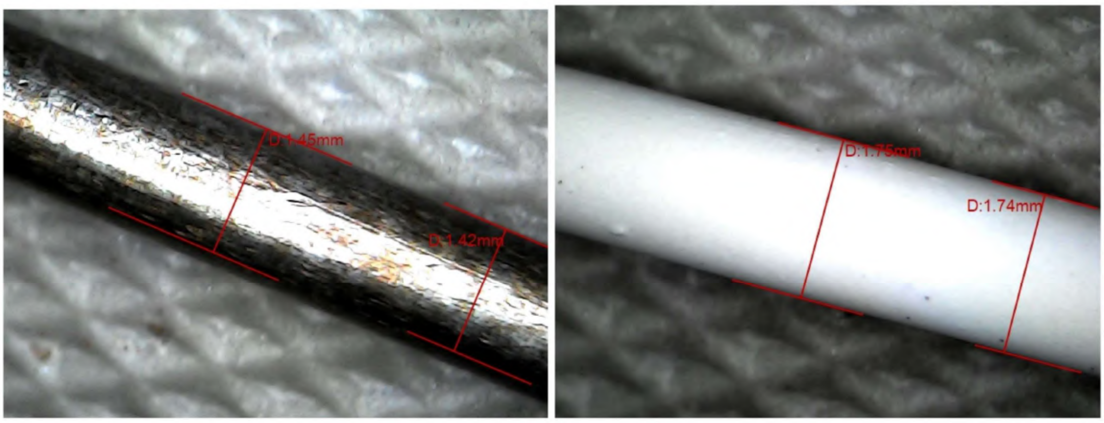

Fig. 4.3(a) Al_2O_3 coated SS-308L electrode (coating thickness ~155 µm).

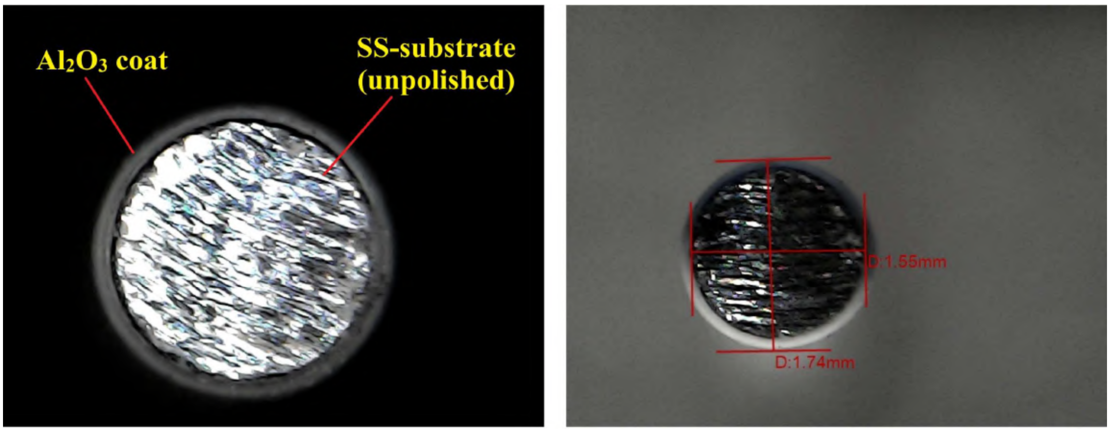

Fig. 4.3(b) Al_2O_3 coated SS-316L electrode with bare SS tip (coating thickness ~95 µm).

Details of the probes tested for compatibility with PbLi are summarized in Table 4.1 below. All weight measurements were done using a calibrated precision weighing balance (Sartorius make, CPA225D) with a resolution of 10 µg.

Table 4.1 Details of fabricated probes tested under test campaign-1 and test campaign-2.

Test campaign	Probe identification	Coated length (mm)	Weight (g)
1	P1	~85	8.57521 ± 0.00001
	P2	~65	7.45867 ± 0.00001
2	P3	~60	7.66220 ± 0.00001

4.3.2 Performance Validation In Liquid PbLi Environment

4.3.2.1 Test campaign-1

Temperature variations with time duration details for the test campaign-1 are depicted in Figure 4.4. The red markers (circle) on the plot represent instances of in-situ high voltage IR tests using the scheme shown in Figure 4.1. Measured IR values with time and temperature are mentioned in Table 4.2. All IR measurements were taken 60 s after high voltage application to minimize the effects of capacitive charging current and dielectric absorption current (Megger guide, 2006). A decrease in the IR was observed for both P1 and P2 with an increase in the temperature from 300°C to 350°C, an expected temperature based derating phenomenon in insulators. However, for P2, during 260 h in static PbLi at 300°C, an increase in the IR value was observed which could be accounted for gradual heat curing of the uppermost untreated coat layer over long operational durations.

From the measured IR performance data, immediate observable advantages of the adopted coating method include selective coating/masking of difficult substrate geometries including the internals of pipe-sections and complex manifolds, easy application without exposure of substrate to very high temperatures as required in the previous reported works (Malang *et al.*, 1995; Shikama *et al.*, 2008; Zhang *et al.*, 2012; Wulf *et al.*, 2013; Singh *et al.*, 2014; Jamnapara *et al.*, 2014; Sree *et al.*, 2014; Purushothaman *et al.*, 2015; Paul *et al.*, 2018; Feng *et al.*, 2018; Wulf *et al.*, 2018; Zala *et al.*, 2019; Zhu *et al.*, 2020) and a highly dense compact coating with complete coverage conforming to electrical insulation requirements in harsh LM environment of interest.

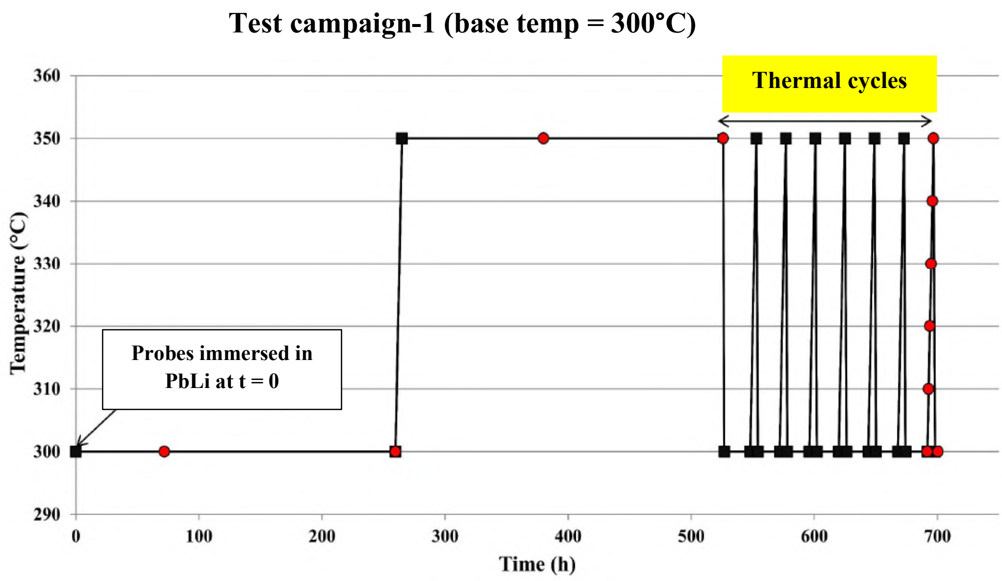

Fig. 4.4 Temperature and time duration details for test campaign-1.

After continuous exposure of over 520 h in PbLi, thermal cycling within PbLi environment was conducted to establish the insulation integrity during possible temperature gradients in an operating LM circuit. Considering the normal operational temperature of PbLi circulations facilities, 300°C was taken as the base temperature for test campaign-1, while IR at the start of last thermal cycle was taken as the base IR value. To gain higher accuracy in measurements, a digital IR tester (Make: Fluke, Model: 1550C) with ±5% uncertainty was used. Measured IR values are reported under Table 4.3 and IR derating trends are shown in Figure 4.5. In addition to the temperature effect, the observed IR derating trends also include the effect of rising PbLi level surrounding the coated probes. However, for the current set up, overall PbLi level rise per 10°C change is estimated less than 1 mm. In consideration to the chemical stability of Al_2O_3, temperature is assumed to be the prominent derating factor for a conservative estimation of IR derating. The above assumption is also supported by the rising trend of IR values towards the base IR value, as mentioned in the last row of Table 4.3, taken just after achieving 300°C at the surface of tank, corroborating thermal and chemical stability of Al_2O_3 insulation in high temperature PbLi environment.

Table 4.2 IR measurements for P1 and P2 in PbLi environment during test campaign-1.

Time (h) (since t=0)	**Temperature (°C)**	**DC test voltage (V)**	**IR for Probe P1 (x 10^9 Ω)**	**IR for Probe P2 (x 10^8 Ω)**
72	300	100	> 6	> 1
260	300	100	> 6	> 3
380	350	100	> 1	> 1
525	350	100	> 1	> 0.9

Table 4.3 Temperature derating factors for IR during last thermal cycle of test campaign-1.

Temperature (°C)	**DC test voltage (V)**	**IR for Probe P1 (x 10^9 Ω)**	**Temperature derating for P1**	**IR for Probe P2 (x 10^8 Ω)**	**Temperature derating for P2**
300 (base)	275	6.18	1.00	3.15	1.00
310	275	3.75	0.61	2.09	0.66
320	275	2.42	0.39	1.60	0.51
330	275	1.73	0.28	1.35	0.43
340	275	1.20	0.19	1.08	0.34
350	275	0.822	0.13	0.835	0.27
300	275	6.08	0.98	2.39	0.76

The observed decrease in the IR value while returning to the base temperature of 300°C could be explained considering the phenomenon of dielectric relaxation in the absence of an external electric field, where the dipoles within the dielectric tend to arrange themselves in a random orientation. However, in presence of an external electric field, the dipoles preferentially realign within the bulk so as to reduce the effect of this external field making the effective electric field within the dielectric to zero. An increase in the temperature results in an agitated state of dipoles and a sudden drop in the temperature may not bring them instantly to the same low energy state leading to a delay in effective dielectric polarization (dipole alignment). Existence of a non-zero dielectric absorption current leads to measurement of a reduced IR (Megger guide, 2006). It should be noted that these derating factors have been estimated post exposure of the insulation coating to high temperature corrosive PbLi environment for over 690 h. In view of similarity of the fabricated probes with electrical cables, observed temperature based IR derating is much better (Megger guide, 2006).

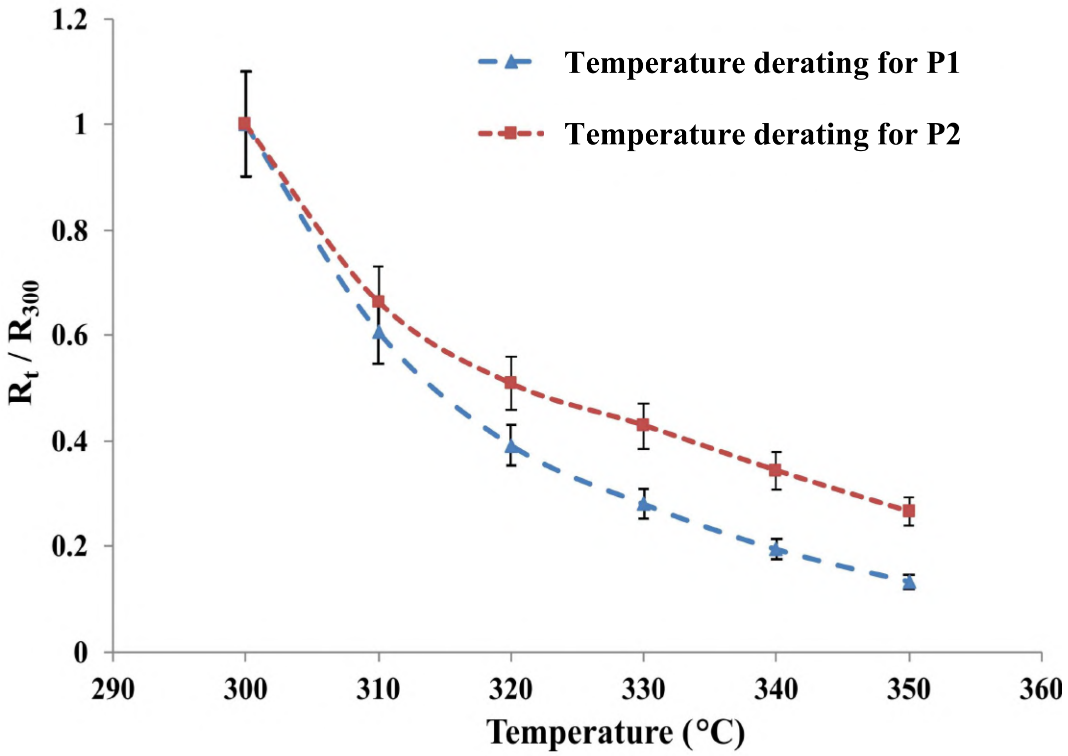

Fig. 4.5 Temperature related IR derating trends for P1 and P2 (post exposure to static PbLi for ~690 h).

Figure 4.6 presents the images of P1 and P2 after removal and post chemical cleaning, depicting only partial cleaning achieved even after sufficient immersion time in a 1:1:1 (volume ratio) solution of acetic acid, hydrogen-peroxide and ethyl alcohol. Such a change in appearance was not observed during an earlier short duration experimental study, where complete cleaning could be achieved for one of the sample probes exposed to PbLi at 300ºC for continuous 250 h. Observed discoloration in present case could be attributed to a partial ingress of PbLi in the coated layer over longer exposure durations. After chemical cleaning, no weight loss was observed for P1 while a normalized weight loss of ~ 1.56 mg/cm^2 over the coated surface area was observed for P2. This loss could be primarily accounted for dehydration of topmost untreated coat layer of P2 during facility heating and could also include partial thinning of the coating section immersed in PbLi. However, in view of no variation in the order of magnitude for IR within uncertainty limits at relevant temperatures (refer Table 4.2 and Table 4.3), dehydration of the coating could be ascribed as the prominent cause for this observed weight loss.

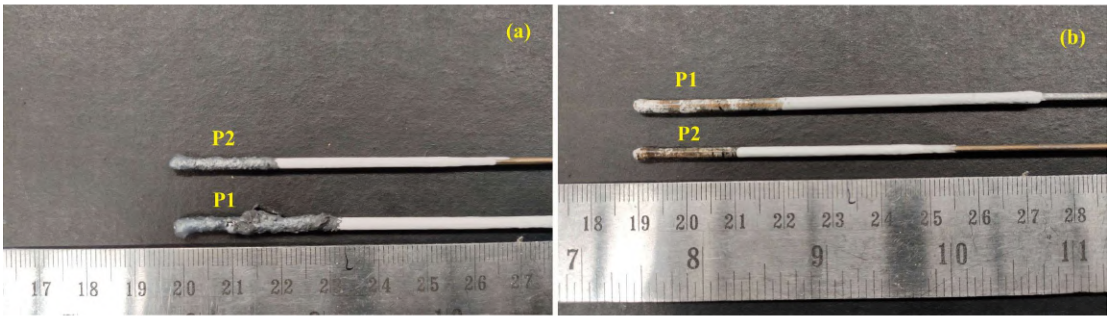

Fig. 4.6 Condition of P1 and P2 after: (a) continuous PbLi exposure of over 700 h; (b) after chemical cleaning.

4.3.2.2 Test campaign-2

Electrical insulation performance achieved for probe P2 (during test campaign-1) through gradual heat curing of uppermost layer during system operation seems promising to achieve coating on substrates with sharp bends, multiple/parallel internal flow sections, complex geometries etc. To establish the repeatability and reliability of this coating technique, a more rigorous test campaign-2 was conducted using probe P3 as per the details shown in Figure 4.7, while the measured IR values with time and temperature are reported under Table 4.4. The variation in IR followed a pattern similar to that observed during test campaign-1, accounting for gradual heat curing of the untreated coat layer.

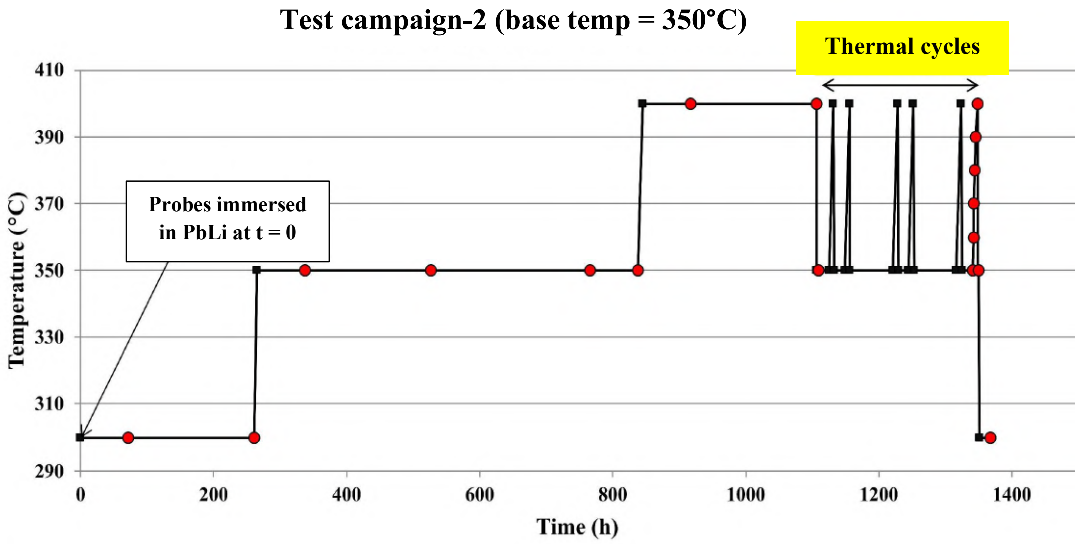

Fig. 4.7 Temperature and time duration details for test campaign-2.

After continuous high temperature PbLi exposure of over 1340 h, temperature based derating factors were estimated using a base temperature of 350°C as reported under Table 4.5 and Figure 4.8. For insulation health estimations and to address the dielectric relaxation observations made during test campaign-1, IR readings were taken at 60 s and 120 s after application of high voltage for all the cases studied towards derating estimations. As observed from Table 4.5, at any given temperature, a rising value of IR from 60 s to 120 s substantiates the health of insulation. A comparison of the data from Table 4.4 and Table 4.5, alongwith consideration to the fact that capacitive charging current normally decays within 30 seconds and conduction current remains constant through the IR test, signifies that dielectric polarization is taking more time which is also indicative of insulation health (Megger guide, 2006). This further corroborates the prominent effect of delayed dielectric polarization as discussed under Section 4.3.2.1. However, as the order of magnitude for IR readings at 60 s and 120 s remains the same, this effect is not of any significant implication for practical purposes toward achieving an electrical insulation in PbLi LM environment.

Table 4.4 IR measurements for P3 in PbLi environment during test campaign-2.

Time (h) (since t=0)	**Temperature (°C)**	**DC test voltage (V)**	**IR for Probe P3 (x 10^8 Ω)**
72	300	275	2.90
261	300	275	4.57
338	350	275	1.30
526	350	275	2.18
766	350	275	2.99
838	350	275	2.89
917	400	275	0.583
1106	400	275	0.767
1109	350	275	2.99

Table 4.5 Temperature derating factors for IR during last thermal cycle of test campaign-2.

Temperature (°C)	**DC test voltage (V)**	**IR for P3 after 60 s (x 10^8 Ω)**	**Temperature derating for P3 (as per 60 s data)**	**IR for P3 after 120 s (x 10^8 Ω)**	**Temperature derating for P3 (as per 120 s data)**
350 (base)	275	0.945	1.00	1.29	1.00
360	275	1.06	1.12	1.39	1.08
370	275	1.26	1.33	1.22	0.95
380	275	0.804	0.85	0.98	0.76
390	275	0.735	0.78	0.821	0.64
400	275	0.638	0.68	0.768	0.60
350	275	2.28	2.41	2.37	1.84

Figure 4.8 also affirms that temperature deratings estimated using IR data at 120 s are higher than corresponding deratings using IR data at 60 s. However, degradation in the IR over a temperature gradient of 50ºC is relatively low compared to both the cases under test campaign-1. Also, the IR value essentially did not deteriorate between 350°C-370°C in contrast to the pattern observed under test campaign-1. These improvements could all be ascribed to a long duration exposure near the required curing temperature of 427°C. The IR after cool down to the base temperature was observed ~ 83% higher than the corresponding value at start of the cycle, which is assumed to be the result of an effective dielectric polarization due to repetitive IR

tests at high voltage leading to a polarization current component to zero. This assumption is also in coherence to the nearly identical IR values observed at 60 s and 120 s after a few IR measurements (refer Table 4.5). However, this needs to be investigated in more detail with similar more tests.

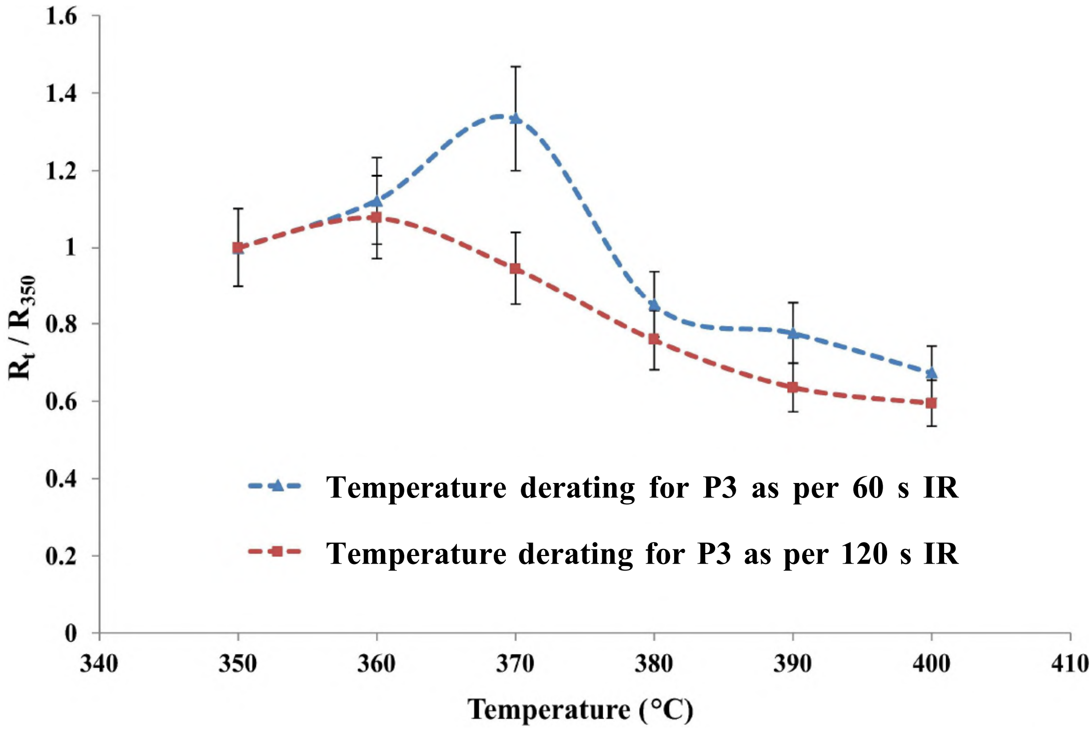

Fig. 4.8 Temperature related IR derating trend for P3 (post exposure to static PbLi for ~1340 h).

The IR at base temperature of 350ºC measured at the end of last thermal cycle (1350 h of exposure) tends towards the measured IR observed at same temperature between 500 h - 800 h of exposure. Similarly, the measured IR values at 300°C (1367 h of PbLi exposure) were $1.89 \times 10^8\ \Omega$ and $3.32 \times 10^8\ \Omega$ after 60 s and 120 s, respectively. All these observations corroborate high integrity and healthiness of the electrical insulation over complete test duration.

Image of the probe after removal from the tank and after chemical cleaning is shown in Figure 4.9. The PbLi exposed coated section appeared blackish after cleaning, which is in close agreement to the findings reported in (Borgstedt *et al.*, 1994). Figure 4.9 shows major visible cracks just after completion of chemical cleaning. Spontaneous chipping of a few coat sections was noticed during chemical cleaning followed by detachment of almost complete PbLi exposed portion of the coating during subsequent drying at RT. Therefore, weight measurements for P3 post exposure could not be performed. A similar observation with an AlN-BN sample immersed in Li was reported (Mitsuyama *et al.*, 1998), where Li covered surface broke into pieces during subsequent cleaning in water, accounted for induced stresses due to reaction between water and Li. However, in the present study, Li activity is negligible owing to the low weight percentage of Li (0.62% to 0.68%). Additionally, neither such observations have been reported for alumina coated samples in previous corrosion studies with PbLi nor observed during test campign-1 for probe P2, which had a similar fabrication method and PbLi immersion process as that of P3. The possibility of crack generation/initiation during thermal cycling cannot be completely ruled out owing to significantly large difference in CTEs. However, the unexposed top-section of coated probe (~20 mm), which is also expected to experience similar thermal gradients, remained well adhered to the substrate with no presence of cracks or indication of brittleness. A crack generation within LM would have led to a sharp decline in the measured IR, which was not observed. Therefore, in view of the IR integrity observed from Table 4.4 and Table 4.5, it is inferred that the through-crack generation occurred post removal of the probe from LM.

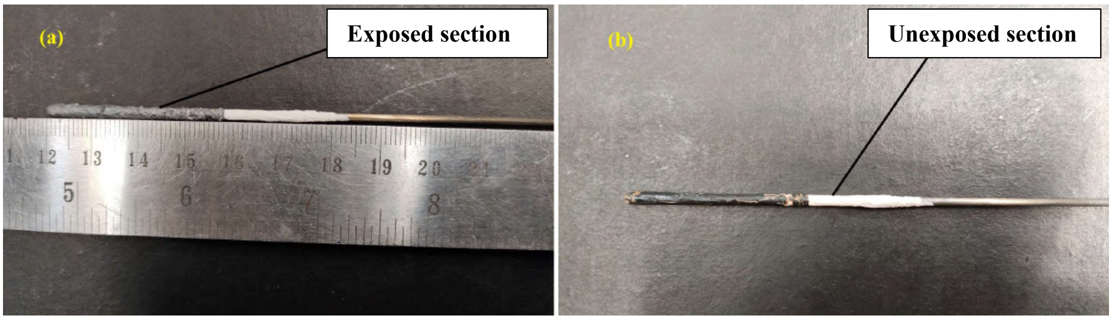

Fig. 4.9 Condition of probe after: (a) continuous PbLi exposure of over 1360 h; (b) after chemical cleaning.

One of the possibilities could be the cracking due to compressive stresses generated over LM exposed portion of coated substrate because of temperature dependent volumetric contraction of the surface adhered PbLi during cool down period. Considering the fact that Al_2O_3 contains predominant ionic bonding (Siegel *et al.*, 2002), the slip planes are essentially non-existent. This type of arrangement does not allow movement of one row of atoms over another, under the influence of an external stress, due to large repulsive forces. Therefore, it is likely that the generated compressive stresses could not be relieved through a re-arrangement of the atoms within the crystal structure, leading to a fracture of the coat. However, the solidified surface adhered PbLi layer held the coat together until it was removed through chemical cleaning procedure, after which the pieces of the coating seem to spontaneously chip-off from the substrate. Under present experimental constraints, such compressive stresses are inevitable. In contrast, during the flowing PbLi conditions in a coolant/breeder system of a fusion reactor, LM will be surrounded by ceramic insulating coatings, leading to an absence of such compressive stresses. However, as the coating cracks were not observed during test campaign-1, the contribution of PbLi exposure duration and temperature is of interest for further compatibility studies. In view of similarity of the fabricated probes to electrical cables, volumetric electrical resistivity was estimated for the enveloping cases using IR relation for an electrical cable. It should be noted that in the present experimental study, a conservative estimation of volumetric electrical resistivity has been performed by assuming the tip-portion (blob) as a perfect electrical insulation in view of its relative higher thickness as compared to the coating thickness along the length. Therefore, complete insulation leakage current is assumed to flow only through thickness of coating along the probe length, leading to an under estimation of calculated volumetric electrical resistivity for the probe(s) under reported operating conditions. Calculated volumetric electrical resistivity remained of the order of 10^9 – 10^{11} **Ω**-cm between 300°C-400°C. The coating resistance, measured as a product of volumetric electrical resistivity and insulation thickness, remained of the order of 10^4 – 10^6 **Ω**-m^2, many orders of magnitude higher than required for successful operation of LM based coolant circuits with acceptable MHD pressure drops (Buhler and Molokov, 1993; Malang *et al.*, 1995; González *et al.*, 2020). Calculations for volumetric electrical resistivity and coating resistance are provided under **Appendix-A**. This further substantiates the applicability of Al_2O_3 coatings as an electrical insulator for high temperature PbLi coolant/breeder circuits in fusion power plants. It can be observed that the volumetric electrical resistivity for fully treated probe P1 is one order of magnitude higher than that of P2 at same temperature, an effect that can be attributed to higher degree of compaction achieved with full heat curing. However, sufficient volumetric electrical resistivity achieved and ease of coat formations using gradual heat curing through system operations makes the second method more promising and attractive.

4.3.3 Metallographic Investigations

Dip coating technique usually results in an uneven coating thickness across the length. Additionally, heat cure of the coated probes in a horizontal orientation, as mentioned under Section 4.2, may also contribute to the coating thickness variations under the influence of gravity. In this view, cross-sectional samples were cut across PbLi exposed portions of probes P1 and P2, using a diamond wire cutter, to examine coating thicknesses and PbLi ingress depth. A representative SEM image for one of the cross-sectional samples from P1, as shown in Figure 4.10, confirms a compact coating free from cracks (cracks appearing on the surface of cross-sections are due to wire cutting process).

For a given probe, coating thicknesses were measured at various points of the cut samples and an average coating thickness value was calculated by taking an average of all the thickness measurements performed. For illustration purposes, coating thickness estimations on one of the samples cut from probe P2 are depicted in Figure 4.11. Estimations as per the method described above resulted in average coating thicknesses of ~495 μm and ~212 μm for PbLi immersed portions of probe P1 and P2, respectively.

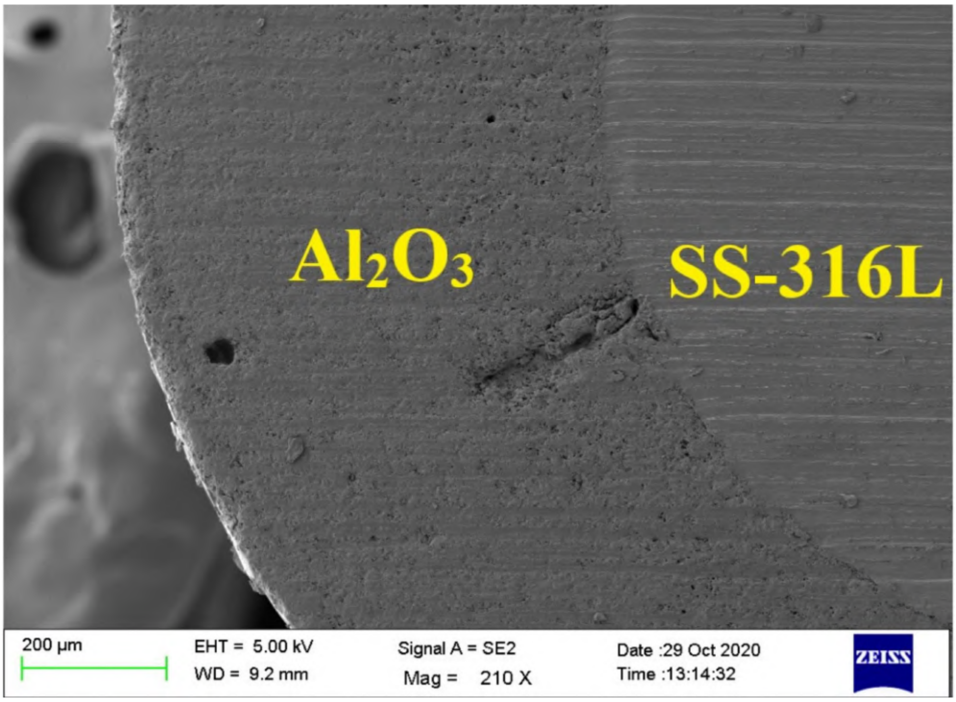

Fig. 4.10 Cross-sectional view of a sample from P1 showing Al_2O_3 coating layer deposited and well adhered to substrate.

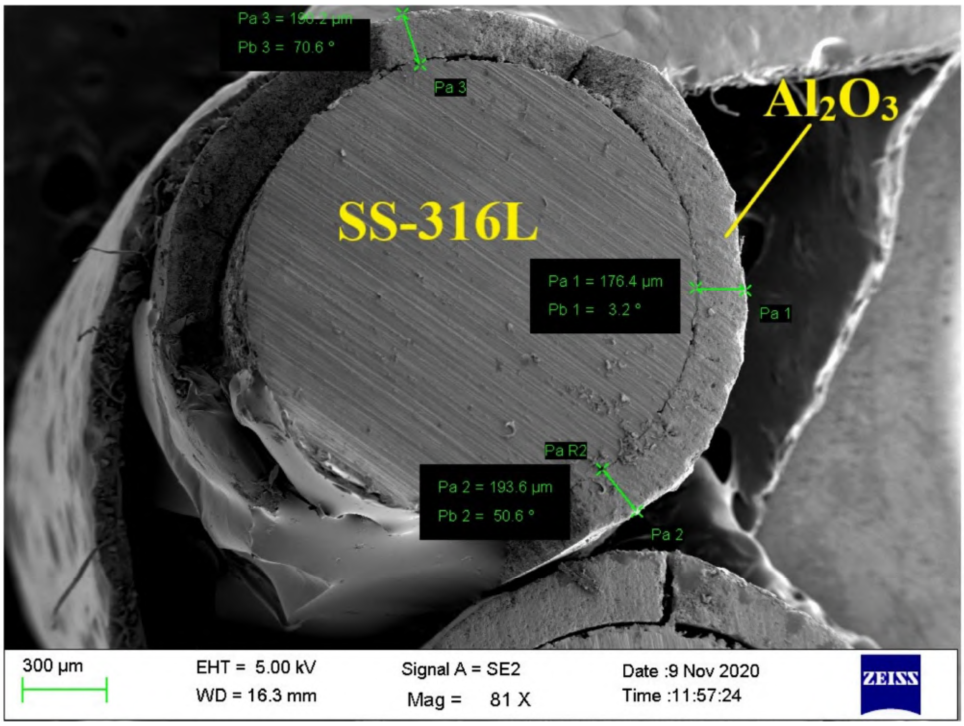

Fig. 4.11 Cross-sectional view of a sample from P2 for estimation of average coating thickness.

To estimate PbLi ingress depth, EDX point analysis was carried out at different locations across the cross-sections. Points indicated in Figure 4.12(a) and Figure 4.12(b), moving radially inwards towards the substrate, were chosen for point EDX analysis of probes P1 and P2, as detailed in Table 4.6 (point P_1 lying at the surface of the coating exposed to PbLi). The points of analyses for P1 and P2 were ~20 µm apart and ~10 µm apart, respectively. In view of the primary objective of validating electrical insulating coating towards application in PbLi eutectic alloy, ingress depth of Pb (~99.32 - 99.38% by weight in PbLi eutectic) was considered representative in consistency with previously reported coating qualification studies with respect to corrosion compatibility assessments (Jain et al., 2014; Jamnapara et al., 2014; Gazquez et al., 2017; Paul et al., 2018; Wulf et al., 2018).

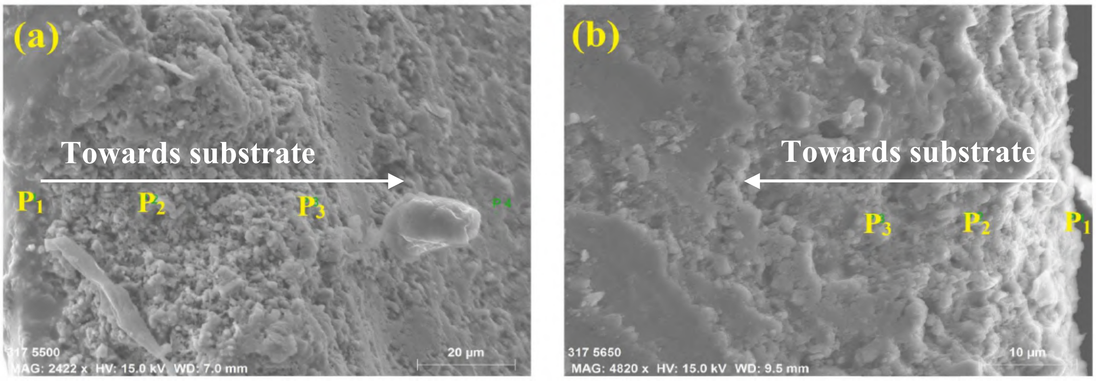

Fig. 4.12 EDX point analysis for Pb ingress estimations for: (a) probe P1; (b) probe P2.

Analyses at various points corroborate Pb ingress limited to 20 µm depth for both the probes tested under test campaign-1. Corresponding EDX elemental analysis are represented under Figure 4.13(a)-(c) and Figure 4.14(a)-(c) for probes P1 and P2, respectively. The limited penetration depth of Pb validates Al_2O_3 coating as an electrical insulator as well as corrosion barrier for high temperature PbLi applications.

Restricted ingress depth also substantiates the assumption of temperature being the prominent factor in IR derating, as discussed under Section 4.3.2.1.

Table 4.6 Ingress profile of Pb for probes P1 and P2.

Probe Identification	**Point number (marked in yellow)**	**Pb % as per EDX analysis**
Probe P1	P_1 (at surface)	13.08
	P_2 (~20 µm from P_1)	0.00
	P_3 (~40 µm from P_1)	0.00
Probe P2	P_1 (at surface)	2.92
	P_2 (~10 µm from P_1)	0.69
	P_3 (~20 µm from P_1)	0.00

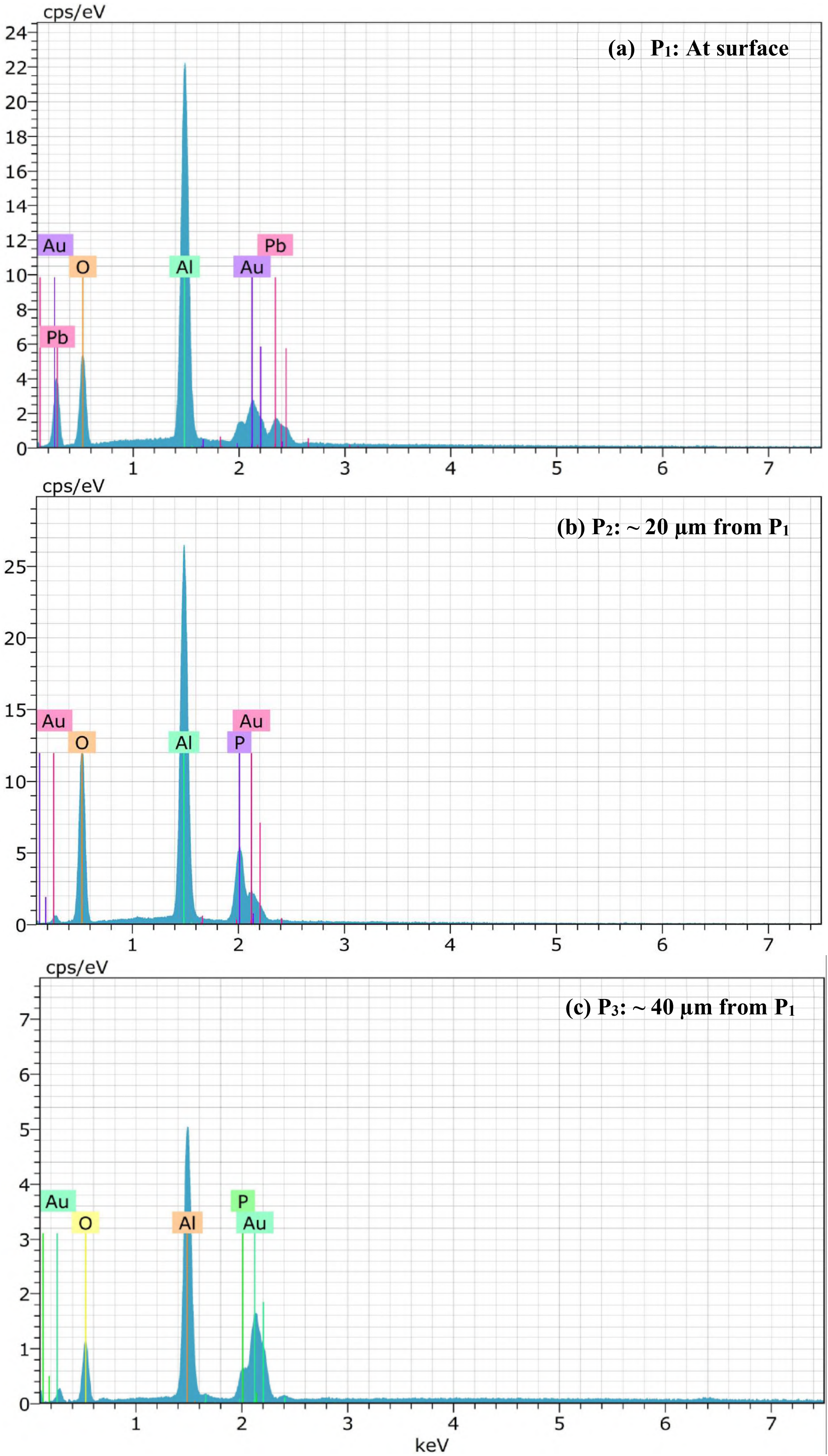

Fig. 4.13 EDX elemental analysis for probe P1.

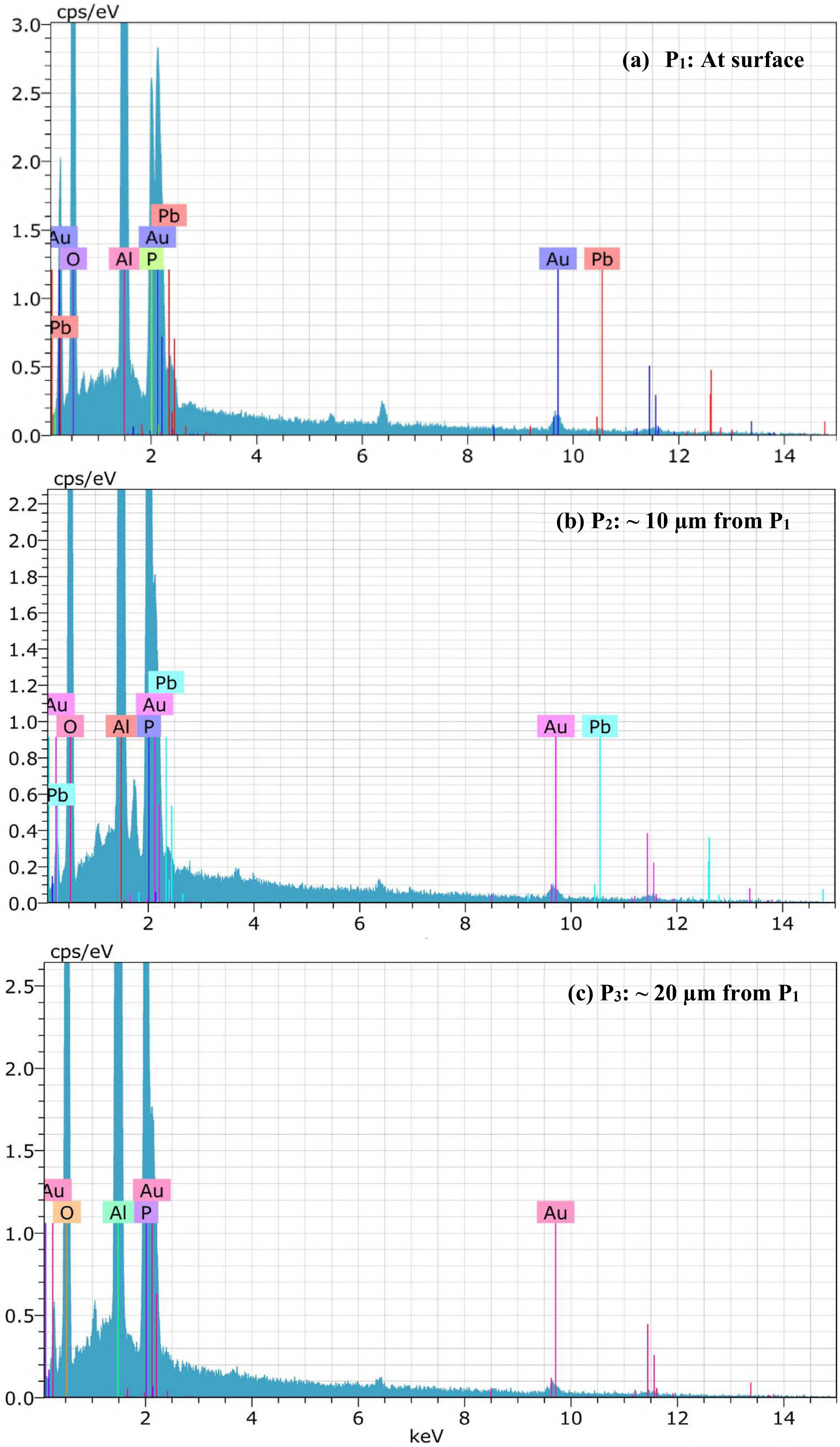

Fig. 4.14 EDX elemental analysis for probe P2.

As shown in Figure 4.15(a), the coating thickness for P3, estimated from the chipped off coat sections and averaged over 04 data points, was ~429 μm. A representative image for one of the samples with observed cracks across the thickness is shown in Figure 4.15(b). PbLi ingress depth estimations for P3, using EDX, were rendered inconclusive as Pb ingress was detected over the complete coating thickness in stark contrast to the observed IR reported under Table 4.4 and Table 4.5. This can be explained in view of observed major cracks after chemical cleaning (refer Figure 4.9 and Figure 4.15(b)), which seemed to have allowed ingress of Pb from the cleaning solution itself across the complete coating thickness. All the analysed samples from P3 indicated similar results.

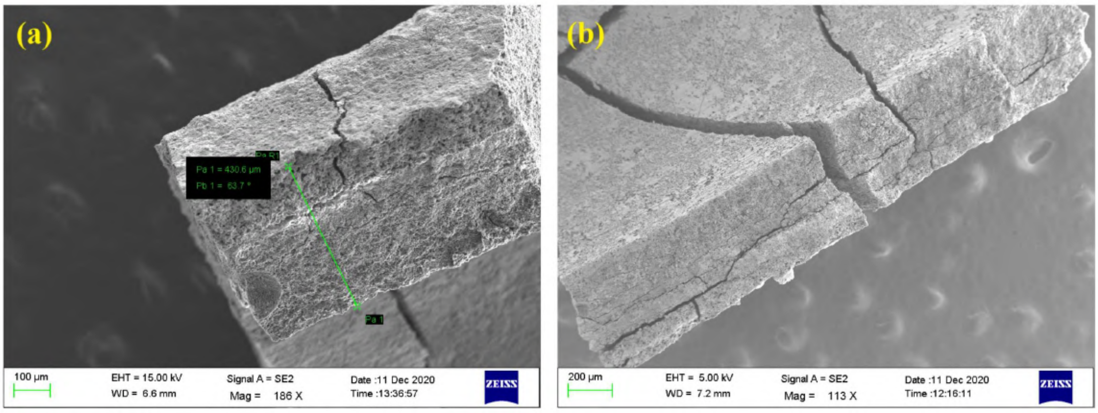

Fig. 4.15 SEM analysis for Probe P3: (a) coating thickness estimations; (b) cracks across the coating thickness.

Surface microstructure of PbLi exposed coating portion for P1 is presented in Figure 4.16(a), suggesting presence of flaked/whisker type structures (marked as A) and agglomerates less than 1 μm in size (marked as B) mostly covered at the surface with flakes/whiskers. The typical flake/whisker type pattern is in close agreement to the reporting of α-Al_2O_3 (Santos *et al.*, 2000; Patel *et al.*, 2020) while the globular pattern is generally associated with θ-phase of Al_2O_3 (Santos *et al.*, 2000). X-Ray Diffraction (XRD) analysis of the sample, as shown in Figure 4.16(b), depicts the presence of only α-phase of Al_2O_3 (ICDD card no: 02-002-1227). Prominent presence of α-phase is attributed to the calcined Al_2O_3 powder utilized as a raw ingredient for coating suspension, as verified through separate XRD analysis of dried coating suspension sample.

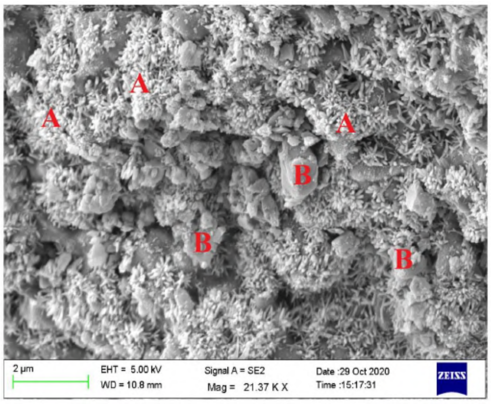

(a)

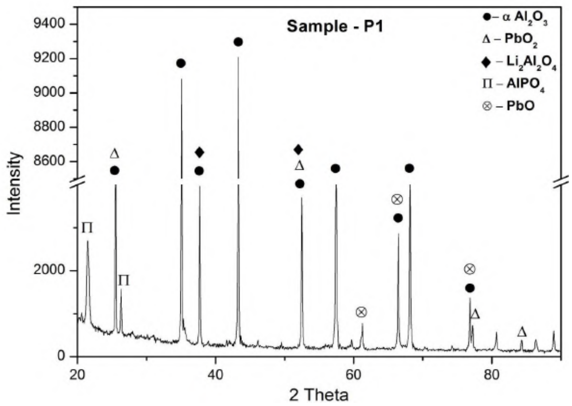

(b)

Fig. 4.16 (a) Surface morphology of PbLi exposed Al_2O_3 section for P1; (b) XRD pattern.

As reported under various studies, α-Al_2O_3 is the thermodynamically stable phase formed through irreversible phase transformations from other transition alumina when heated at temperature in excess of 1000ºC, resulting in the crystal shapes varying with the nature of precursor (Santos *et al.*, 2000). Therefore, the α-Al_2O_3 agglomerates seem to have been converted from θ-Al_2O_3 particles during the calcination of raw powder used for suspension preparation. Aluminium monophosphate ($AlPO_4$) detected in the XRD (ICDD card no: 00-048-0652) is the binding agent of the utilized coating while the presence of lead-oxides (PbO, PbO_2) is primarily accounted for oxidation of Pb content adhered to the probe coated surface and pre-existing oxides in the used PbLi melt. Formation of $LiAlO_2$ (ICDD card no: 00-001-1306), instead of generally observed Li_2O for PbLi melt systems, is in agreement to the previously reported compatibility studies between Al_2O_3 and PbLi (Pint and More, 2008; Jain *et al.*, 2014; Jamnapara *et al.*, 2014). Previous investigations affirm that Li reacts with trace amount of oxygen present in the argon gas to produce Li_2O, which further reacts with Al_2O_3 over time to form $LiAlO_2$.

$$4Li + O_2 \text{ (trace amount from Ar)} \rightarrow 2Li_2O(s)$$

$$Li_2O(s) + Al_2O_3(s) \rightarrow 2LiAlO_2(s).$$

Regular filling/purging of argon cover gas to maintain an inert atmosphere over LM acts as a constant supply source for oxygen in the present experimental study. The particle morphology of the PbLi exposed section and the corresponding XRD analysis for P3, as shown in Figure 4.17(a) and Figure 4.17(b) respectively, also confirm the presence of α-Al_2O_3 with nearly spherical and uniform particle size < 100 nm.

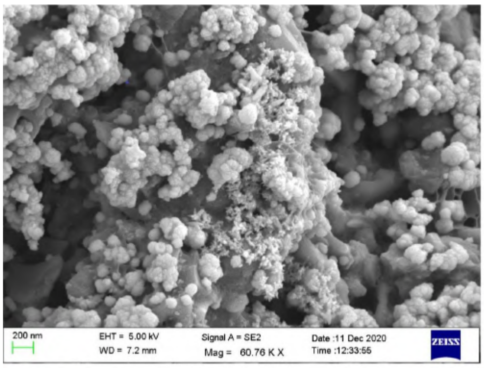

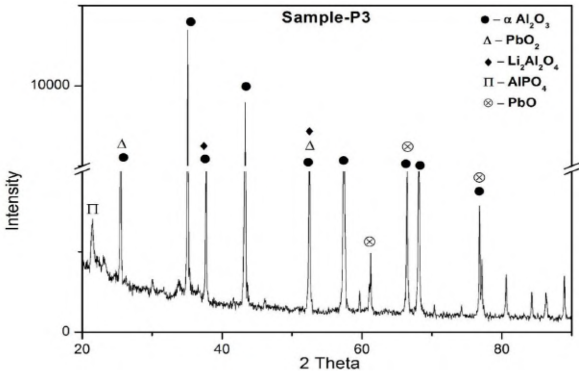

(a) (b)

Fig. 4.17 (a) Particle morphology of PbLi exposed Al_2O_3 section for P3; (b) XRD pattern.

An important establishment from the XRD results of all the tested probes is the prominent presence of α-Al_2O_3 and $AlPO_4$, both of which are promising candidates for TPB with high permeation reduction factors and exhibit high mechanical and chemical stability at relevant operating temperatures (Chen *et al.*, 2003; Levchuk *et al.*, 2004; Zhang and Hatano, 2010; Jun *et al.*, 2016; Wang *et al.*, 2019). This observation paves the way towards exhaustive qualification of the studied coating technique for nuclear fusion applications.

4.4 CONCLUSION

The major conclusions derived from the second experimental study are mentioned below:

- The explored alumina coating seems chemically compatible and thermally stable towards usage as an electrical insulation in corrosive liquid PbLi environment upto 400°C.
- The coating application method does not require exposure of substrate material to high temperature and provides a well-adhered, compact and non-porous coat on SS-316L substrates.
- The observed volumetric electrical resistivity of the order of $10^9 – 10^{11}$ Ω-cm is sufficient for realization of the electrical conductivity based two-phase detection probe for PbLi LM applications. The observed coating resistance of the order 10^4-10^6 Ω-m^2 justifies the utilization as a feasible solution to MHD pressure drop mitigation in LM breeder/coolant circuits.
- The prominent presence of thermodynamically stable phase α-Al_2O_3 along with $AlPO_4$ makes the coating a potential candidate for TPB in future fusion reactors.
- Considering activation of aluminium in a nuclear environment, further optimization and automation is required in the coating application process to achieve thinner coatings with uniform thicknesses.

4.5 CLOSURE

An aluminium monophosphate bonded high purity Al_2O_3 coating suspension applied using dip coating/brush coating technique was studied as a candidate functional material towards electrical insulation requirements in PbLi LM applications. Coated substrates were validated in static PbLi for continuous 1360 h in the temperature range of 300ºC-400ºC for assessment of electrical insulation integrity and temperature derating. For its ease of application, the adopted coating method seems compatible for coating of difficult substrate geometries like manifolds and complex structures typical of breeder blankets. High brittleness observed after chemical cleaning of PbLi exposed coated section is of interest towards further studies. Homogeneity of the coating application method was established for different substrate materials and geometries including internals of pipe-sections.

Considering the initial coating applications in lab scale PbLi R&D facilities, the preliminary investigations were conducted for a moderate temperature range between 300°C - 400°C only. However, further investigations are planned for extended durations at higher temperature upto 500°C with flowing PbLi. A complete corroboration towards application suitability requires further rigorous validations under flowing PbLi conditions at representative temperature and radiation environment to assess extent of radiation induced conductivity. Further plans also include process optimization to achieve a uniform and repeatable coating thickness by integrating industrial practices like dip-coater and atomizers.

In conclusion, the electrical insulation performance of the coating is accessed sufficient towards realization of prototype two-phase detection probe for PbLi environment. The next chapter presents details about fabrication of the probe and its validation in PbLi-Ar vertical columns.

CHAPTER 5

DEVELOPMENT AND VALIDATION OF A TWO-PHASE DETECTION MULTIVARIABLE PROBE FOR LEAD-LITHIUM/ARGON VERTICAL COLUMNS

5.1 INTRODUCTION

Nuclear fusion breeder blanket concepts employ various attractive solid and liquid candidate breeder materials in the form of lithium/lithium-containing compounds like Li, Pb-16Li, Li_2O, $LiAlO_2$, Li_4SiO_4, Li_2SiO_3, Li_2TiO_3 and Li_2ZrO_3 (Malang *et al.*, 1995; Tang *et al.*, 2009) with the primary objectives of efficient heat extraction and tritium breeding to achieve self-sufficiency. Out of these candidate materials, PbLi has gained immense focus for its various advantages including a high TBR without the need for an additional neutron multiplier as required for solid breeders, ability to circulate and therefore extract tritium outside the blanket, immunity towards radiation damage and thermal stresses, high thermal conductivity and less chemical activity compared to pure Li (Malang *et al.*, 1995). Success of a breeder concept is primarily governed by the TBR and heat extraction performance, which can be well achieved using PbLi in a self-cooled concept. However, as reported under various studies, interaction of Li with fusion neutrons to breed tritium also leads to formation of helium gas, a by-product, which has relatively low solubility in PbLi and could precipitate in the form of bubbles affecting the system design and safety (Sedano, 2007; Kordac and Kosek, 2017; Fraile and Polcar, 2020).

*This chapter is published in **Saraswat, A.**, **A. Prajapati**, **R. Bhattacharyay**, **P. Chaudhuri and S. Gedupudi** (2022) Development of a compact multivariable sensor probe for two-phase detection in high temperature PbLi-argon vertical columns. *Instruments and Experimental Techniques*, **65**(1), 179-189.

Entrapped gases within breeder/coolant LM circuit tend to cause local hot spots, improper shielding and a reduction in TBR. As reported under (Kordac and Kosek, 2017), for PbLi flow rates upto 1000 kg/s, this gas phase generation is significant and independent of pressure. Various concepts like HCLL, WCLL, DCLL and LLCB, therefore, would be prone to such a phenomenon. In some of the concepts like HCLL and LLCB, accidents like an in-box TBM LOCA and LOHS will lead to ingress of high pressure helium gas inside PbLi coolant circuit resulting in a liquid-gas two-phase flow with high density ratio between the two phases. Additionally, preliminary lab scale experimental runs at IPR with water as a test fluid and water flow channel configurations similar to LLCB TBM has corroborated presence of trapped gas pockets at sharp 90° bends inside TBM-like geometry and entrained gas bubbles in re-circulation zones. In a similar phenomenon, the two-phase flow and trapped gas pockets are expected in lab scale PbLi R&D facilities due to charging in presence of an inert cover gas.

For modelling such occurrences of high relevance towards design and operational safety of ancillary breeder/coolant circuits of fusion reactors, an extensive experimental database needs to be generated for two-phase flow regimes in high density LMs, mandating development of proper diagnostic tools compatible with high temperature and corrosive PbLi environment. Numerous two-phase flow experimental studies for room temperature LMs and low-melting LMs have been conducted worldwide utilizing available techniques (Saito *et al.*, 2004; Saito *et al.*, 2004; Saito *et al.*, 2005; Gundrum *et al.*, 2016; Keplinger *et al.*, 2017; Xu *et al.*, 2019; Keplinger e*t al.*, 2019). Although commercially available techniques (like PIV, laser etc.) and specialized techniques (like γ-ray, X-ray, NR etc.) provide a non-intrusive way for detection of two-phase (Bertola, 2003; Gardenghi *et al.*, 2020), the opaque nature, extreme operating environments and installation constraints specifically encountered in LM facilities make these techniques less attractive towards practical implementation. Specifically, localized detection of trapped gases within a confined zone mandates miniaturization of the measurement technique/probe. Electrical impedance based measurement techniques provide a better route in consideration to the ease of installation, feasibility of adaptation to specific applications and good response due to a large difference between the electrical conductivities of LM and gas (Nuclear Energy Agency Handbook, 2015). A relevant and detailed two-phase study on Lead-Bismuth Eutectic (LBE) utilizing electrical conductivity probes has been conducted upto a temperature of 200°C with application of epoxy-resin insulation (Ariyoshi, 2015). However, adaptation of the technique to PbLi scenarios puts severe demands on the electrical insulation in terms of chemical compatibility with highly corrosive PbLi at an operating temperature upto 400°C. As per the recent literature (Valls, 2020), no experimental data exist at present relevant to two-phase flow detection with PbLi as one of the constituent phases. Therefore, numerical techniques like RELAP/SCDAPSIM/MOD4.0 codes are being applied to study different flow regimes with PbLi as one of the constituents.

This study primarily aims to bridge the existing gap with development and preliminary validation of a multivariable/hybrid probe, based on the electrical conductivity principle in conjunction with bulk temperature measurements, as a tool to study two-phase flow regimes in PbLi environment. In the present work, detection of gas phase in the form of bubbly flow and estimations of void fraction has been performed for bulk PbLi temperature upto 400°C. Validation of measurement technique for accidental scenarios like in-box TBM LOCA/LOHS is performed with a controlled Ar gas injection at high flow rates varying from 1.5 slpm to 3.5 slpm in a vertical PbLi static column. Scope of the present study, however, does not encompass determination/reconstruction of bubble shape within LM.

5.2 MATERIALS AND METHODS

5.2.1 Probe Design

The hybrid sensor probe is fabricated from a duplex configuration K-type thermocouple with an outer sheath diameter of 1.5 mm and both the sensing junctions located at a distance of 1.5 mm from the tip. Ungrounded hot junction configuration allows utilization of a single probe for simultaneous electrical conductivity based voltage measurements and bulk temperature measurements of two-phase systems. Using a dip coating technique, a thin layer of refractory coating suspension of aluminium monophosphate bonded calcined Al_2O_3 with 99.8% purity is applied on the probe sheath (made of SS-316), which is then inserted into a recrystallized alumina tube of 200 mm length with 2 mm bore and 1 mm wall thickness intended to provide protection and ruggedness to the probe in a heavy LM environment against impacts from Ar bubbles rising in the two-phase column over the complete range of flow regimes. End of the alumina tube (near the sensor tip) is closed by filling the same coating suspension, such that ~1.5 mm of the thermocouple sheath is exposed outside the protection tube. For each coating stage, an air-set period of 24 h at RT was followed by high temperature heat curing steps as discussed under Section 4.2 in Chapter-4.

After the first heat cure, the annular region between the thermocouple sheath and alumina tube wall is filled with alumina slurry, from the rear side, using a hypodermic needle, and then second heat cure is performed. Closure of the rear end of the tube and coating over 100 mm length of the tube outer surface followed by the third heat cure completes the probe fabrication. Schematic diagram of the probe and a relevant section of the final fabricated probe are shown in Figure 5.1(a) and Figure 5.1(b), respectively. For simplicity of representation, only one temperature measuring junction is shown in Figure 5.1(a).

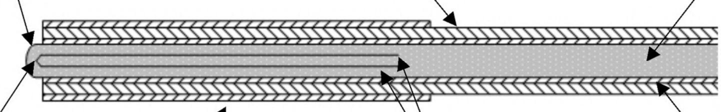

Fig. 5.1(a) Schematic representation of the multivariable probe.

Working principle for the probe is similar to that mentioned in Figure 3.1 of Chapter 3 and also referred in (Nuclear Energy Agency Handbook, 2015; Saraswat *et al.*, 2021) except that the second electrode is replaced by another K-type thermocouple, which is also utilized to measure bulk PbLi temperature in the test facility. Fabricated probe provides thermal trends for the two-phase flow in addition to discrete voltage dips corresponding to bubble interactions with the exposed metallic tip of the sheath. Overall average diameter of the coated section of as-fabricated probe is ~ 4.6 mm.

Room temperature IR for the as-fabricated probe was > 275 GΩ at 275 VDC providing an insulation leakage current < 1 nA, measured using Fluke 1550C digital insulation tester. Installation of the probe is facilitated using compression fittings to provide a gas tight seal for inert cover gas environment and to minimize probe movement during bubble impaction.

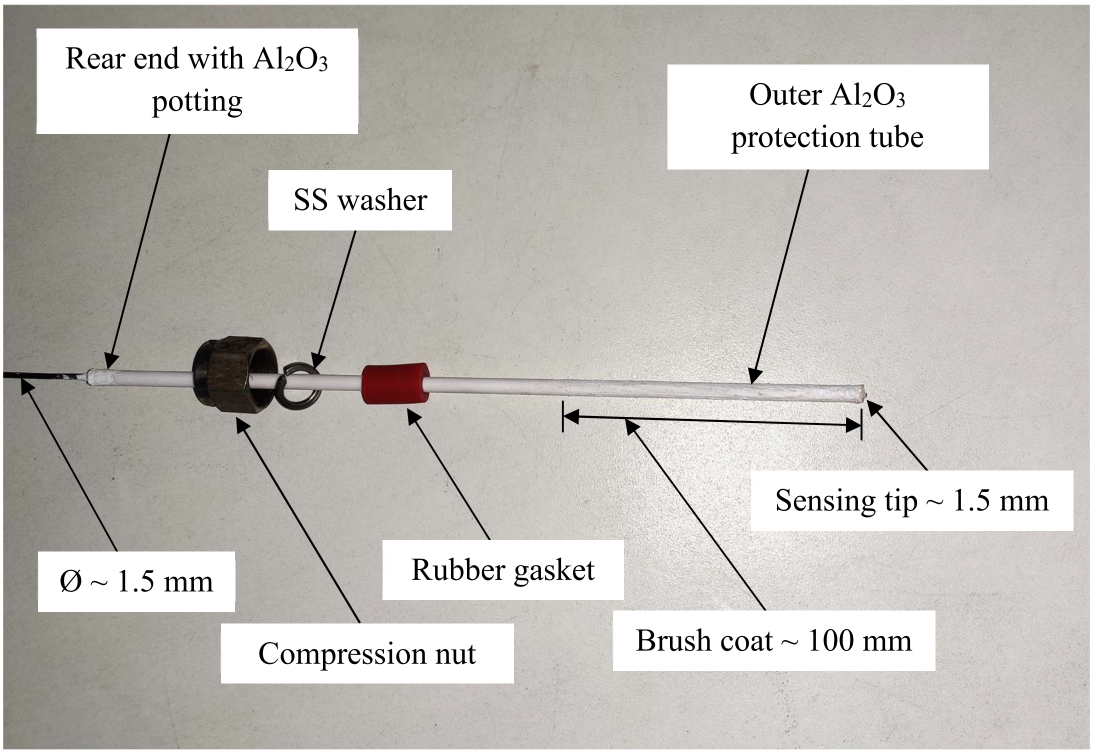

Fig. 5.1(b) As-fabricated multivariable probe for PbLi-Ar two-phase flow detection.

5.2.2 Test Facility: Design And Operation

Figure 5.2(a) represents the schematic of the developed test facility (without PbLi tank) highlighting PbLi wetted components, while the assembled test set up is shown in Figure 5.2(b). To minimize the thermal gradients within bulk PbLi, the inner diameter and height of PbLi tank are kept as 52.48 mm and 100 mm respectively. All the PbLi wetted components are fabricated from SS-304 while the probe sheath is made of SS-316. Resistive heating in a feedback control loop employed at the tank outer surface maintains the bulk PbLi temperature within ±5°C. Melting of PbLi chunks is performed in the tank with a positive Ar pressure environment with vent valve in closed condition. To increase the probability of bubble interaction with the sensing tip of the fabricated probe, injection of Ar is performed using an 8-legged spider configuration gas sparger with three bores of 2 mm in each leg. During continuous injection of Ar through sparger, a momentary closure of the vent valve with simultaneous rise in system pressure (measured using a digital pressure transmitter) ensures the flow of Ar in the test facility.

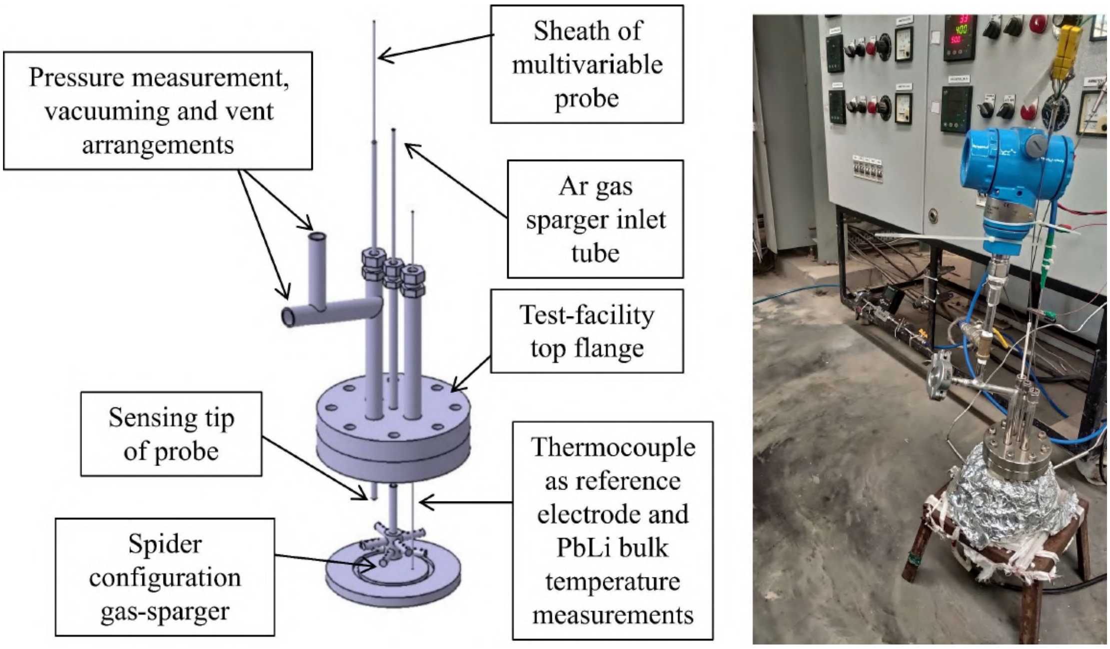

(a) (b)

Fig. 5.2 (a) Schematic representation of PbLi-Ar two-phase test facility; (b) Assembled two-phase flow test set up with installed probe (similar orientation as in Fig. 5.2(a)).

After establishing the gas flow, the sparger is pushed inside static liquid PbLi till the bottom of the tank. The Ar gas injected nearly at RT, flows downward through the complete axial length of the sparger and emerges out in surrounding PbLi environment from the bores giving rise to a two-phase flow regime within PbLi column. The separate bare-sheathed thermocouple, also acting as second electrode of electrical conductivity based circuit, is dipped inside bulk PbLi (with measuring junction just above the tank bottom but below the sparger bores) to measure the bulk PbLi temperature before generation of the two-phase flow and to maintain electrical conductivity with PbLi at all instants. After stabilization of the two-phase flow, the hybrid probe is inserted and the contact with PbLi is ensured using real time voltage measurements from electrical conductivity circuit and simultaneous rise of both the thermocouple signals of the hybrid probe. The vent valve on the top flange is kept fully open during two-phase flow detection experiments. For lower flow rates, variation in the Ar flow rate through the sparger is achieved through modulation of a needle valve downstream of the gas cylinder. For higher flow rates, a Digital Mass Flow Controller (DMFC) is employed to regulate a constant Ar flow to realize high void fractions similar to the accidental conditions of an in-box TBM LOCA/LOHS. The distance between the probe tip and the top layer of sparger legs is ~55 mm.

5.3 RESULTS AND DISCUSSIONS

5.3.1 Probe Calibration And Response Time Estimations

Probe calibration is performed in static liquid PbLi at bulk temperature of 290°C by manual dipping and retrieval giving rise to almost pulsed shaped voltage output, across a 250 Ω sensing resistor, nearly equal to the excitation voltage of 5 VDC due to high electrical conductivity of PbLi (Schulz, 1991; Martelli *et al.*, 2019). To sample the thermocouple signals at high frequency synchronous with voltage signals generated from conductivity circuit, millivolt (mV) outputs of the temperature sensors are logged as raw data, and the offline temperature conversion is performed using a constant Seebeck coefficient of 40 μV/°C for K-type thermocouple in the operating range of interest. Error minimization related to Cold Junction Compensation (CJC) is achieved using a controlled ambient temperature at DAQ side. Utilized DAQ card (PXIe-6363) provides an absolute accuracy of ≤33 μV for the selected mV measurement range providing an error less than ±1°C for K-type thermocouple. Data processing for the temperature trends also involves smoothening using a moving average function of last 100 samples as represented in the thermal trends.

A representative data logged at 0.2 kHz sampling frequency is shown in Figure 5.3. From t = 0 to 5.63 s, the probe outside PbLi shows a zero voltage output due to an open circuit (no current passing through the sensing resistor). As soon as the probe is dipped in PbLi (t = 5.63 s), a pulsed output of 5 V is obtained and a simultaneous sharp positive slope is observed for both the thermocouples leading towards the bulk PbLi temperature of 290°C. It should be noted that the rise in temperature observed between t = 0 to 5.63 s is due to travel of the probe towards PbLi before immersion. At t = 48.45 s, the probe is pulled out of PbLi leading to a zero voltage signal corresponding to a break in continuity and a simultaneous downward trend in both the temperature values is observed. The time duration from t = 48.45 s to 77.68 s simulates a slug flow (a long traversing bubble). The same pattern is repeated for probe insertion in PbLi at t = 77.68 s and retrieval at t = 92.62 s. The similarity in the temperature variation trends for both the junctions of duplex thermocouple validates the accuracy of measurements. Between t = 106.89 s to t = 115.66 s, a number of repeated dip/retrieve cycles with approximately 1s dip time, simulating a bubbly flow, highlight the excellent response of the electrical conductivity based measurements but sluggish response of the temperature signals. However, it could be noticed that the magnitude of the temperature during this time period i.e. ~283°C remains in between the magnitudes when the probe tip was in contact with PbLi (~289°C) and when the probe was in complete gas phase (~276°C).

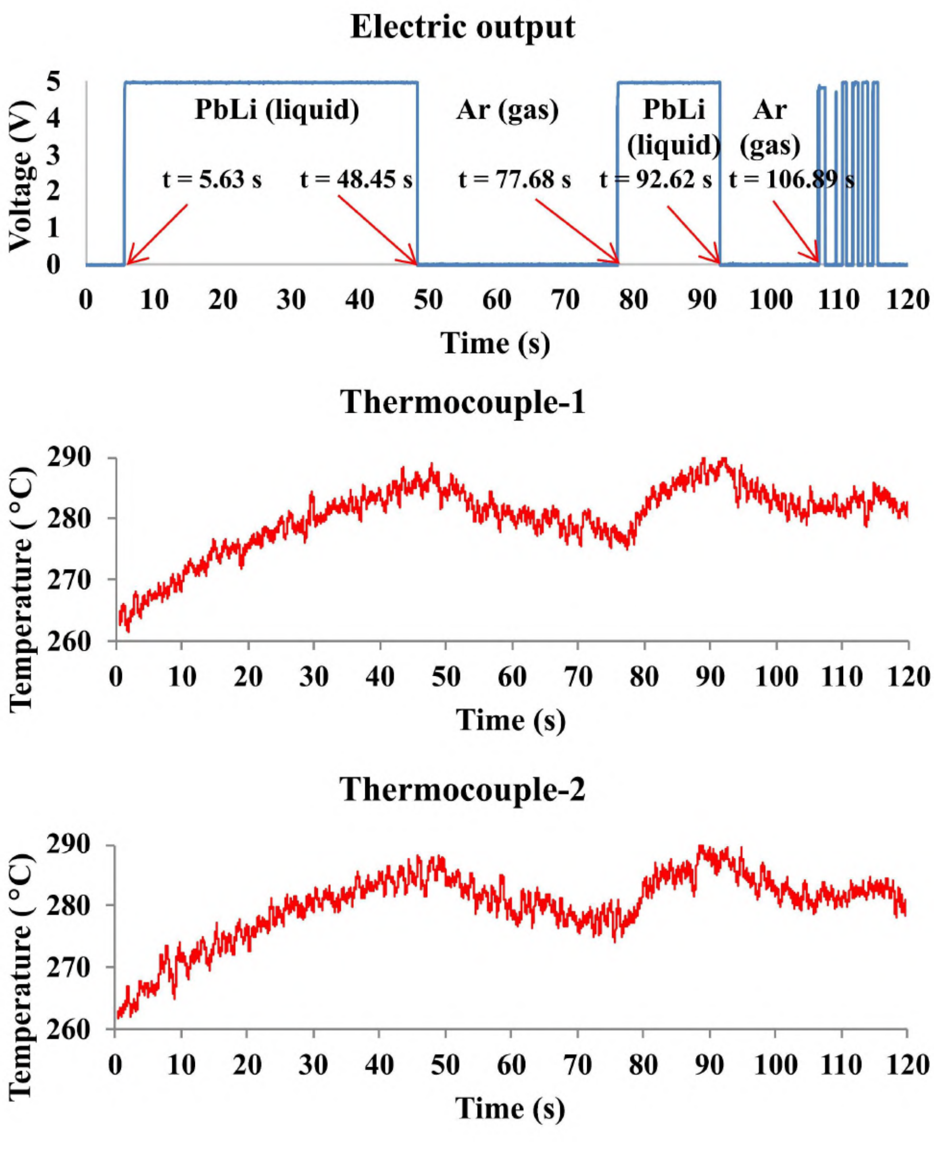

Fig. 5.3 Calibration test of probe in PbLi environment highlighting the effect of PbLi contact on the electrical conductivity based signals and temperature trends.

A detailed data analysis of the interpolated voltage signal from the electrical conductivity scheme for one of the retrieval cycles is shown in Figure 5.4. The marker points with values mentioned in brackets provide actual experimentally logged data, while the interpolated signal establishes that the T_{90} response time of the sensor is ~4.5 ms for dropping voltage (retrieval from PbLi simulating a bubble impaction on probe tip). A finite drop time arises for the voltage signal as the electrical continuity does not break instantly due to a thin film of LM attached to the probe tip (Jalili and Zarrati, 2004). Although, the calibration and response time of the sensor probe also depend on the sampling frequency utilized as demonstrated under Chapter-3 of this thesis (Saraswat *et al.*, 2021) for water-air systems, in view of high electrical conductivity of PbLi, a relatively lower frequency of 0.2 kHz suffices for a conclusive qualitative real time detection of two-phase flow in PbLi columns.

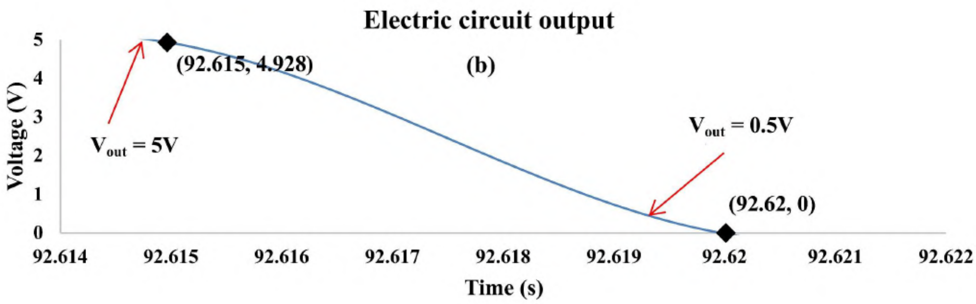

Fig. 5.4 Signal analysis to estimate T_{90} response time during retrieval from PbLi.

Assuming the case of an irregular shaped single Ar bubble with an impaction chord length = $l + d$ as shown in Figure 5.5 (where l = length of conducting tip of the hybrid probe) rising vertically in a PbLi column with a resultant velocity v. As discussed in Chapter-3 and our previous work (Saraswat *et al.*, 2021), voltage dip will initiate at the instant shown below i.e., after complete encapsulation of the conducting tip (AB) by the Ar bubble, and voltage rise will commence as soon as the length d has been traversed across the point B, due to re-established electrical continuity. Taking the limiting case where the time taken to traverse length d exactly equals T_{90} response time for the voltage dip case, the conclusive detection of the bubble based on T_{90} response is given by:

$$d = vT_{90} \tag{5.1}$$

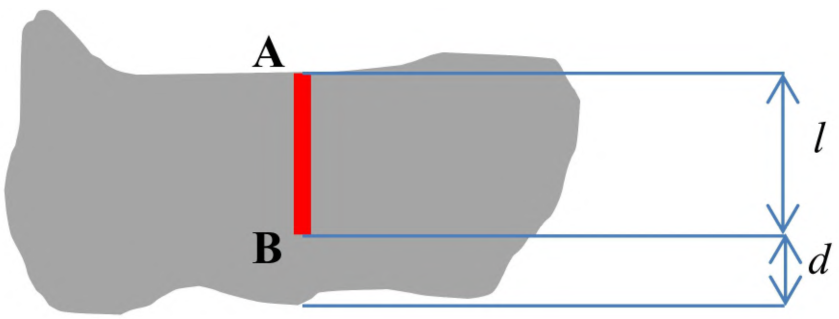

Fig. 5.5 Electrical conductivity based detection criterion for fabricated probe towards detection of an irregular bubble.

Equation (5.1) suggests that, for the given probe with a sensing tip of 1.5 mm, Ar bubbles with impaction chord lengths of 1.6 mm and 2 mm can be detected conclusively using the T_{90} threshold, if traversing the probe at resultant vertical velocities of upto 2.22 cm/s and 11.11 cm/s, respectively. Further performance enhancements are possible by reducing the length of the conducting tip and using needle shaped probes to detect smaller bubbles with increased travel velocities. A relaxation in the threshold criteria for a conclusive detection (eg: T_{50} or T_{75} instead of T_{90}) will further allow detection of same sized bubbles travelling with higher velocities.

5.3.2 Probe Performance In PbLi-Ar Two-Phase Flow At Low And Intermediate Void Fractions

Hybrid probe was exposed to two-phase flow regimes in PbLi-Ar vertical column with bulk PbLi temperature of 390°C and varying time-averaged void fractions (hereafter denoted as α). Obtained voltage pulses from electrical conductivity based measurements are normalized in binary, where data points with voltage magnitude ≥ 80% of the maximum voltage output are assigned a logic HIGH (1) and remaining data points are assigned a logic LOW (0). Here, for practical purposes, maximum voltage output is considered equal to the applied excitation voltage in view of high electrical conductivity of PbLi. Ratio of the number of data points with logic LOW to the total number of data points defines α for the time interval under consideration (Nuclear Energy Agency Handbook, 2015; Saraswat *et al.*, 2021).

Probe performance data for a continuous sample of 20 s (t = 0 to 20 s), extracted from one of the experimental runs of a total duration 200 s, is presented in this section in the form of simultaneous voltage data and temperature trends (Figure 5.6(a)–5.6(h)). As both the junctions of duplex thermocouple of the hybrid probe provided data in close agreement, temperature trend for only one junction is shown and discussed as a representative case. The temperature trend starts from 0.5 s in Figure 5.6(a) due to an applied moving average function as discussed above. For visualization purposes, ordinate range is kept as 30°C while abscissa range is maintained as 2.5s for all the cases with α mentioned at the top left corner for each analysed case. For instance, for Figure 5.6(a), logic LOW is assigned to 238 sample points (having voltage value < 4 V) out of a total number of 501 sampled points. This gives a time-averaged void fraction of 238/501 = 0.475 for the considered time duration. Figure 5.6(a)–5.6(h) depict characteristics of bubbly flow patterns occasionally tending towards a slug flow (Besagni *et al.*, 2018; Huang *et al.*, 2018; Valls *et al.*, 2020) without a clear distinction. This is in close agreement to the reported experimental observations in (Saito *et al.*, 2005), where no stable slug bubbles could be identified in PbBi-N_2 two-phase flow owing to high shearing stress of LM flow induced by preceding bubbles. Figure 5.6(i) depicts the case, near the end of same experimental run, when gas flow from the sparger is stopped and the probe is in PbLi environment continuously. Figure 5.7, taken from another experimental run, provides insight about two-phase PbLi-Ar flow at very low non-zero void fractions with stark characteristics of a well dispersed and well separated bubbly flow with Ar bubbles of varying diameters in PbLi continuum.

Variation in experimentally measured two-phase bulk temperature using hybrid probe is observed to be dependent on α. An increase in the Ar flow (leading to an increase in α) results in a decreasing trend in the measured two-phase bulk temperature and vice-versa. Obtained voltage data in agreement with temperature trends establishes reliable detection of two-phase using fabricated hybrid probe. It could be observed that for all the cases, measured two-phase bulk temperature is lower than the temperature of bulk PbLi, a phenomenon attributed to the coupled effect of forced convection by injected room temperature Ar gas and a resultant simultaneous decrease in the Effective Thermal Conductivity (ETC) of the two-phase mixture, leading to a reduced heat extraction from the continuously heated tank walls. A preliminary estimate suggests that the localized two-phase ETC falls to ~5.14% at α = 0.95. However, an exact estimation requires a complete information about volumetric void-distribution within the tank.

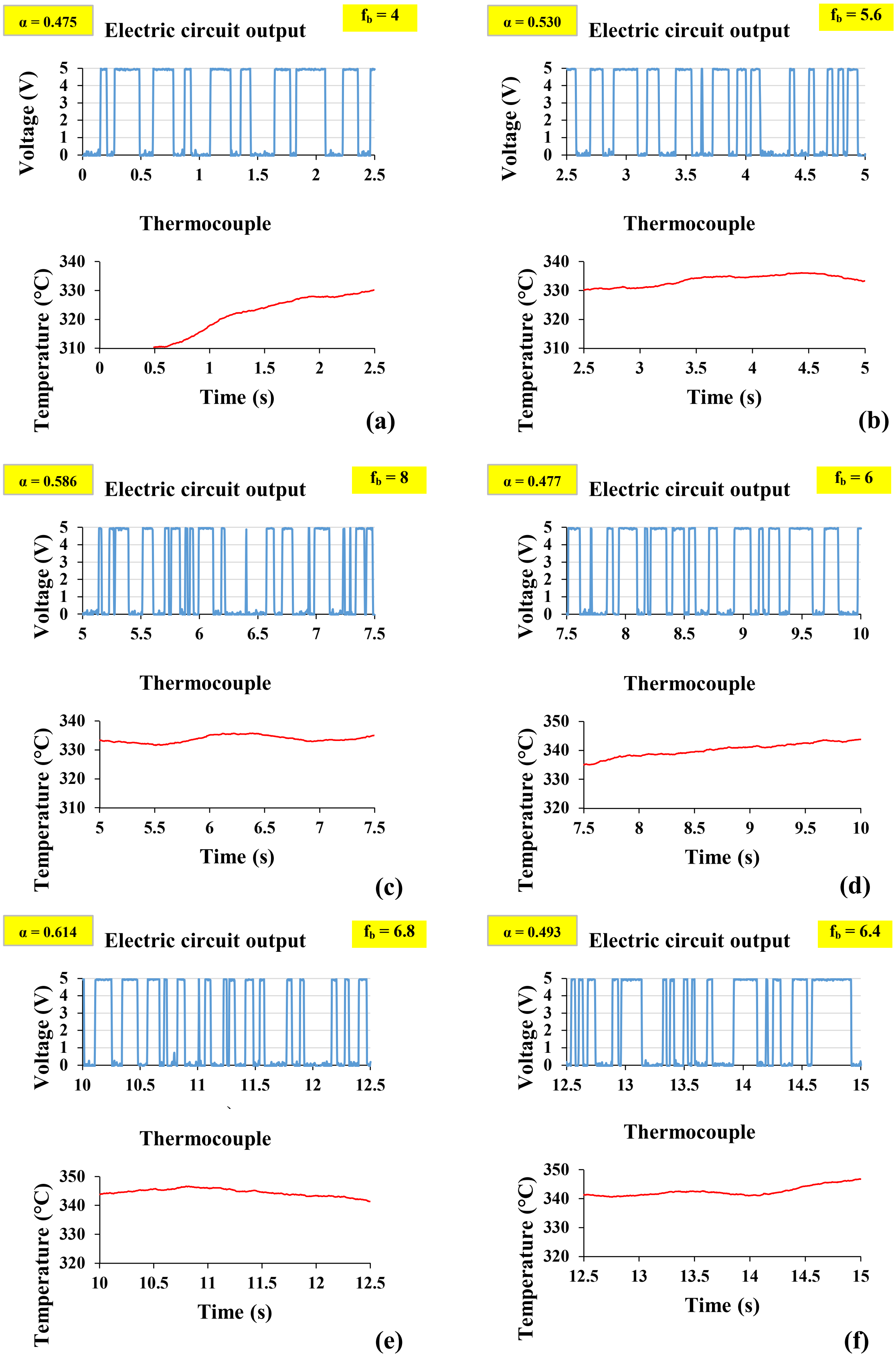

α = 0.475
Electric circuit output
f_b = 4
Voltage (V)
Thermocouple
Temperature (°C)
Time (s)
(a)
α = 0.530
Electric circuit output
f_b = 5.6
Voltage (V)
Thermocouple
Temperature (°C)
Time (s)
(b)
α = 0.586
Electric circuit output
f_b = 8
Voltage (V)
Thermocouple
Temperature (°C)
Time (s)
(c)
α = 0.477
Electric circuit output
f_b = 6
Voltage (V)
Thermocouple
Temperature (°C)
Time (s)
(d)
α = 0.614
Electric circuit output
f_b = 6.8
Voltage (V)
Thermocouple
Temperature (°C)
Time (s)
(e)
α = 0.493
Electric circuit output
f_b = 6.4
Voltage (V)
Thermocouple
Temperature (°C)
Time (s)
(f)

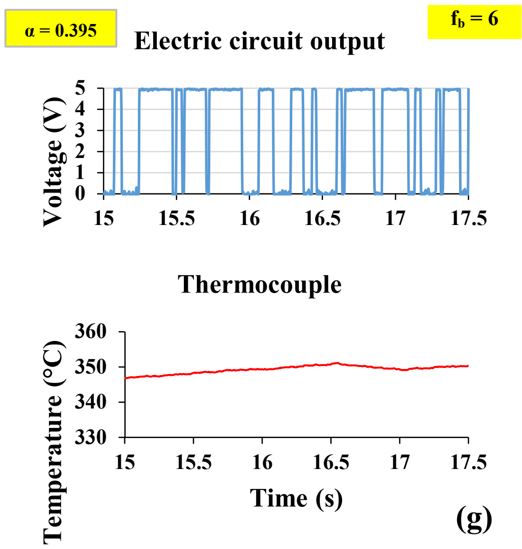

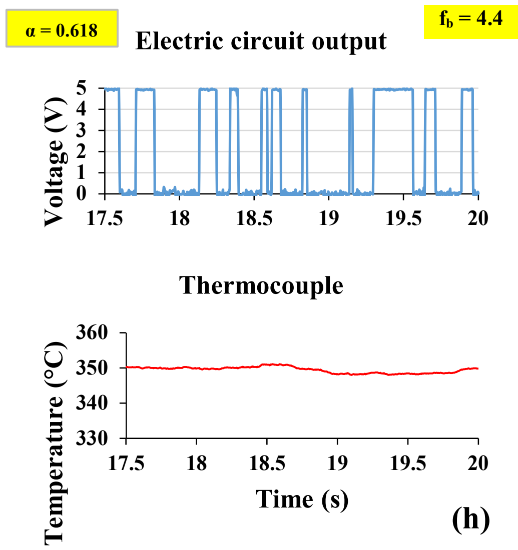

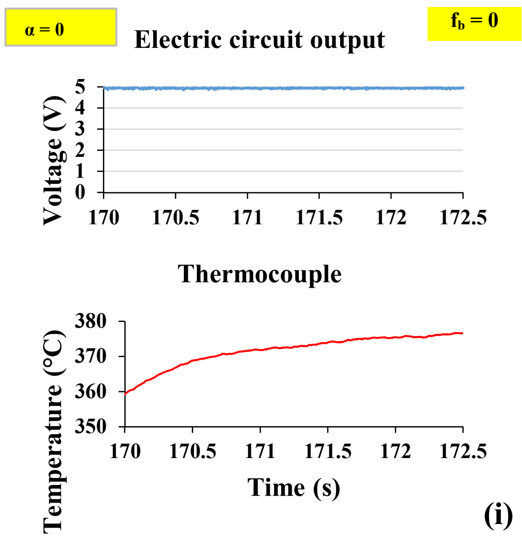

Fig. 5.6 (a)-(i): Performance of probe for varying α.

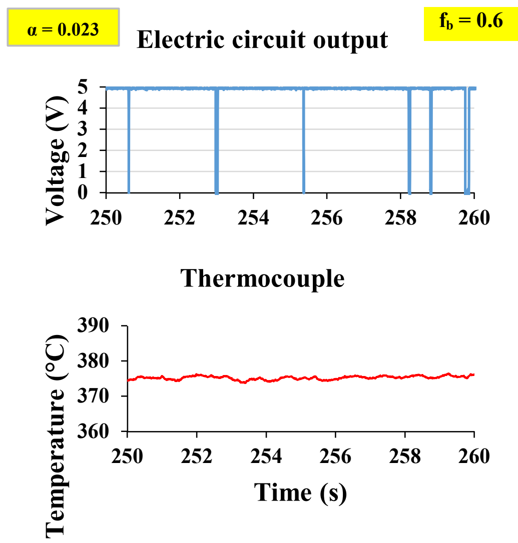

Fig. 5.7 Performance of probe at very low (non-zero) α.

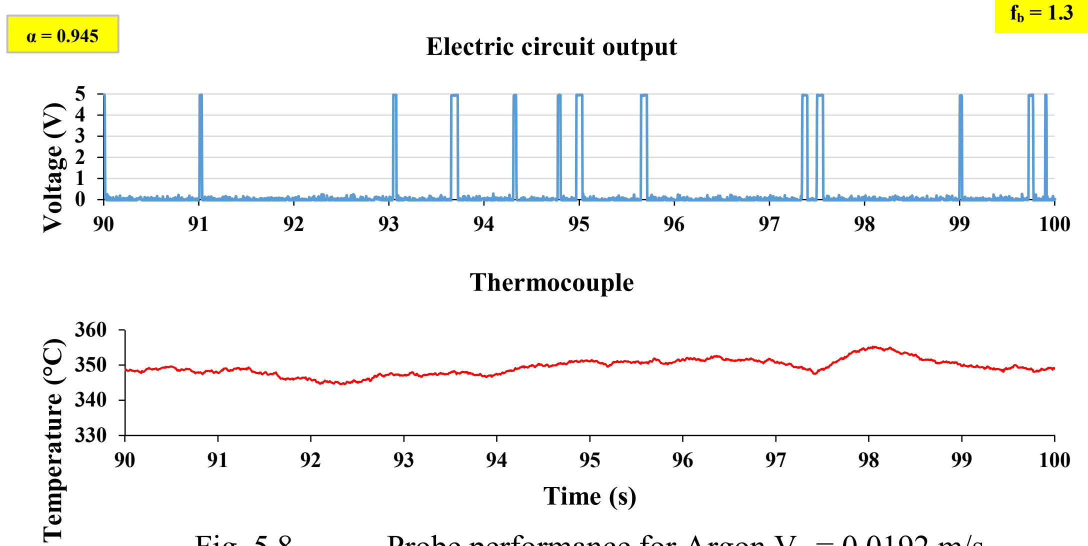

Fig. 5.8 Probe performance for Argon $V_g = 0.0192$ m/s.

Restricted flow of Ar (α = 0 and 0.02) in Figure 5.6(i) and Figure 5.7 rapidly drives the two-phase temperature towards bulk PbLi temperature. An important observation from these tests is that although each bubble could be detected using the electrical conductivity principle, only a trend could be obtained through two-phase bulk temperature measurements which could provide qualitative inference about an overall presence of two-phase. An adaptation of measurement probe using micro-thermocouples with better response may lead to quantification of two-phase flow using temperature data alone.

5.3.3 Bubble Frequency And Average Bubble Residence Time Estimations

In the present scenario, with a single tip probe, detection of bubble velocity or bubble chord length is not possible in absence of a reference time frame. However, the bubble frequency (f_b), a critical parameter defined as the ratio of number of bubbles (N) impacting the probe to the given time duration (T), can be estimated (Ariyoshi, 2019) from the relation below:

$$f_b = N/T \tag{5.2}$$

Taking the cases of Figure 5.6(a) and Figure 5.6(d) with nearly same α, estimated bubble frequencies are 4 bubble/s and 6 bubble/s respectively. Differences in the observed bubble frequencies could be explained by the fact that over the complete 2.5 s duration, distribution of voids in these two cases is not similar. Moreover, as the void fraction rises, the bubble frequency is expected to increase in a dispersed bubbly flow regime. However, coalescence of bubbles gives rise to gas pockets with larger impaction chords resulting in a higher magnitude of α, but effectively reducing the bubble count within same time as can be observed for Figure 5.6(h) with an estimated bubble frequency of 4.4 bubble/s. The bubble frequency can be further utilized to estimate the average bubble residence time (T_b), i.e. the average time a bubble takes to traverse through the probe tip, defined as the ratio of time-averaged void fraction to bubble frequency (Ariyoshi, 2019):

$$T_b = \alpha/f_b \tag{5.3}$$

For the cases of Figure 5.6(a) and Figure 5.6(d) with similar α, estimated average bubble residence times are 118.75 ms and 79.5 ms, respectively. This also corroborates that although the magnitude of α for both these cases is almost same, the time distribution of interaction of the liquid and gas phases with the probe tip varies significantly, as experimentally observed from the logged voltage dips. For the case in Figure 5.6(h) with higher α, estimated average bubble residence time is 140.45 ms, which seems to be the effect of bubble coalescence in accordance to the discussion made above. For the case of very low α (Figure 5.7), estimated parameters are 0.6 bubble/s and 38.33 ms, respectively.

5.3.4 Probe Performance In PbLi-Ar Two-Phase Flow At High Void Fractions (In-box LOCA)

One of the postulated accidental events for PbLi cooled TBM concepts is an in-box TBM LOCA where the high pressure coolant (helium/water) enters the PbLi loop, pressurizing the complete LM system. A relevant recent simulation study for PbLi-He two-phase flow (Valls *et al.*, 2020) has considered helium fractions in the range of 0.1–0.9 with mixture velocities between 0.0001 m/s and 100 m/s.

In the present experimental study, controlled Ar flow rates varying from 1.5 slpm to 3.5 slpm, corresponding to superficial gas flow velocities ranging from 0.0115 m/s to

0.0269 m/s (at standard conditions), have been injected in the test facility using a DMFC to achieve α ~ 0.95 over continuous durations as long as 200 s with bulk PbLi temperature of 400°C. A representative sample of 10 s extracted from the case of Ar injection at 2.5 slpm, corresponding to a superficial gas velocity of 0.0192 m/s, is shown in Figure 5.8. The flow pattern indicated by the voltage signal clearly establishes a localized two-phase regime tending towards an annular flow with bubble frequency as low as 1.3 bubble/s and an average bubble residence time as large as 726.92 ms. In contrast to the bubbly flow, the high bubble residence time is indicative of flow pattern tending towards a dispersed PbLi phase within Ar gas continuum near the probe tip. This observation is also in agreement with the annular flows reported in the numerical study (Valls *et al.*, 2020). The average temperatures measured by the multivariable probe and PbLi bulk temperature sensor over the presented time duration match within ±1°C to the corresponding averages over complete test duration of 250 s, justifying the analysed sample being a representative case.

The total duration of continuous exposure of the probe in high α (> 0.9) PbLi-Ar two-phase environment was over 2 h. No distortions in the voltage signal were observed related to degradation of the coated section as reported in (Muñoz-Cobo *et al.*, 2017). During the tests, hybrid probe was exposed to temperature gradients as large as 300°C within a few seconds (during immersion) and pressure gradients upto 1 bar(g) during sparger tests using venting. Additionally, the installation scheme adopted for the present study exposes the probe to high thermal gradients (> 300°C) along the length due to partial immersion in PbLi and partial exposure outside the facility port. No adverse effects of such gradients were observed on the probe performance. Measured IR > 275 GΩ at 275 VDC post exposure to PbLi environment also corroborates the integrity of applied coating. In view of the performance observed, the developed probe is expected to sustain the temperature gradients typically encountered in a liquid metal circuit, without significant impact on its functionality.

An image of the probe and gas sparger after retrieval from the test tank is shown in Figure 5.9. Silvery lustrous deposition of PbLi on the immersed portion of probe is due to installation constraints of the present facility, requiring retrieval of the probe before the retrieval of sparger, leading to solidification of PbLi near the probe tip. The probe was chemically cleaned and re-tested for satisfactory performances in PbLi-Ar bubbly columns.

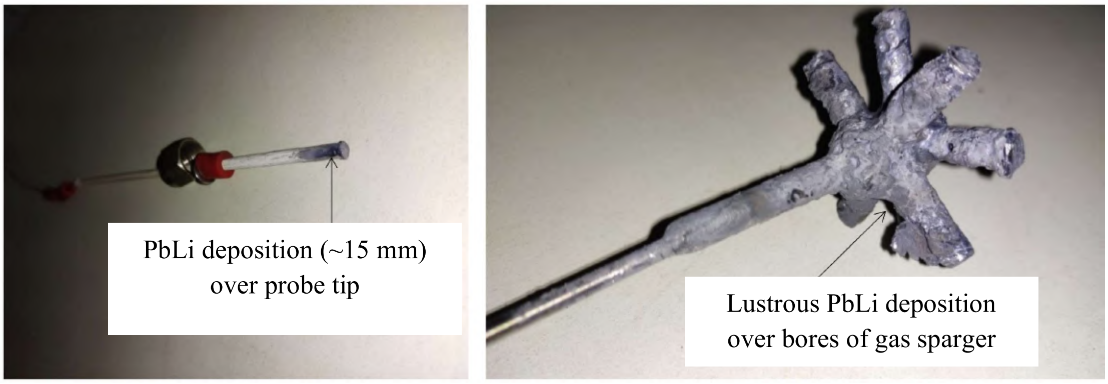

Fig. 5.9 Condition of probe and gas sparger after exposure to PbLi-Ar environment.

Lead and its alloys generally exhibit poor wettability with stainless steels (Nuclear Energy Agency Handbook, 2015; Lu *et al.*, 2017). However, liquid metal contact over longer operational duration may modify the surface conditions resulting in non-wetting to wetting transition. This may lead to liquid metal deposition over the conducting tip of the probe rendering the two-phase sensing difficult. In this view, it is proposed that installation of the probe can be achieved through an isolation valve, allowing online retraction and cleaning/maintenance of the probe at regular intervals. Considering a continuous PbLi exposure and in view of practical operational experiences, it is foreseen that frequent visual observations/maintenance of the probe may be required until sufficient data is generated through experiments. Further configurations of sparger are also being considered to achieve a better draining of PbLi LM after retrieval from the facility.

5.4 CONCLUSION

The major conclusions derived from the third experimental study are mentioned below:

- The developed multivariable probe provides detection/estimation of time-averaged void fraction, bubble frequency, average bubble residence time and two-phase bulk temperature.

- Electrical conductivity based detection scheme provides quantitative detection of two-phase flow while the coherent two-phase bulk temperature trends provide qualitative insights about overall presence of a two-phase flow.

- In the present study, upto 8 bubble/s (at α ~0.58) could be resolved successfully using the developed probe. Further, it is experimentally observed that generally for $\alpha \leq 0.6$, the bubble frequency tends to increase with an increase in α. For $\alpha > 0.6$, however, the bubble frequency shows a decreasing trend with an increased gas phase fraction leading to an increased bubble residence time. This phenomenon could be primarily attributed to the coalescence of smaller gas pockets. However further detailed experimentation is required to ascertain the same.

- The experimental studies validate functional validity of the fabricated probe for α from 0 to 0.95 covering a wide range of flow regimes.

5.5 CLOSURE

A multivariable/hybrid probe based on the electrical conductivity principle employing simultaneous bulk temperature measurements has been designed and fabricated to experimentally study PbLi (liquid)-Ar (gas) two-phase flow in vertical columns with bulk PbLi temperatures upto 400°C. To adapt the electrical conductivity based technique for corrosive PbLi environments, high purity Al_2O_3 coatings were applied as electrical insulation over the immersed portion of the probe. The developed probe was calibrated and validated for its functionality under different two-phase flow regimes i.e., single phase flow, dispersed bubbly-flow, transition regime towards slug flow and localized annular flows with α varying from 0 to 0.95. Bubble detection criterion based on the response time for a given threshold was discussed to correlate the bubble velocity and dimension of impaction chord towards a conclusive detection.

The developed probe was successfully utilized under highly turbulent flow regimes with Ar gas flow rates upto 3.5 slpm. Although an unavailability of fully developed flow regime in the present facility limits identification of clear transitions between different flow regimes, the primary aim of validating the developed probe as a tool towards experimental detection of PbLi-Ar two-phase flows at relevant operating temperature has been successful considering the satisfactory functioning of probe covering most of the operational ranges of time-averaged void fraction. Considering initial applications of the probe in lab-scale PbLi facilities at IPR, typical operating conditions include operating temperature range of 300°C - 400°C, operating pressure range of 1-3 bar (g) and PbLi flow velocities varying between 0.1 – 0.4 m/s.

Future activities include miniaturization of the hybrid probe to expand the measurability for smaller diameter dispersed bubbles and to enhance the response of temperature sensors. A dual-tip version will be fabricated to understand the evolution of bubble size and bubble velocities with varying void fractions of Ar/He pockets in PbLi environment. Developed probe system is expected to be an indispensable tool enabling future experimental studies on two-phase flow at high temperature providing substantiation for software models being developed for advanced LM based breeding blanket concepts.

CHAPTER 6

CONCLUSIONS AND FUTURE SCOPE

6.1 INTRODUCTION

The experimental investigation presented in the thesis is primarily organized under three stages. In the first stage, experimental studies were carried out towards detection of vertically rising air bubbles in a water column with an electrical conductivity based probe. Bubbles were quantified through experimental measurements and estimations of discrete voltage dips, bubble impaction chord length and time-averaged void fractions. To adapt the electrical conductivity principle for high temperature PbLi scenario, in the second stage, long duration experiments were conducted towards validation of electrically insulating alumina coatings in high temperature PbLi environment with experimental measurements and estimations of insulation resistance, volumetric electrical resistivity and temperature dependent IR derating factors. Further, the coating characterization provided detailed insights about coating thickness variations, LM ingress depth and surface/particle morphologies. Experiences gained from the first two stages were utilized in the third stage to fabricate a multivariable probe with a basic temperature sensor functionally enhanced through the application of validated alumina coating to provide means of electrical conductivity based bubble detection and measurements of two-phase bulk temperature in PbLi-argon vertical columns. The developed probe was employed for estimations of time-averaged void fractions, bubble frequency and average bubble residence time in high temperature PbLi environment.

6.2 BROAD CONCLUSIONS FROM THE PRESENT STUDY

Major conclusions from the study are provided below:

- Electrical conductivity based detection scheme provides good temporal resolution and high reliability towards conclusive detection of gas pockets in liquid. This scheme could detect all the bubbles colliding with the probe sensing tip.

- Coating deposition method optimized for $AlPO_4$ bonded alumina requires a low temperature exposure of the substrate and could be homogenized for different substrate materials using the same heat curing parameters. The validated coating method exhibits compactness, non-porosity and good adherence to the substrate.

- Validated coating is assessed promising in terms of electrical insulation integrity, chemical compatibility and high temperature endurance in static PbLi environment for time durations upto 1300 h at temperature between 300°C-400°C.

- Observed temperature dependent degradation of insulation resistance is much better than that of commercial insulations. However, brittleness observed is one of the concerns which need further experimentation towards improvements.

- Quantification of two-phase parameters like time-averaged void fraction, bubble frequency and average bubble residence time is possible using the electrical conductivity based detection scheme alone. Estimation of parameters like impaction chord length and bubble travel velocity, however, requires a reference time frame.

- Developed two-phase detection probe could provide a reliable detection over a wide range of flow regime i.e. for time-averaged void fraction upto 0.95 over an operational bulk temperature of 400°C.

- Experimental observations suggest coalescence of gas pockets above a time-averaged void fraction of 0.6 under PbLi environment with a decrease in bubble frequency and simultaneous increase in the average bubble residence time.

6.3 FUTURE SCOPE OF WORK

Experiences gained from the present study further pave the path for an advancement of the developed detection tool. Although time-averaged void fractions are relevant to study localized phenomena, it is of extreme importance to be able to measure the presence of two-phase regimes across a wider cross-section. In this view, a sensor array, as shown in Figure 6.1, is being planned for initial implementations in PbLi-Ar/He vertical columns in a rectangular duct.

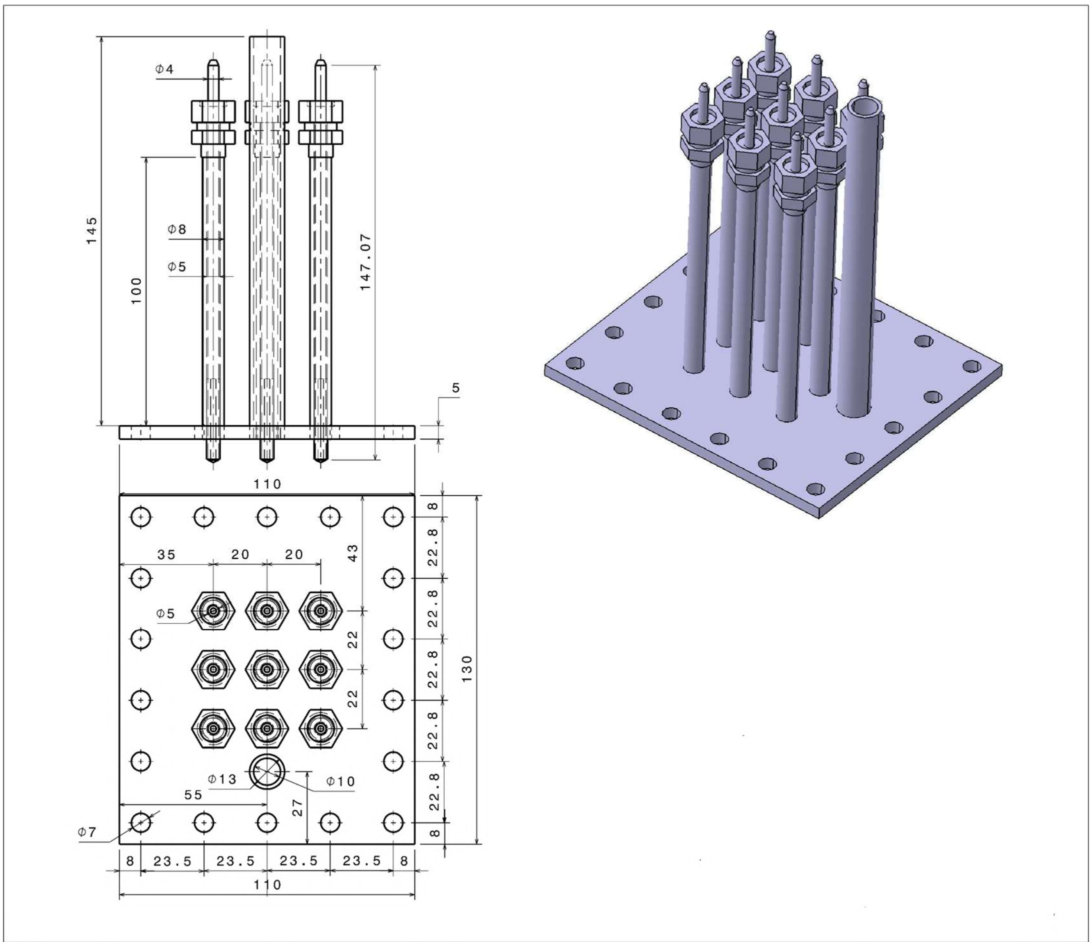

Fig. 6.1 Proposed two-phase detection sensor array assembly for PbLi-Ar vertical flow across wider cross-sections in a rectangular duct.

Later, to accommodate the practical deployment in the PbLi loop pipelines of lab scale facilities, a 2-inch flanged configuration sensor array compatible for installation in a vertical as well as horizontal orientation is designed as shown in Figure 6.2. In this configuration, an added advantage is the feasibility of traversing individual probes to get information about radial variation of time-averaged void fraction.

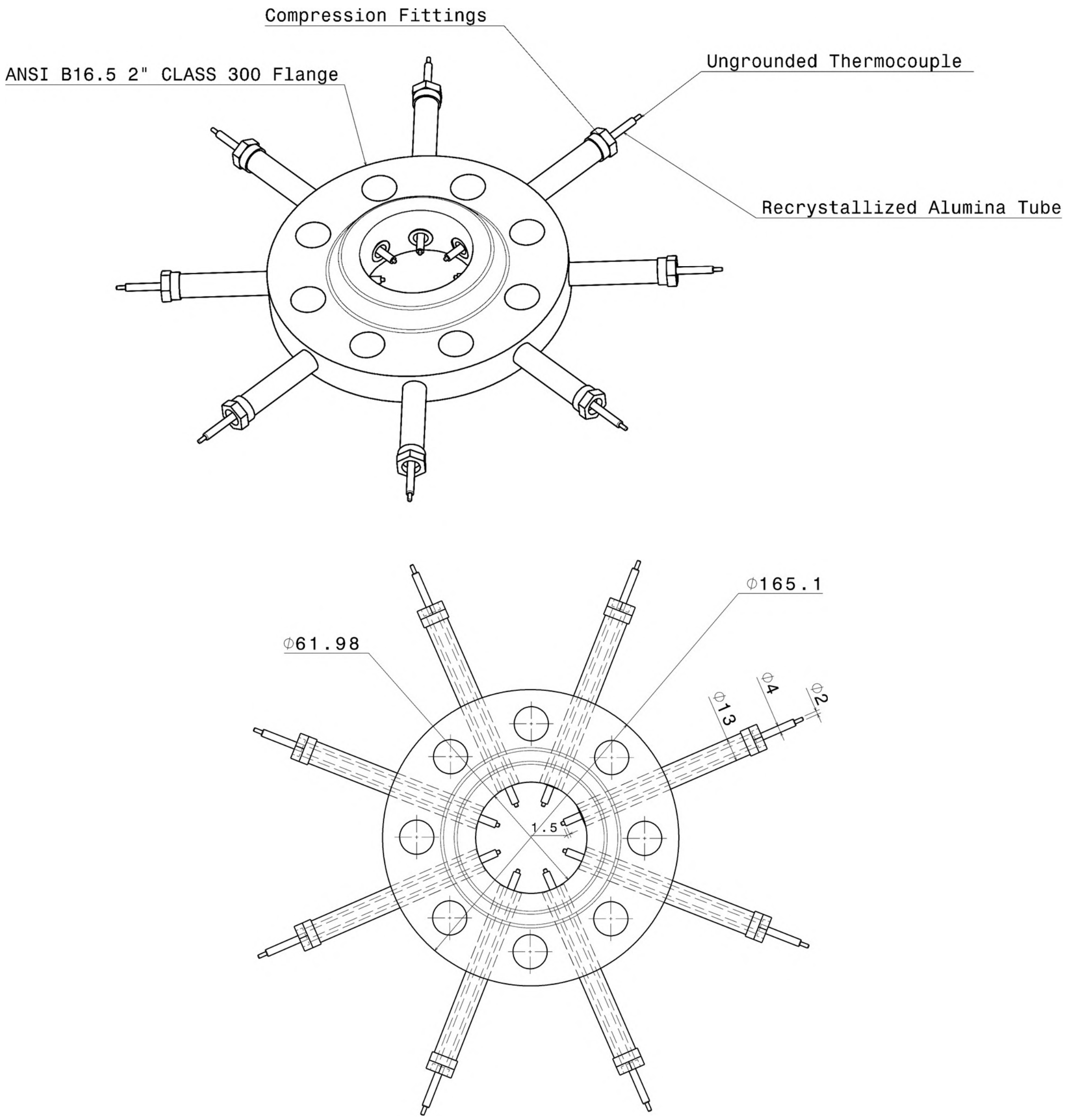

Fig. 6.2 Proposed two-phase detection sensor array for wider cross-sectional measurements in PbLi loop pipelines (horizontal and vertical).

As electrical conductivity based detection is an intrusive technique, inherent modification of the flow geometry and bubble dynamics is inevitable. To minimize these effects due to probe-bubble interaction, miniaturization is envisaged using fine diameter thermocouples to fabricate dual-tip probes (Nuclear Energy Agency Handbook, 2015) for estimations of bubble velocity and impaction chord length. Tests will involve flow of both the phases for more realistic representation of the operational cases and to characterize flow regimes in advanced breeder blanket configurations. Although the present study validates the probe for applications in PbLi environment only, chemical compatibility of SS-316 (probe tip) and alumina, which is the major constituent of the coating material, allows utilization of the probe in other liquid metals (like PbBi, Hg, Na, GaInSn etc.). Detailed experimental studies are however required to quantify the degradation in probe performance considering the scarcity of chemical compatibility data for Al_2O_3 and $AlPO_4$ as coating-bonding agents.

In view of practical implementation in a radiation environment relevant to fusion reactors, candidate materials for probe tip may include SS-316L/SS-316L(N)-IG/RAFMS depending on the commercial availability and fabricability constraints. Data from these studies could be utilized towards validation of simulation models and codes, presently under development, to predict the effects of postulated events/accidents in a TBM and/or fusion machine employing LM breeders and coolants.

In addition to the above mentioned plans, the extended future scope of work is summarized below:

- Deposition and performance validation of alumina coating in a graded coating composition. For instance, an SS-410 intermediate layer deposited between the SS-316L substrate and topmost Al_2O_3 layer may provide a better adhesion and sustain thermal gradients considering a gradual variation in CTEs across different layers.

- Miniaturization of the probe using fine diameter thermocouples to enhance thermal response and to minimize probe-bubble interactions. A dual-tip version of the probe will further provide the required time reference to experimentally estimate bubble impaction chord lengths and bubble rise velocity.

- Experimental validation in flowing heavy LM loop(s) with extended flow sections (fully developed flow profiles) for detailed study on the transitions between different two-phase flow regimes.

6.4 CLOSURE

This chapter presented major conclusions derived from the conducted experiments and a scope for future work is discussed.

APPENDIX A

ESTIMATIONS OF VOLUMETRIC ELECTRICAL RESISTIVITY AND COATING RESISTANCE

Insulation resistance of an electrical cable is given by the following relation:

$$\mathbf{R_i} = \left(\frac{\varrho}{2\Pi L}\right) \ln \frac{R}{r} \tag{A.1}$$

Where,

R_i = Insulation resistance of the cable (Ω),

ϱ = Volumetric electrical resistivity of insulation material (Ω-m),

L = Length of the insulation over the cable (m),

R = Outer radius of the cable with insulation (m) and

r = Outer radius of the conductor (m).

Using data from Table 4.1 to Table 4.5 and taking the enveloping IR values at each temperature:

Table A.1 Estimated volumetric electrical resistivity and coating resistance.

Test Campaign	Probe	Insulation Resistance (Ω)	Avg. coating thickness (mm)	Coated length (m)	Temperature (°C)	Resistivity (Ω-cm)	Coating resistance (Ω-m²)
1	P1	6×10^9	0.495	0.085	300	6.65×10^{11}	3.29×10^6
		6.18×10^9	0.495	0.085	300	6.85×10^{11}	3.39×10^6
		0.822×10^9	0.495	0.085	350	9.12×10^{10}	4.51×10^5
		1×10^9	0.495	0.085	350	1.11×10^{11}	5.49×10^5
	P2	1×10^8	0.212	0.065	300	1.74×10^{10}	3.68×10^4
		3.15×10^8	0.212	0.065	300	5.47×10^{10}	1.16×10^5
		0.835×10^8	0.212	0.065	350	1.45×10^{10}	3.08×10^4
		1×10^8	0.212	0.065	350	1.74×10^{10}	3.68×10^4
2	P3	2.90×10^8	0.429	0.060	300	2.55×10^{10}	1.09×10^5
		4.57×10^8	0.429	0.060	300	4.01×10^{10}	1.72×10^5
		1.29×10^8	0.429	0.060	350	1.13×10^{10}	4.86×10^4
		2.99×10^8	0.429	0.060	350	2.63×10^{10}	1.13×10^5
		0.583×10^8	0.429	0.060	400	5.12×10^9	2.20×10^4
		0.768×10^8	0.429	0.060	400	6.74×10^9	2.89×10^4

APPENDIX B

UNCERTAINTY ANALYSIS

The following table (Table B.1) presents details of the uncertainties in the primary measured quantities/variables using sensors and instrumentation utilized throughout the work reported in this thesis. The uncertainty values have been taken from the reference manuals from the instrument technical specification datasheet and calibration standards for the utilized sensors.

Table B.1 Uncertainties in the measured quantities.

S. No.	Instrument/Sensor	Measured quantity	Uncertainty
1.	Thermocouple	Temperature	As per IEC 60584-2, Class-1 (± 1.5°C or ± 0.4% of measured temperature, whichever is greater)
2.	Insulation resistance tester	Insulation resistance	± 5% of measured IR value
3.	PXIe-6363	Voltage	Absolute accuracy: < ± 33 µV (-100 to 100 mV range) Absolute accuracy: < ± 1660 µV (-10 to 10 V range)
4.	Pressure transmitter	Pressure	± 0.1% of calibrated span (0-10 bar(g))
5.	Digital pressure gauge	Pressure	± 0.1% of calibrated span (0-12 bar(g))
6.	DMFC	Mass flow rate	± 1% of measured flow rate
7.	SEM	Coating thickness	± 10-50 nm

Utilizing the uncertainties in the primary measured variables, an uncertainty analysis has been carried out for the derived quantities using the error propagation relation. Table B.2 below provides the estimated uncertainties for the derived quantities.

Table B.2 Estimated uncertainties in the derived quantities.

S. No.	Derived quantity	Uncertainty
1.	Electrical resistivity	± 5%
2.	Bubble frequency (bubbles/s) (for considered time duration = 2.5 s for Fig. 5.6(a) – Fig. 5.6(h))	Mean = 5.9 Systematic uncertainty = ± 0.005% Random uncertainty = ± 21.668% Total uncertainty = 1.278 Total uncertainty (%) = ± 21.668%
3.	Time-averaged void fraction (for considered time duration = 2.5 s for Fig. 5.6(a) – Fig. 5.6(h))	Mean = 0.523 Systematic uncertainty = ± 0.007% Random uncertainty = ± 14.976% Total uncertainty = 0.078 Total uncertainty (%) = ± 14.976%
4.	Bubble residence time (s) (for considered time duration = 2.5 s for Fig. 5.6(a) – Fig. 5.6(h))	Mean = 0.092 Systematic uncertainty = ± 0.009% Random uncertainty = ± 27.383% Total uncertainty = 0.025 Total uncertainty (%) = ± 27.383%

REFERENCES

1. **Abdou**, **M.**, **N. B. Morley**, **S. Smolentsev**, **A. Ying**, **S. Malang**, **A. Rowcliffe and M. Ulrickson** (2015) Blanket/first wall challenges and required R&D on the pathway to DEMO. *Fusion Engineering and Design*, **100**, 2-43.

2. **Anderson**, **J. L. and J. R. Fincke** (1980) Mass flow measurements in air-water mixtures using drag devices and gamma densitometer. *ISA Transactions*, **19**(1), 37-48.

3. **Andreini**, **R. J.**, **J. S. Foster and R. W. Callen** (1977) Characterization of gas bubbles injected into molten metals under laminar flow conditions. *Metallurgical Transactions B*, **8**, 625–631.

4. **Andruszkiewicz**, **A.**, **K. Eckert**, **S. Eckert and S. Odenbach** (2013) Gas bubble detection in liquid metals by means of the ultrasound transit-time-technique. *The European Physical Journal Special Topics*, **220**, 53–62.

5. **Andruszkiewicz**, **A. and K. Eckert** (2018) Experimental studies of two-phase liquid metal-gas chain flow with ultrasonic echo pulse method and in the magnetic field of permanent magnets. *MATEC Web of Conferences*, **240**, 03003.

6. **Ariyoshi**, **G.** (2019) Flow Characteristics of Lead-Bismuth Two-phase Flow. *PhD Thesis*, Kyoto University.

7. **Ariyoshi**, **G.**, **D. Ito and Y. Saito** *Experimental Study of Flow Structure and Turbulent Characteristics in Lead–Bismuth Two-Phase Flow*. pp. 107-115. *In* **Nakajima K.** (eds.) *Nuclear Back-end and Transmutation Technology for Waste Disposal*. Springer, Tokyo, 2015.

8. **Atchutuni**, **S. S.**, **A. Saraswat**, **C. S. Sasmal**, **S. Verma**, **A. K. Prajapati**, **A. Jaiswal**, **S. Gupta**, **J. Chauhan**, **K. B. Pandya**, **M. Makwana**, **H. Tailor**, **H. S. Agravat**, **P. Rao and E. Rajendrakumar** (2018) Corrosion experiments on IN-RAFM steel in flowing lead-lithium for Indian LLCB TBM. *Fusion Engineering and Design*, **132**, 52-59.

9. **Bertola**, **V.** (2003) Two-Phase Flow Measurement Techniques. *In: Bertola V. (eds) Modelling and Experimentation in Two-Phase Flow. International Centre for Mechanical Sciences (Courses and Lectures)*, **450**, 281-323.

10. **Besagni**, **G.**, **F. Inzoli and T. Ziegenhein** (2018) Two-Phase Bubble Columns: A Comprehensive Review. *ChemEngineering*, **2**(2), 13.

11. **Borgstedt**, **H. U.**, **H. Glasbrenner and Z. Peric** (1994) Corrosion of insulating layers on MANET steel in flowing Pb-17Li. *Journal of Nuclear Materials*, **212-215**(B), 1501-1503.

12. **Bühler**, **L. and C. Mistrangelo** (2018) Pressure drop and velocity changes in MHD pipe flows due to a local interruption of the insulation. *Fusion Engineering and Design*, **127**, 185-191.

13. **Buhler**, **L. and S. Molokov** (1993) Magnetohydrodynamic flows in ducts with insulating coatings. *Rep. KfK-5103*, Kernforschungszentrum Karlsruhe.

14. **Cha**, **J. E.**, **Y. C. Ahn**, **K. W. Seo**, **H. Y. Nam**, **J. H. Choi and M. H. Kim** (2003) The Performance of Electromagnetic Flowmeters in a Liquid Metal Two-Phase Flow. *Journal of Nuclear Science and Technology*, **40**(10), 744-753.

15. **Cha**, **J. E.**, **I. C. Lim**, **H. R. Kim**, **C. M. Kim**, **H. Y. Nam and Y. Saito** (2005) Measurement of Liquid-Metal Two-Phase Flow with a Dynamic Neutron Radiography. *Transactions of the Korean Nuclear Society Autumn Meeting*, Busan, Korea.

16. **Chen**, **D.**, **L. He and S. Shang** (2003) Study on aluminum phosphate binder and related Al_2O_3-SiC ceramic coating. *Materials Science and Engineering: A*, **348**(1-2), 29-35.

17. **Chen**, **J. C.**, **S. Kalish and G. A. Schoener** (1968) Probe for Detection of Voids in Liquid Metals. *Review of Scientific Instruments*, **39**, 1710.

18. **Chikada**, **T.**, **A. Suzuki**, **Z. Yao**, **D. Levchuk**, **H. Maier**, **T. Terai and T. Muroga** (2009) Deuterium permeation behavior of erbium oxide coating on austenitic, ferritic, and ferritic/martensitic steels. *Fusion Engineering and Design*, **84**(2-6), 590–592.

19. **Conrad**, **R.** (1991) Irradiation experiments on liquid tritium breeding material Pb-17Li in the HFR Petten. *Fusion Engineering and Design,* **14**, 289-297.

20. **Corazzaa**, **C.**, **K. Rosseel**, **W. Leysen**, **K. Gladinez**, **A. Marino**, **J. Lim and A. Aerts** (2020) Optical fibre void fraction detection for liquid metal fast neutron reactors. *Experimental Thermal and Fluid Science*, **113**, 109865.

21. **Courtessole**, **C.**, **S. Smolentsev**, **T. Sketchley and M. Abdou** (2016) MHD PbLi experiments in MaPLE loop at UCLA. *Fusion Engineering and Design*, **109-111**(A), 1016-1021.

22. **Eckert, S.**, **G. Gerbeth and O. Lielausis** (2000) The behaviour of gas bubbles in a turbulent liquid metal magnetohydrodynamic flow: Part I: Dispersion in quasi-two-dimensional magnetohydrodynamic turbulence. *International Journal of Multiphase Flow,* **26**(1), 45-66.

23. **Feng, S.**, **Y. Wang**, **C. Zhang**, **C. Luo**, **J. Xu and J. Suo** (2018) Preparation of Al_2O_3/Cr_2O_3 tritium permeation barrier with combination of pack cementation and sol–gel methods. *Fusion Engineering and Design*, **131**, 1–7.

24. **Fernández-Berceruelo**, **I.**, **M. Gonzalez**, **I. Palermo**, **F. R. Urgorri and D. Rapisarda** (2018) Large-scale behavior of sandwich-like FCI components within the EU-DCLL operational conditions. *Fusion Engineering and Design,* **136**(A), 633-638.

25. **Fraile**, **A. and T. Polcar** (2020) Volume and pressure of helium bubbles inside liquid Pb16Li. A molecular dynamics study. *Nuclear Fusion*, **60**, 046018.

26. **Gajjar**, **P.**, **T. Haas**, **K. B. Owusu**, **M. Eickhoff**, **P. Kowitwarangkul and H. Pfeifer** (2019) Physical study of the impact of injector design on mixing, convection and turbulence in ladle metallurgy. *Engineering Science and Technology, an International Journal*, **22**(2), 538-547.

27. **Gardenghi**, **A. R.**, **E. S. Filho**, **D. G. Chagas**, **G. Scagnolatto**, **R. M. Oliveira and C. B. Tibiriçá** (2020) Overview of Void Fraction Measurement Techniques, Databases and Correlations for Two-Phase Flow in Small Diameter Channels. *Fluids*, **5**(4), 216.

28. **Gazquez**, **M. C.**, **S. Bassini**, **T. Hernandez and M. Utili** (2017) Al_2O_3 coating as barrier against corrosion in Pb-17Li. *Fusion Engineering and Design*, **124**, 837-840.

29. **Giulio**, **D. D.**, **D. Suarez**, **L. Batet**, **E. M. Valls and L. Savoldi** (2020) Analysis of flow channel insert deformations influence on the liquid metal flow in DCLL blanket channels. *Fusion Engineering and Design*, **157**, 111639.

30. **González**, **M. and M. Kordac** (2020) Electrical resistivity behaviour of alumina flow channel inserts in PbLi. *Fusion Engineering and Design,* **159**, 111761.

31. **Guichou, R.**, **P. Tordjeman**, **W. Bergez**, **R. Zamansky and K. Paumel** (2017) Experimental study of bubble detection in liquid metal. *Journal of Magnetohydrodynamics*, **53**(4), 667-676.

32. **Gundrum**, **T.**, **P. Büttner**, **B. Dekdouk**, **A. Peyton**, **T. Wondrak**, **V. Galindo and S. Eckert** (2016) Contactless Inductive Bubble Detection in a Liquid Metal Flow. *Sensors*, **16**(1), 63.

33. **Huang**, **S.**, **X. Wu**, **B. Zong**, **Y. Ma**, **X. Guo and D. Wang** (2018) Local void fractions and bubble velocity in vertical air-water two-phase flows measured by needle-contact capacitance probe. *Science and Technology of Nuclear Installations*, 7532618.

34. **Iadicicco**, **D.**, **M. Vanazzia**, **F. G. Ferré**, **B. Paladino**, **S. Bassini**, **M. Utili and F. Di Fonzo** (2019) Multifunctional nanoceramic coatings for future generation nuclear systems. *Fusion Engineering and Design* **146**(B), 1628-1632.

35. **IAEA technical meeting** (2006) Characterization and Testing of Materials for Nuclear Reactors. *Proceedings of a technical meeting held in Vienna, May 29–June 2, 2006:* IAEA-TECDOC-1545.

36. **Iguchi**, **M.**, **H. Kawabata**, **Z. Morita**, **K. Nakajima and Y. Ito** (1994) Continuous measurements of bubble characteristics in a molten iron bath with Ar gas bubbling. *Tetsu-to-Hagane*, **80**(5), 365-370.

37. **Iguchi**, **M.**, **H. Kawabata**, **K. Nakajima and Z. Morita** (1995) Measurement of bubble characteristics in a molten iron bath at 1600°C using an electroresistivity probe. *Metallurgical and Materials Transactions B*, **26**, 67–74.

38. **Jain**, **U.**, **A. Mukherjee**, **S. Sonak**, **S. Kumar**, **R. Mishra and N. Krishnamurthy** (2014) Interaction of alumina with liquid Pb83Li17 alloy. *Fusion Engineering and Design*, **89**(11), 2554-2558.

39. **Jalili**, **M. R. and A. R. Zarrati** (2004) Development and calibration of a resistivity probe for measurement of air concentration and bubble count in high-speed air-water flows. *Scientia Iranica*, **11**(4), 312-319.

40. **Jamnapara**, **N. I.**, **A. S. Sree**, **E. R. Kumar**, **S. Mukherjee and A. S. Khanna** (2014) Compatibility study of plasma grown alumina coating with Pb–17Li under static conditions. *Journal of Nuclear Material*, **455**(1-3), 612–617.

41. **Jun**, **F.**, **D. Min**, **J. Fanya**, **C. Meiyan**, **S. Liru**, **T. Honghui and Z. Guikai** (2016) Preparation and properties of alumina coatings as tritium permeation barrier by plasma electrolytic oxidation. *Rare Metal Materials and Engineering*, **45**(2), 315-320.

42. **Karcher**, **Ch.**, **Z. Lyu**, **Th. Boeck**, **N. Tran and U. Lüdtke** (2018) Experimental and numerical investigation on particle-induced liquid metal flow using Lorentz force velocimetry. *IOP Conf. Series: Materials Science and Engineering*, **424**, 012006.

43. **Keplinger**, **O.**, **N. Shevchenko and S. Eckert** (2017) Validation of X-ray radiography for characterization of gas bubbles in liquid metals. *IOP Conference Series: Material Science and Engineering*, **228**, 012009.

44. **Keplinger**, **O.**, **N. Shevchenko and S. Eckert** (2019) Experimental investigation of bubble breakup in bubble chains rising in a liquid metal. *International Journal of Multiphase Flow*, **116**, 39-50.

45. **Keplinger**, **O.**, **N. Shevchenko and S. Eckert** (2019) Experimental investigations of bubble chains in a liquid metal under the influence of horizontal magnetic field. *International Journal of Multiphase Flow*, **121**, 103111.

46. **Klaasen**, **B.**, **F. Verhaeghe**, **B. Blanpain and J. Fransaer** (2014) A study of gas bubbles in liquid mercury in a vertical Hele-Shaw cell. *Experiments in Fluids*, **55**, 1652.

47. **Kordač**, **M. and L. Košek** (2017) Helium bubble formation in Pb-16Li within the breeding blanket. *Fusion Engineering and Design*, **124**, 700-704.

48. **Krull**, **B.**, **E. Strumpf**, **O. Keplinger**, **N. Shevchenko**, **J. Fröhlich**, **S. Eckert and G. Gerbeth** (2017) Combined experimental and numerical analysis of a bubbly liquid metal flow. *IOP Conference. Series: Materials Science and Engineering*, **228**, 012006.

49. **Kumar**, **M.**, **A. Patel**, **A. Jaiswal**, **A. Ranjan**, **D. Mohanta**, **S. Sahu**, **A. Saraswat**, **P. Rao**, **T. S. Rao**, **V. Mehta**, **S. Ranjith Kumar**, **R. Bhattacharyay**, **E. Rajendrakumar**, **S. Malhotra and P. Satyamurthy** (2019) Engineering design and development of lead lithium loop for thermo-fluid MHD studies. *Fusion Engineering and Design*, **138**, 1-5.

50. **Levchuk**, **D.**, **F. Koch**, **H. Maier and H. Bolt** (2004) Deuterium permeation through Eurofer and α-alumina coated Eurofer. *Journal of Nuclear Materials*, **328**(2-3), 103–106.

51. **Lobanov**, **P. D. and M. A. Pakhomov** (2017) Experimental and numerical study of heat transfer enhancement in a turbulent bubbly flow in a sudden pipe expansion. *Journal of Engineering Thermophysics*, **26**, 377–390.

52. **Lu**, **W.**, **W. Wang**, **H. Jiang**, **G. Zuo**, **B. Pan**, **W. Xu**, **D. Chu**, **J. Hu and J. Qi** (2017) Investigation of wetting property between liquid lead lithium alloy and several structural materials for Chinese DEMO reactor. *Journal of Nuclear Materials*, **494**, 303-310.

53. **Lyu**, **Z.** (2019) Lorentz force velocimetry in liquid metal two-phase flow applications. *PhD Thesis*, Technische Universität Ilmenau.

54. **Malang**, **S.**, **A. R. Raffray and N. B. Morley** (2009) An example pathway to a fusion power plant system based on lead–lithium breeder: Comparison of the dual-coolant lead–lithium (DCLL) blanket with the helium-cooled lead–lithium (HCLL) concept as initial step. *Fusion Engineering and Design*, **84**(12), 2145-2157.

55. **Malang**, **S.**, **H. U. Borgstedt**, **E. H. Farnum**, **K. Natesan and I. V. Vitkovski** (1995) Development of insulating coatings for liquid metal blankets. *Fusion Engineering and Design*, **27**, 570-586.

56. **Martelli**, **D.**, **A. Venturini and M. Utili** (2019) Literature review of lead-lithium thermophysical properties. *Fusion Engineering and Design*, **138**, 183-195.

57. **Martsiniouk**, **D. Ye. and A. P. Sorokin** (2000) The questions of liquid metal two-phase flow modelling in the FBR core channels. *State Scientific Centre of Russian Federation*, Institute of Physics and Power Engineering, Obinisk, Kaluga Region, Russian Federation.

58. **Matsuura**, **H. and M. Nishikawa** *Evaluation method of tritium breeding ratio using neutron transport equation*. pp. 257-272. *In* ***Tanabe T.*** *(eds.) Tritium: Fuel of Fusion Reactors.* Springer, Japan, 2017.

59. **Megger guide** (2006) A stitch in time: The complete guide to electrical insulation testing.

60. **Mitsuyama**, **T.**, **T. Terai**, **T. Yoneoka and S. Tanaka** (1998) Compatibility of insulating ceramic materials with liquid breeders. *Fusion Engineering and Design*, **39–40**, 811–817.

61. **Muñoz-Cobo**, **J. L.**, **S. Chiva**, **S. Méndez**, **G. Monrós**, **A. Escrivá and J. L. Cuadros** (2017) Development of Conductivity Sensors for Multi-Phase Flow Local Measurements at the Polytechnic University of Valencia (UPV) and University Jaume I of Castellon (UJI). *Sensors*, **17**(5), 1077.

62. **Nuclear Energy Agency Handbook** (2015) Handbook on lead-bismuth eutectic alloy and lead properties, materials compatibility, thermal hydraulics and technologies. *OECD 2015*: NEA. No. 7268.

63. **Patel, P.**, **N. I. Jamnapara**, **A. Zala and S. D. Kahar** (2020) Investigation of hot-dip aluminized Ti6Al4V alloy processed by different thermal treatments in an oxidizing atmosphere. *Surface and Coatings Technology*, **385**, 125323.

64. **Paul**, **B.**, **K. Raju**, **M. Vadsola**, **T. S. R. C. Murthy**, **J. Kishor**, **P. Arora**, **P. Chakraborty**, **K. Singh**, **S. Majumdar and V. Kain** (2018) Investigations on wear and liquid metal corrosion behavior of aluminized IN-RAFMS. *Fusion Engineering and Design*, **128**, 204–214.

65. **Pint**, **B. A. and K. L. More** (2008) Transformation of Al_2O_3 to $LiAlO_2$ in Pb–17Li at 800°C. *Journal of Nuclear Materials*, **376**(1), 108–113.

66. **Purushothaman**, **J.**, **R. Ramaseshan**, **S. K. Albert**, **R. Rajendran**, **N. Gowrishankar**, **V. Ramasubbu**, **S. Murugesan**, **A. Dasgupta and T. Jayakumar** (2015) Influence of surface roughness and melt superheat on HDA process to form a tritium permeation barrier on RAFM steel. *Fusion Engineering and Design*, **101**, 154-164.

67. **Rajendrakumar**, **E.**, **T. Jayakumar and A. K. Suri** (2012) Overview of TBM R&D activities in India. *Fusion Engineering and Design,* **87**, 461-465.

68. **Rapisarda**, **D.**, **I. Fernandez**, **I. Palermo**, **F. R. Urgorri**, **L. Maqueda**, **D. Alonso**, **T. Melichar**, **O. Frýbort**, **L. Vála**, **M. Gonzalez**, **P. Norajitra**, **H.**

Neuberger and A. Ibarra (2017) Status of the engineering activities carried out on the European DCLL. *Fusion Engineering and Design,* **124**, 876–881.

69. **Ratajczak**, **M.**, **D. Hernández**, **T. Richter**, **D. Otte**, **D. Buchenau**, **N. Krauter and T. Wondrak** (2017) Measurement techniques for liquid metals. *IOP Conference. Series: Materials Science and Engineering*, **228**, 012023.

70. **Rowcliffe**, **A. F.**, **L. M. Garrison**, **Y. Yamamoto**, **L. Tan and Y. Katoh** (2018) Materials challenges for the fusion nuclear science facility. *Fusion Engineering and Design*, **135**, 290–301.

71. **Saito**, **Y. and K. Mishima** (2012) Bubble measurements in liquid-metal two-phase flow by using a four-sensor probe. *Multiphase Science and Technology*, **24**(4), 279-297.

72. **Saito**, **Y.**, **K. Mishima and M. Matsubayashi** (2004) Void fraction and velocity measurement of simulated bubble in a rotating disc using high frame rate neutron radiography. *Applied Radiation and Isotopes*, **61**(4), 667-674.

73. **Saito**, **Y.**, **K. Mishima**, **Y. Tobita**, **T. Suzuki and M. Matsubayashi** (2004) Velocity field measurement in gas-liquid metal two-phase flow with use of PIV and neutron radiography techniques. *Applied Radiation and Isotopes*, **61**(4), 683-691.

74. **Saito**, **Y.**, **K. Mishima**, **Y. Tobita**, **T. Suzuki and M. Matsubayashi** (2005) Measurements of liquid–metal two-phase flow by using neutron radiography and electrical conductivity probe. *Experimental Thermal and Fluid Science*, **29**(3), 323-330.

75. **Sano**, **M. and K. Mori** (1974) Bubble Formation from Single Nozzles in Liquid Metals. *Journal of the Iron and Steel Institute of Japan*, **60**, 348.

76. **Sano**, **M. and K. Mori** (1980) Size of Bubbles in Energetic Gas Injection into Liquid Metal. *Transactions of the Iron and Steel Institute of Japan*, **20**(10), 675-681.

77. **Santos**, **P. S.**, **H. S. Santos and S. P. Toledo** (2000) Standard transition aluminas. Electron microscopy studies. *Materials Research*, **3**, 104-114.

78. **Saraswat**, **A.**, **A. Prajapati**, **R. Bhattacharyay**, **P. Chaudhuri and S. Gedupudi** *Experimental investigations on bubble detection in water-air two-phase vertical columns*. pp. 555-566. *In:* **Kumar A., Pal A., Kachhwaha S.S., Jain P.K.** *(eds.) Recent Advances in Mechanical Engineering. Lecture Notes in Mechanical Engineering*. Springer, Singapore, 2021.

79. **Saraswat**, **A.**, **S. Sahu**, **T. S. Rao**, **A. Prajapati**, **S. Verma**, **S. Gupta**, **M. Kumar**, **R. P. Bhattacharyay and P. Das** (2016) Development of sensors for

high-temperature high-pressure liquid Pb/Pb-16Li applications. *Proceeding of IAEA Fusion Energy Conference-2016*.

80. **Schulz**, **B.** (1991) Thermophysical properties of the Li(17)Pb(83) alloy. *Fusion Engineering and Design*, **14**(3-4), 199-205.

81. **Schwerdtfeger**, **K.** (1968) Velocity of rise of argon bubbles in mercury. *Chemical Engineering Science*, **23**, 937-938.

82. **Sedano**, **L. A.** (2007) Helium bubble cavitation phenomena in Pb-15.7Li and potential impact on tritium transport behaviour in HCLL breeding channels. *Ciemat Technical Reports EURATOM / CIEMAT Fusion Association – 103*, National Magnetic Confinement Fusion Laboratory.

83. **Shikama**, **T.**, **R. Knitter**, **J. Konys**, **T. Muroga**, **K. Tsuchiya**, **A. Moesslang**, **H. Kawamura and S. Nagata** (2008) Status of development of functional materials with perspective on beyond-ITER. *Fusion Engineering and Design*, **83**, 976–982.

84. **Siegel**, **D. J.**, **L. G. Hector**, **Jr. and J. B. Adams** (2002) Adhesion, atomic structure, and bonding at the Al(111)/$\alpha-Al_2O_3$(0001) interface: A first principles study. *Physical Review B*, **65**, 085415.

85. **Singh**, **K.**, **A. Fernandes**, **B. Paul**, **M. R. Gonal**, **G. Abraham and N. Krishnamurthy** (2014) Preparation and investigation of aluminized coating and subsequent heat treatment on 9Cr–1Mo Grade 91 steel. *Fusion Engineering and Design*, **89**(11), 2534-2544.

86. **Smolentsev**, **S.**, **N. B. Morley**, **M. Abdou and S. Malang** (2015) Dual-coolant lead–lithium (DCLL) blanket status and R&D needs. *Fusion Engineering and Design*, **100**, 44–54.

87. **Sree**, **A. S. and E. Rajendrakumar** (2014) Effect of heat treatment and silicon concentration on microstructure and formation of intermetallic phases on hot dip aluminized coating on Indian RAFMS. *Fusion Science and Technology*, **65**(2), 282-291.

88. **Stefani**, **F.**, **S. Eckert**, **G. Gerbeth**, **A. Giesecke**, **T. Gundrum**, **D. Räbiger**, **M. Seilmayer and T. Weier** (2017) The DRESDYN project: planned experiments and present status. *Proceedings in Applied Mathematics and Mechanics* **17**, 123 – 126.

89. **Stefański**, **S.**, **W. Kalawa**, **K. Mirek and M. Stępień** (2017) Visualization and research of gas-liquid two phase flow structures in cylindrical channel. *E3S Web of Conferences*, **14**, 01026.

90. **Suzuki**, **T.**, **Y. Tobita**, **S. Kondo**, **Y. Saito and K. Mishima** (2003) Analysis of gas–liquid metal two-phase flows using a reactor safety analysis code SIMMER-III. *Nuclear Engineering and Design*, **220**, 207–223.

91. **Tanaka**, **S.**, **Y. Ohara and H. Kawamura** (2000) Blanket R&D activities in Japan towards fusion power reactors. *Fusion Engineering and Design,* **51–52**, 299–307.

92. **Tang**, **T.**, **Z. Zhang**, **J. B. Meng and D. L. Luo** (2009) Synthesis and characterization of lithium silicate powders. *Fusion Engineering and Design*, **84**(12), 2124–2130.

93. **Thiyagarajan**, **T. K.**, **P. Satyamurthy**, **N. S. Dixit**, **N. Venkatramani**, **A. Garg and N. R. Kanvinde** (1995) Void fraction profile measurements in two-phase mercury — nitrogen flows using gamma-ray attenuation method. *Experimental Thermal and Fluid Science*, **10**, 347-354.

94. **Timmel**, **K.**, **N. Shevchenko**, **M. Roder**, **M. Anderhuber**, **P. Gardin**, **S. Eckert and G. Gerbeth** (2015) Visualization of Liquid Metal Two-phase Flows in a Physical Model of the Continuous Casting Process of Steel. *Metallurgical and Materials Transactions B*, **46**, 700–710.

95. **Tosti**, **S.**, **A. Moriani and A. Santucci** (2013) Design and manufacture of an oven for high temperature experiments of erosion–corrosion of SiC_f/SiC into LiPb. *Fusion Engineering and Design*, **88**(9-10), 2479-2483.

96. **Tsuchiya**, **K.**, **M. Aida**, **Y. Fujii and M. Okamoto** (1993) Bubble formation from a single nozzle in moderator liquids and liquid metal for tritium breeding. *Journal of Nuclear Materials*, **207**, 123-129.

97. **Usov**, **E. V.**, **P. D. Lobanov**, **N. A. Pribaturin**, **V. I. Chuhno**, **A. E. Kutlimetov and A. I. Svetonosov** (2017) Numerical simulation of gas volume motion during the gas injection into liquid metal coolant. *IOP Conf. Series: Journal of Physics: Conf. Series*, **899**, 032024.

98. **Utili**, **M.**, **S. Bassini**, **L. Boccaccini**, **L. Bühler**, **F. Cismondi**, **A. Del Nevo**, **M. Eboli**, **F. DiFonzo**, **T. Hernandez**, **S. Wulf**, **M. Kordač**, **D. Martelli**, **E. Mas De les Valls**, **T. Melichar**, **C. Mistrangelo**, **M. Tarantino**, **A. Tincani and L. Vála** (2019) Status of Pb-16Li technologies for European DEMO fusion reactor. *Fusion Engineering and Design*, **146**, 2676–2681.

99. **Valls**, **E. M.**, **A. Cegielski**, **M. Jaros**, **M. Pérez-Ferragut**, **L. Batet**, **T. Sandeep**, **V. Chaudhari and J. Freixa** (2020) Development of flow regime maps for lead lithium eutectic–helium flows. *Fusion Engineering and Design*, **158**, 111691.

100. **Vassallo**, **E.**, **M. Pedroni and V. Spampinato** (2018) Effect of alumina coatings on corrosion protection of steels in molten lead. *Journal of Vacuum Science &* Technology B, **36**, 01A105.

101. **Vogt**, **T.**, **S. Boden**, **A. Andruszkiewicz**, **K. Eckert**, **S. Eckert and G. Gerbeth** (2015) Detection of gas entrainment into liquid metals. *Nuclear Engineering and Design*, **294**, 16-23.

102. **Walker**, **A.** (2010) An investigation of gas bubble generation and measurement in water and mercury. *Master's Thesis,* University of Tennessee, Knoxville.

103. **Wang**, **L.**, **J. Yang**, **C. Liang**, **Y. Feng**, **W. Jin**, **J. Cao**, **X. Wang**, **K. Feng**, **A. W. Kleyn and N. Liu** (2019) Preparation and properties of improved Al_2O_3 based MOD coatings as tritium permeation barrier. *Fusion Engineering and Design*, **143**, 233-239.

104. **Wang**, **Z. H.**, **S. D. Wang**, **X. Meng and M. J. Ni** (2017) UDV measurements of single bubble rising in a liquid metal Galinstan with a transverse magnetic field. *International Journal of Multiphase Flow*, **94**, 201-208.

105. **Wulf**, **S. E.**, **N. Holstein**, **W. Krauss and J. Konys** (2013) Influence of deposition conditions on the microstructure of Al-based coatings for applications as corrosion and anti-permeation barrier. *Fusion Engineering and Design*, **88**(9-10), 2530– 2534.

106. **Wulf**, **S. E.**, **W. Krauss and J. Konys** (2018) Long-term corrosion behavior of Al-based coatings in flowing Pb–15.7Li, produced by electrochemical ECX process. *Nuclear Materials and Energy*, **16**, 158-162.

107. **Xu**, **W.**, **K. J. Xu**, **J. P. Wu**, **X. L. Yu and X. X Yan** (2019) Peak-to-peak standard deviation based bubble detection method in sodium flow with electromagnetic vortex flowmeter. *Review of Scientific Instruments*, **90**, 065105.

108. **Zala**, **A. B.**, **N. I. Jamnapara**, **C. S. Sasmal**, **P. Chaudhuri and M. Ranjan** (2019) Investigation of alumina film formed over aluminized RAFM steel by plasma assisted heat treatment. *Fusion Engineering and Design*, **146**(B), 2002-2006.

109. **Zhang, C., S. Eckert and G. Gerbeth** (2005) Experimental study of single bubble motion in a liquid metal column exposed to a DC magnetic field. *International Journal of Multiphase Flow*, **31**, 824–842

110. **Zhang**, **G. K.**, **C.A. Chen**, **D.L. Luo and X. L. Wang** (2012) An advance process of aluminum rich coating as tritium permeation barrier on 321 steel workpiece. *Fusion Engineering and Design*, **87**(7-8), 1370– 1375.

111. **Zhang**, **K. and Y. Hatano** (2010) Preparation of Mg and Al phosphate coatings on ferritic steel by wet-chemical method as tritium permeation barrier. *Fusion Engineering and Design*, **85**(7-9), 1090–1093.

112. **Zheng**, **S. and M. Zhu** (2018) New process with argon injected into ladle around the tapping hole for controlling slag carry-over during continuous casting ladle. *Metals*, **8**(8), 624.

113. **Zhu**, **C.**, **W. Zhang**, **L. Wang**, **Z. Ning**, **Y. Feng**, **K. Feng**, **J. Liao**, **Y. Yang**, **N. Liu and J. Yang** (2020) Effect of thermal cycles on structure and deuterium permeation of Al_2O_3 coating prepared by MOD method. *Fusion Engineering and Design*, **159**, 111750.

CURRICULUM VITAE

1.	**NAME**	:	Abhishek Saraswat
2.	**DATE OF BIRTH**	:	04 September 1987

3. **EDUCATIONAL QUALIFICATIONS**

2010 Bachelor of Engineering (B.E.)

Institution	:	University of Delhi, Delhi
Specialization	:	Instrumentation & Control Engineering

Master of Science (M.S.)

Institution	:	Indian Institute of Technology Madras
Registration Date	:	22-07-2019

4. **PROFESSIONAL EXPERIENCE**

2011-Present	:	Scientific Officer Institute for Plasma Research, Gandhinagar

GENERAL TEST COMMITTEE

CHAIRPERSON:	Prof. A. Seshadri Sekhar Head of the Department Department of Mechanical Engineering, IIT Madras
GUIDE(S):	Dr. Sateesh Gedupudi Assistant Professor Department of Mechanical Engineering, IIT Madras
	Dr. Paritosh Chaudhuri Head of the Division Fusion Blanket Division, IPR Gandhinagar
MEMBERS:	Dr. Mayank Mittal Associate Professor Department of Mechanical Engineering, IIT Madras
	Dr. Srinivasa Rao Bakshi Associate Professor Department of Metallurgical and Materials Engineering, IIT Madras